Swansea University
Prifysgol Abertawe

The study and evaluation of ohmic contacts on GaN based wide band gap semiconductors

Gareth Davies, BSc (Hons)

Swansea University

Submitted to Swansea University in fulfilment of the requirements for the Degree of MSc by Research

Supervised by

Professor Michael Jennings Swansea University

January 2025

Declarations

This work has not previously been accepted in substance for any degree and is not being concurrently submitted in candidature for any degree.

Signed: 

Date: 08/01/2025

This thesis is the result of my own investigations, except where otherwise stated. Other sources are acknowledged by footnotes giving explicit references. A bibliography is appended.

Signed: 

Date: 08/01/2025

I hereby give consent for my thesis, if accepted, to be available for electronic sharing

Signed: 

Date: 08/01/2025

The University's ethical procedures have been followed and, where appropriate, that ethical approval has been granted.

Signed: 

Date: 08/01/2025

Declaration

I declare that this thesis has been composed solely by myself and that it has not been submitted, in whole or in part, in any previous application for a degree. Except where states otherwise by reference or acknowledgment, the work presented is entirely my own. The work presented in chapters 6 and 7 have been published by the author.

Gareth Davies

January 2025

Executive Summary

Wide band gap (WBG) semiconductors, particularly Gallium Nitride (GaN), have emerged as transformative materials in power electronics, surpassing the limitations of traditional silicon-based devices. This thesis presents a detailed investigation into the development and optimization of ohmic contacts for GaN-based High Electron Mobility Transistors (HEMTs), aiming to enhance performance, reliability, and efficiency.

Key Objectives and Methodology:

The study focuses on evaluating ohmic contacts using materials such as pure aluminium (Al), aluminium Silicon Copper (AlSiCu), Titanium (Ti), and Tantalum (Ta). Fabrication processes, including deposition and annealing at temperatures up to 600°C, were conducted to establish robust metal-semiconductor interfaces. Electrical characteristics were measured across varying temperatures (300K–400K), employing the Transmission Line Method (TLM) to extract specific contact resistivity (ρC) and analyse transport mechanisms like Thermionic Emission (TE), Thermionic Field Emission (TFE), and Field Emission (FE).

Major Findings:

1. **Material Performance**:
    - Specific contact resistivity values were significantly influenced by material and doping configurations. For example, the 250Å Ti / 3000Å Pure Al contact on GaN exhibited a low ρC of 3.14×10^{-3} Ω·cm² at 400K, validating its suitability for high-performance HEMTs.
    - The AlN substrate demonstrated lower resistivity compared to nucleation layers, highlighting the impact of substrate quality.
2. **Temperature-Dependent Behaviour**:
    - At elevated temperatures, ohmic contacts showed a reduction in resistivity by an order of magnitude, aligning with TFE theory. This supports enhanced electron tunnelling across the metal-semiconductor interface under thermal excitation.

3. **Structural Integrity**:
    - Post-annealing analysis using Scanning Electron Microscopy (SEM) and Transmission Electron Microscopy (TEM) confirmed defect-free interfaces, crucial for device reliability.
    - Energy Dispersive X-ray (EDX) analyses further ensured the absence of contamination at the metal-GaN junctions.

Practical Implications:

The results underscore the potential of Au-free ohmic contacts in reducing RDS(on), a critical parameter for power efficiency in GaN HEMTs. Optimizing these contacts can enable devices that consume less power while maintaining high-speed and thermal performance, paving the way for applications in renewable energy, electric vehicles, and high-frequency communication systems.

Recommendations for Future Work:

1. Explore additional material combinations and device geometries to identify configurations with optimal performance for specific applications.
2. Conduct detailed gate-voltage dependency studies to further understand the interplay between contact resistance and device operation.
3. Leverage advanced characterization techniques to refine structural and electrical insights, potentially guiding next-generation device fabrication.

This research provides a foundational understanding of ohmic contact behaviours in GaN-based HEMTs and contributes valuable insights toward advancing semiconductor technology for energy-efficient solutions in power electronics.

Acknowledgements

For the proposal of the Thesis and his expertise in wide band gap semiconductors I am deeply indebted to Professor Michael Jennings from Swansea University, for his guidance, perseverance, and advice.

Many thanks also need to go to Dr Andrew Withey for all his support and guidance during this Thesis, without his support none of this would be possible.

I would like to also acknowledge the training department, especially Joanne Daniels for her dedication in providing the opportunity for me to undertake a MSc.

Lastly, I would like to mention the Failure Analysis Department for going beyond in their duties to free up valuable time for me to perform my research and characterisation over the previous two years.

Contents

List of Figures

List of Tables

List of Abbreviations

2DEG	*Two-Dimensional Gas*
Al	*Aluminium*
AlN	*Aluminium Nitride*
AlSiCu	*Aluminium Silicon Copper*
AU	*Gold*
CTLM	*Circular Transmission Line Method*
EBSD	*Electron Backscatter Diffraction*
EDS	*Energy Dispersive Spectroscopy*
EDX	*Energy Dispersive X-Ray*
FE	*Field Emission*
FET	*Field Effect Transistor*
FIB	*Focused Ion Beam*
GaN	*Gallium Nitride*
GDS	*Graphical Data Stream*
HCP	*Hexagonal Close Packed*
HEMT	*High Electron Mobility Transistor*
HVPE	*Hydride Vapor Phase Epitaxy*
IC	*Integrated Circuit*
IGBT	*Integrated-Gate Bipolar Transistor*
LPVCD	*Low Pressure Chemical Vapor Deposition*
MBE	*Molecular Beam Epitaxy*
MOCVD	*Metal Organic Chemical Vapor Deposition*
MOSFET	*Metal Oxide Semiconductor Field Effect Transistor*
PCM	*Process Control Monitoring*
SDD	*Silicon Drift Detector*
SEM	*Scanning Electron Microscopy*
Si	*Silicon*
SiC	*Silicon Carbide*
Ta	*Tantalum*
TE	*Thermionic Emission*
TEM	*Transmission Electron Microscopy*
TFE	*Thermionic Field Emission*
Ti	*Titanium*
TLM	*Transmission Line Method*
UHR	*Ultra-High Resolution*
WBG	*Wide Band Gap*
XRD	*X-Ray Diffraction*

Chapter 1: Introduction

In semiconductors, the bandgap is the energy difference between the top of the valence band and the bottom of the conduction band. This energy gap stands for the smallest amount of energy needed to excite an electron from the valence band (filled with electrons) to the conduction band (empty or partially filled with electrons), resulting in the creation of a mobile electron (or hole) that can conduct electricity. The size of the bandgap can affect a semiconductor's electrical properties and its suitability for different applications. The bandgap energy of GaN is a "large" bandgap, as it is larger than most semiconductors such as silicon, which allows GaN to be used in high-power and high-temperature electronic applications such as power electronics [1].

Additionally, Aluminium Nitride (AlN) is also a wide bandgap semiconductor, and it has similar electronic and optical properties to GaN. Therefore, they can be used together in some electronic devices, such as high-power and high-frequency transistors, high-power microwave devices, and high-temperature sensors. One example of their use together is in the field of high-electron-mobility transistors (HEMTs), which are used in high-frequency and high-power electronic applications. In these devices, GaN is used as the active layer, while AlN is also electrically insulating providing safety at higher voltages. This is because AlN has a higher thermal conductivity than GaN and can better dissipate heat generated by the device, which allows for higher power density and improves device performance [2]. In GaN HEMTs, AlN is favoured for its exceptional thermal conductivity and lattice match with GaN, while AlGaN, with its tuneable bandgap and robust piezoelectric effects, is extensively used for channel modulation. Metal contact resistivity is also extremely important in semiconductors especially in wide band gap power devices as this contact resistance at the gate and the source effects the overall on resistance $(R_{DS(on)})$ of the device.

Contact resistance is a measure of the resistance between the metal contact points of a device. $R_{DS(on)}$, or "on-state resistance," is a measure of the resistance between the source and drain of a MOSFET (metal-oxide-semiconductor field-effect transistor) when the transistor is in the "on" state, allowing current to flow. The contact resistance adds to the unipolar limit figure of merit, shown in Fig.1.1, debilitating its on-state performance even further. The crystalline wurtzite structure of GaN is extremely strong, GaN is also mechanically robust, with high hardness and resistance to

deformation, making it ideal for high-power applications. GaN can also handle sufficiently elevated temperatures without breaking down, the wurtzite crystal lattice also supplies the ability to achieve extremely high conductivity as compared to Silicon and Silicon Carbide [3]

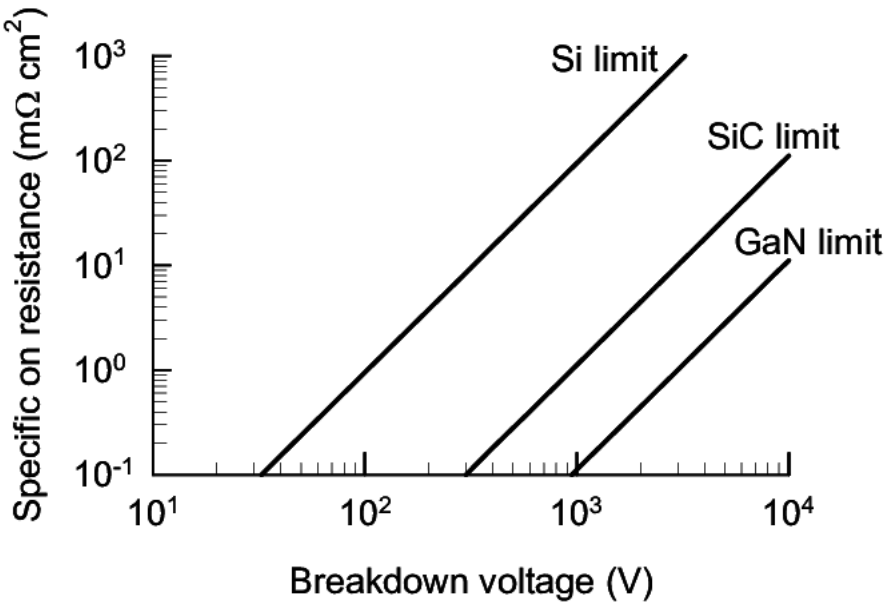

Fig. 1.1: On resistance versus breakdown voltage [4]

The quality of the ohmic contacts plays a pivotal role in determining the overall device performance. Ohmic contacts are essential for enabling efficient carrier injection and extraction at the source and drain terminals of the transistor, facilitating the transport of electrons through the channel region. Achieving low contact resistivity is of paramount importance in minimizing power losses and maximizing device efficiency. The intricate interplay between the material properties of the contacts, the semiconductor, and the fabrication processes significantly influences the contact resistance, which in turn affects the current transport mechanisms within the device.

Consequently, an in-depth evaluation of ohmic contacts on GaN based HEMTs becomes indispensable for optimising device characteristics, as the efficiency of carrier flow directly impacts the device's operational capabilities. Despite significant advancements, existing research still faces several shortcomings, including limited understanding of contact behaviour under high-temperature and high-frequency conditions, inconsistencies in reported contact resistivity values due to variations in fabrication techniques, and a lack of standardised methodologies for evaluating

reliability and long-term stability of ohmic contacts. This thesis delves into the rigorous assessment of ohmic contacts on GaN-based HEMTs, shedding light on the key factors affecting contact resistivity, their implications for current transport, and their overall significance for device functionality.

This thesis is structured to provide a comprehensive investigation into the design, fabrication, and characterisation of ohmic contacts on GaN based wide bandgap semiconductors. Chapter 2 provides a detailed review of the properties of wide bandgap semiconductors, with a particular focus on the material properties of GaN, including its structural, electrical, and thermal characteristics, which make it suitable for high power and high frequency applications. Chapter 3 explores the fundamental principles of metal semiconductor contact mechanisms, including Schottky and ohmic contact formation, and examines the current transport models, such as thermionic emission (TE) and thermionic field emission (TFE), that govern these interfaces.

Chapter 4 outlines the experimental methodologies employed in this study, detailing the fabrication processes, deposition techniques, and annealing procedures used to produce the ohmic contacts, as well as the advanced characterisation techniques such as SEM, TEM, and EDX utilised to evaluate structural and compositional integrity. Chapters 5 and 6 focus on material fabrication and device characterisation, respectively. Chapter 5 presents the specifics of the GaN substrates and epitaxial layers, including nucleation and AlN buffer layers, while Chapter 6 provides an in-depth discussion on the metallisation stacks and process parameters adopted to form the ohmic contacts. The electrical measurements and characterisation results are analysed in Chapter 7, where the specific contact resistivity values, doping densities, and barrier heights are presented and compared with theoretical models and state-of-the-art benchmarks. This chapter also evaluates the temperature dependence of contact performance and its correlation with thermionic field emission mechanisms.

Finally, Chapter 8 concludes the thesis with a summary of the key findings, emphasising the structural robustness and electrical performance of the fabricated contacts. It also outlines practical implications for GaN-based device applications and provides recommendations for future research, including the exploration of additional material systems, geometries, and high-temperature performance evaluations.

Chapter 2: Properties of wide band gap semiconductors

This chapter illustrates the main properties of wide band gap semiconductors, and in particular, Gallium Nitride. After a brief illustration of the crystalline structure the electrical properties will then be discussed showing the advantages of GaN devices over the more traditional Silicon devices.

2.1 Crystalline structures

A semiconductor is a material that has electrical conductivity between that of a conductor and an insulator. In a crystalline structure, the atoms are arranged in a repeating pattern that forms a three-dimensional lattice. The atoms in a semiconductor crystal are held together by chemical bonds, which allows electrons to move freely through the material. This movement of electrons is what gives semiconductors their electrical conductivity.

2.1.1 GaN crystalline structure

Gallium Nitride (GaN) has a hexagonal crystal structure known as the wurtzite structure (Fig. 2.1). In this structure, the atoms are arranged in a repeating pattern of hexagonal unit cells. These hexagons can be found within the basal plane of the crystal lattice, where the nitrogen atoms occupy the corners of the hexagons, and the gallium atoms are positioned at the center of each hexagon. These properties make GaN a desirable material for high-power and high-frequency electronic devices and power electronics

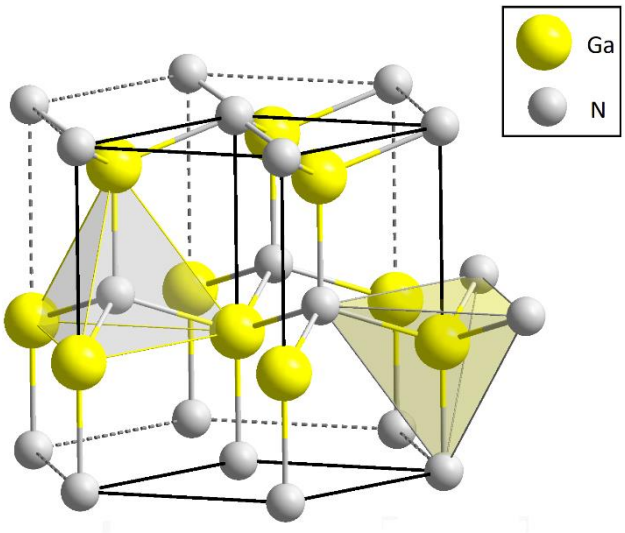

Fig. 2.1: Schematic of wurtzite GaN lattice [5]

2.1.2 AlN crystalline structure

Aluminium Nitride can have a wurtzite structure, but it can also have a hexagonal close-packed (HCP) crystal structure. AlN can be used as a substrate in the growth of GaN, this process is called an AlN buffer layer, which helps to improve the quality of the GaN crystal.

2.1.3 Spontaneous polarisation

Spontaneous polarization in metal contacts to GaN substrates arises from the inherent charge separation within GaN's wurtzite crystal structure [6]. This polarization creates a permanent electric dipole moment across the layers, inducing an electric field from the Ga-rich to the N-rich surface [7]. When metal contacts are established, the interaction with this field influences the metal-semiconductor interface, impacting Fermi level pinning, Schottky barrier height, carrier transport, contact resistance, and device performance. Understanding and managing these effects are crucial for optimizing GaN-based electronic and optoelectronic device performance [8].

2.2 Electrical properties

There are five important electrical properties of semiconductor devices, Band gap (E_g), Critical field (E_{Crit}), Electron Mobility (μ_n), Permittivity (ε_r) and Thermal Conductivity (λ). Table 2.1 below shows the material properties of Silicon, GaN and SiC [5]

Table 2.1: Material properties of Silicon, GaN and SiC

Parameter		**Silicon**	**GaN**	**SiC**
Band gap (E_g)	*eV*	1.12	3.39	3.26
Critical field (E_{Crit})	*MV/cm*	0.23	3.3	2.2
Electron Mobility (μ_n)	$cm^2/V.s$	1400	1500	950
Permittivity (ε_r)		11.8	9	9.7
Thermal Conductivity (λ)	*W/cm.K*	1.5	1.3	3.8
Intrinsic carrier concentrations (n_i)	cm^{-3}	$1.5x10^{10}$	$1.9x10^{-10}$	$8.2x10^{-9}$

The first four properties from the above table will be looked at in a bit more depth.

2.2.1 Band gap (E_g)

A semiconductor band gap is proportional to the strength of the chemical bonds within the lattice of the material and because of the strong bonds in a GaN lattice the

electrons find it difficult to jump between sites. These stronger chemical bonds also supply lower intrinsic leakage and the ability of the device to run at much higher temperatures [3]

2.2.2 Critical field (E_{Crit})

The stronger chemical bonds within a wide bandgap device also provide a higher critical electric field needed for impact ionisation, thus causing the device to breakdown (avalanche fail). The formula below illustrates the approximate voltage needed to break down the device:

$$V_{BR} = {}^{1}/_{2}\, W_{drift}.E_{crit} \qquad (1)$$

The equation shows that the breakdown voltage of the device is proportional to the width of the drift region (W_{drift}). For GaN and SiC the drift region can be ten times smaller than in a Silicon device for the same break down voltage. The smaller drift region in GaN and SiC devices results in lower resistance, faster switching, higher power density, and better thermal performance, making them ideal for next-generation power electronics. This technological edge enables smaller, lighter, and more efficient systems compared to silicon-based devices. Using Poisson's equation [3], we can figure out how many electrons are present between the two terminals.

$$q.N_D = \varepsilon_0.\varepsilon_r.E_{crit}/W_{drift} \qquad (2)$$

In Poisson's equation, q is the charge of electrons ($1.6\text{x}10^{-19}$ Coulombs), N_D is the number of electrons in the volume (cm^{-3}), ε_o is the permittivity of a vacuum measured in farads per meter ($8.854\text{x}10^{-12}$ F/m), and ε_r is the relative permittivity of crystal compared to a vacuum.

2.2.3 On resistance ($R_{DS(ON)}$)

The on resistance of a device refers to the resistance when the device is in the "on" state, meaning that it is conducting current. GaN devices have a low resistance when conducting current which means they are ideal for high power as compared to silicon. The on-resistance for a device can be explained with the theoretical specific on-state resistance equation.

$$R_{DS(on)} = W_{drift}/q.\mu_{n\cdot N_D}$$

(3)

The combining of equations 1, 2 and 3 shows the relationship between break down and specific on-state resistance.

$$R_{DS(on)} = 4.V_{BR}^2/\varepsilon_o.\varepsilon_r.E_{crit}^3$$

(4)

Fig. 1.1 shows this equation plotted for Si, SiC and GaN. The plot of this graph is for ideal devices and semiconductors are not always manufactured ideal. This plot only considers the resistivity of the drift region.

2.2.4 The two-dimensional electron gas (2DEG)

The wurtzite crystal structure of GaN (Fig. 2.1) leads to its capability to achieve high conductivity as compared to silicon. If the crystal structure is put under strain a shift in the atoms of the lattice will cause it to create an electric field. By producing a layer of AlGaN above the GaN a two-dimensional electron gas is created [5]. A two-dimensional electron gas (2DEG) is a thin layer of electrons that are only allowed to move in a two-dimensional plane. The 2DEG is created at the interface of the two different semiconductors, this interface is called a heterojunction, Fig. 2.2.

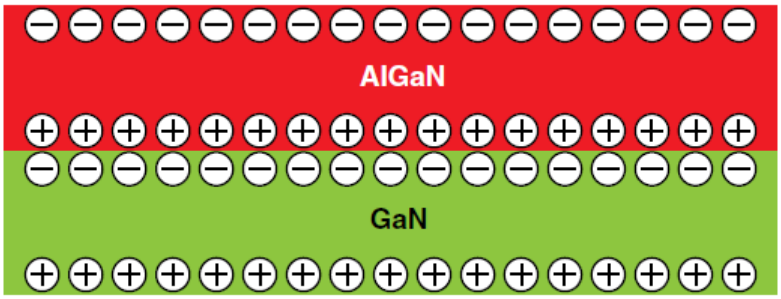

Fig. 2.2: GaN/AlGaN heterostructure showing the formation of a 2DEG [5]

2.2.5 On resistance ($R_{DS(on)}$) GaN HEMT through 2DEG

The on resistance of a transistor, in this case a GaN HEMT transistor is the sum of all resistances as the electrons flow through the device. Fig. 2.3 show the major elements that contribute to the total $R_{DS(on)}$ of the GaN HEMT.

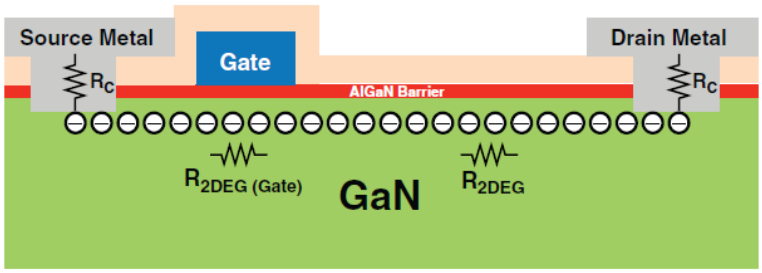

Fig. 2.3: Cross section of GaN HEMT showing major factors of $R_{DS(on)}$ [5]

The source and drain metal contacts connect to the 2DEG through the AlGaN barrier, this resistance is called the contact resistance (R_C). As the electrons then flow through the 2DEG they are then met with the 2DEG resistance (R_{2DEG}). The resistance of the R_{2DEG} is found by the mobility of electrons (μ_{2deg}) plus the number of electrons created by the 2DEG (N_{2DEG}). The total resistance is also contributed to by the distance the electrons must travel (L_{2DEG}), the width of the 2DEG (W_{2DEG}) plus the universal charge constant q (1.6 x 10^{-19} coulombs) [3].

$$R_{2DEG} = L_{2DEG}/(q.\mu_{2DEG}.N_{2DEG}.W_{2DEG}) \quad (5)$$

As discussed in section 2.2.4 The amount of strain induced by the AlGaN barrier will decide the number of electrons in the 2DEG. It is also found by the amount of voltage applied to the gate of the device. The following is a good approximation of the resistance of the GaN HEMT transistor as shown in Figure 2.3.

$$R_{HEMT} = 2\,.R_C + R_{2DEG} + R_{2DEG(Gate)} \quad (6)$$

Another contributing factor of R_{DSon} is parasitic metal loss plus each resistive part will also vary with temperature (*T*), we can approximate eq. 6 with these losses to find an overall R_{DSon}.

$$R_{DS(on)^{(t)}} = R_{parasitic^{(T)}} + (2.R_{C^{(T)}}) + (R_{2DEG} + R_{2DEG(Gate)^{(T)}}) \quad (7)$$

2.3 Advantages of GaN for power devices

The first report of GaN epitaxial dates to 1949 [9] but the breakthrough in AlGaN/GaN high mobility transistors (HEMTs) was not achieved until 1994 by A Kahn [10].

Recently the HEMT has become the go to device for high power applications, this is because as silicon is approaching its limits, the little increases in silicon performance are met with significant increases in costs. Today we demand high efficiency, fast switching, and less power to be consumed. AlGaN/GaN HEMTs can meet these requirements due to their outstanding properties of low channel resistance, high breakdown voltages and high switching frequency [11]. Generally, GaN devices can operate at higher voltages than Silicon (Si) devices, but lower than Silicon Carbide (SiC) devices. Typically, GaN devices can withstand voltages up to 600V, while silicon devices MOSFET are limited to around 200V, silicon MOSFET devices are typically limited to ~200V due to their narrower bandgap and lower breakdown voltage. This constraint restricts their use in medium and high-power applications. whilst SiC devices can handle several kilo-voltages. Also, we must consider that specific voltage capabilities can vary depending on the particular device design and application.

GaN and SiC both offer advantages over traditional based silicon devices especially in power semiconductors. However, there are key differences in their materials that can make GaN a more favourable choice in certain situations. While GaN offers several advantages, its thermal conductivity (~230 W/m·K) is lower than that of SiC (~490 W/m·K). However, GaN's higher electron mobility and lower switching losses make it highly efficient in high-frequency applications. These properties allow GaN-based devices to achieve higher power densities and more compact designs despite their lower thermal conductivity. On the other hand, SiC has its own distinct advantages. With a wider bandgap (~3.3 eV vs. 3.4 eV for GaN), higher thermal conductivity, and greater breakdown field strength, SiC is better suited for high-voltage and high-temperature applications, such as industrial motor drives and power grid converters."

Silicon carbide (SiC) is recognised for its resilience in harsh environments, including high-radiation settings such as space. Its wide bandgap and robust crystal structure contribute to its inherent radiation hardness, making it a suitable choice for space applications. However, it's important to note that while SiC devices exhibit certain radiation-resistant properties, they are not entirely immune to radiation-induced effects. Studies have shown that heavy-ion radiation can lead to degradation or catastrophic failure in SiC power devices. Therefore, careful consideration of device design and application-specific requirements is essential when deploying SiC-based

components in space environments [12]. Both GaN and SiC offer advantages over traditional silicon-based semiconductors, but the choice between the two will depend on the specific requirements of the application. In general, GaN may be a better choice for high-frequency, high-power applications where thermal management is important, while SiC may be a better choice for high-temperature and high-voltage applications where radiation resistance is important.

Also, with the recent advancement of GaN epitaxial capability it has allowed the manufacturing of GaN on Si wafers up to 200mm with high quality performance and low-cost manufacturing [13]. Because of GaN compatibility with Silicon fabrication plants the GaN on Si technology can be massed produced in silicon semiconductor fabrication plants. With advantages, such as reduced size and weight plus reduced costs it makes GaN power electronics a game changer for automotive applications [14].

GaN-based power electronics have emerged as a transformative technology in the automotive industry, particularly for applications requiring high efficiency, compact size, and robust thermal performance. GaN devices are widely utilised in electric vehicles (EVs) and hybrid electric vehicles (HEVs), where they enable more efficient on-board chargers, DC-DC converters, and inverters. The compact size of GaN components allows for lighter and smaller power modules, contributing to weight reduction and extending the driving range of electric vehicles. Additionally, GaN's superior thermal stability and high-voltage operation make it suitable for motor drives and powertrains in EVs, enhancing reliability under harsh operating conditions. These advantages position GaN power electronics as a critical enabler for the next generation of energy efficient, high performance automotive technologies.

Chapter 3: Metal semiconductor contacts

3.1 State of the art literature review

Gallium Nitride (GaN) High Electron Mobility Transistors (HEMTs) have emerged as a key technology for high-frequency, high-power, and high-temperature applications due to GaN's exceptional material properties. With a wide bandgap (~3.4 eV), high electron mobility (~2000 $cm^2/V \cdot s$), and large breakdown field (~3.3 MV/cm), GaN HEMTs outperform conventional silicon-based transistors, making them ideal for power electronics and RF applications [15]. A defining feature of GaN HEMTs is the formation of a Two-Dimensional Electron Gas (2DEG) at the interface between the GaN and AlGaN layers. This enables high electron mobility and low channel resistance, contributing to their superior performance in terms of speed, efficiency, and thermal management.

Achieving low resistance ohmic contacts is critical to optimising GaN HEMT performance, as high contact resistance can lead to power losses, heat generation, and reduced efficiency. However, the wide bandgap of GaN poses challenges in forming ohmic contacts due to the high Schottky barrier height at metal-GaN interfaces. Overcoming this issue requires innovative contact engineering strategies to achieve low specific contact resistivity (ρC) and maintain thermal stability during operation [16].

The most commonly employed ohmic contact scheme for GaN HEMTs is the Ti/Al-based stack, such as Ti/Al/Ni/Au and Ti/Al/Ti/Au. These contacts rely on titanium's ability to react with GaN during annealing to form TiN, which lowers the Schottky barrier and promotes electron tunnelling. Aluminium further reduces the work function, enhancing ohmic behaviour. Rapid thermal annealing (RTA) at 800–900°C has been shown to yield specific contact resistivities as low as $10^{-6}\ \Omega \cdot cm^2$, making Ti/Al-based contacts highly effective for RF and power applications [15]. Despite their widespread use, Ti/Al-based contacts may face challenges related to thermal stability at higher temperatures, prompting exploration of alternative materials.

Refractory metals such as Molybdenum (Mo) and Tantalum (Ta) have been investigated as potential candidates for thermally stable ohmic contacts. Studies have demonstrated that Mo/Au and Ta/Au contacts can achieve specific contact resistivities

of 10^{-5} Ω·cm² after annealing at 1000°C, making them suitable for harsh environments and high-temperature operations [16]. Such advancements highlight the importance of material engineering in improving the reliability of GaN devices for aerospace and automotive applications.

More recently, gold-free ohmic contacts have gained traction due to their cost-effectiveness and processing simplicity compared to gold-based alternatives. Combinations such as Ti/Al/Si and Ti/Al/Cu have demonstrated promising results, offering low resistivity, reduced material costs, and improved adhesion. These configurations address the growing demand for high-volume production and automotive applications where Au-free processing is preferred [17].

In addition to material innovations, advanced contact engineering techniques have shown remarkable improvements in performance. Regrown ohmic contacts employ Molecular Beam Epitaxy (MBE) to create highly doped GaN regions under the contact, achieving ultra-low specific contact resistivities of 10^{-7} Ω·cm². This technique provides excellent electrical properties and reliability, particularly for high-frequency devices [18]. Similarly, tunnel junction contacts, incorporating heavily doped n^+ GaN layers, utilize quantum tunnelling to reduce resistance and are particularly suited for vertical GaN power devices [19].

Looking forward, research continues to focus on improving ohmic contact performance by exploring low-barrier alloys and advanced surface passivation techniques to optimize contact uniformity and stability. Efforts are also underway to integrate GaN-on-Silicon (GaN-on-Si) technology into CMOS fabrication processes, enabling low-cost mass production for automotive and renewable energy systems [17]. The reliability of these contacts under prolonged thermal and electrical stress is being investigated to ensure suitability for high-power and high-frequency applications.

In conclusion, GaN HEMTs continue to evolve as a disruptive technology, driven by advancements in ohmic contact engineering. From traditional Ti/Al-based contacts to refractory metal and gold-free alternatives, modern developments have significantly enhanced thermal stability, cost efficiency, and scalability. The adoption of novel approaches like regrown layers and tunnel junctions' further cements GaN's role in the future of power electronics and RF devices. These advancements are critical for

enabling compact, efficient, and high-performance systems across industries such as telecommunications, automotive, and aerospace.

3.2 Schottky barrier

A Schottky barrier is an interface between two materials, notably a metal and a semiconductor. The metal and semiconductor have a difference in electron affinity, so a barrier is formed at the interface. For current to flow, electrons must pass through this energy barrier, this is performed by applying a voltage and thus reducing the barrier height $q\Phi_B$. Schottky contacts have a rectifying I-V characteristic due to the potential barrier that must be breached, whilst ohmic contacts have linear I-V curves, as shown in Fig. 3.1.

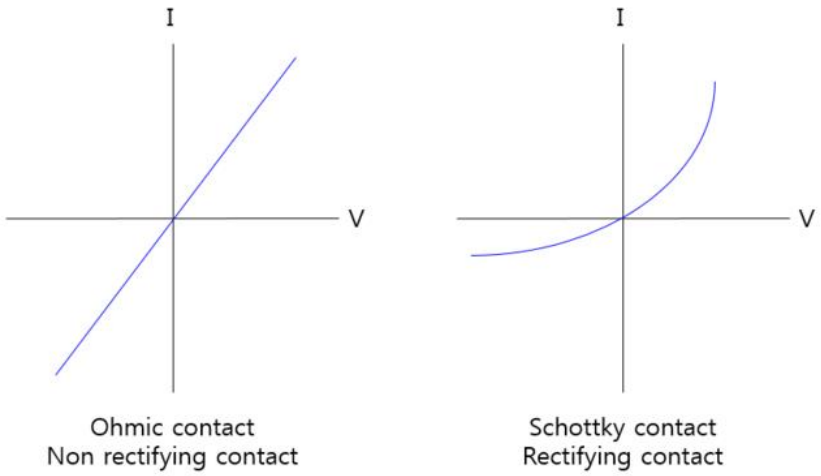

Fig. 3.1: I-V characteristics of ohmic and Schottky contact [1]

The height of the Schottky barrier depends on the properties of the metal and semiconductor, and can be modified by doping the semiconductor, changing the metal used, or by applying an external electric field.

When manufacturing AlGaN/GaN high electron mobility transistors (HEMTs) the desired outcome is for ohmic contacts with very low contact resistance. Metal is deposited onto an insulating AlGaN layer, beneath which a two-dimensional electron gas (2DEG) is induced. To establish current pathways through the AlGaN layer, there is a trade-off between its thickness and the resistance as shown in Fig. 3.2 below.

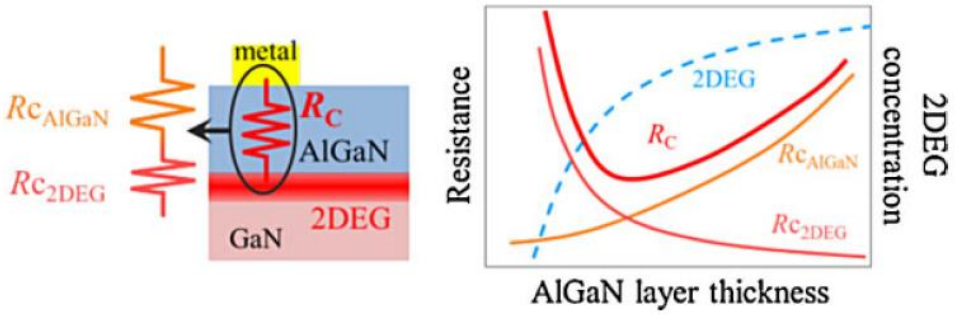

Fig. 3.2: The trade-off between contact resistance components and AlGaN layer thickness is depicted in schematic diagram. The 2DEG concentration is represented by a dashed line, while the resistances are represented by solid lines [20]

Thinning the AlGaN layer reduces the resistance of the layer (R_{cAlGaN}) but decreases the 2DEG concentration, leading to an increase in resistance at the connection to the 2DEG (R_{c2DEG}). On the other hand, thicker AlGaN layers increase the resistance of the AlGaN layer (R_{cAlGaN}) while maintaining a low connection resistance to the 2DEG (R_{c2DEG}). As a result, there is a lower limit to the overall contact resistance (R_c) due to this trade-off [20].

To compensate for this phenomenon various techniques are used, such as optimising the metal stack, surface treatments (cleans) and alloy processing. These can help to improve the metal-semiconductor interaction and reduce contact resistance while maintaining a high 2DEG concentration for optimal device performance.

3.3 Current transport mechanisms

When a metal and a semiconductor come into contact, their Fermi levels must align when in thermal equilibrium, as illustrated in Fig. 3.3 (b). Two scenarios can be considered to describe the interaction between a metal and a semiconductor: The ideal case, also known as the Schottky-Mott limit [21], and the practical case, referred to as the Bardeen limit [22]. Fig. 3.3 (a) portrays the energy band diagram for the ideal scenario (Schottky-Mott limit) [23]

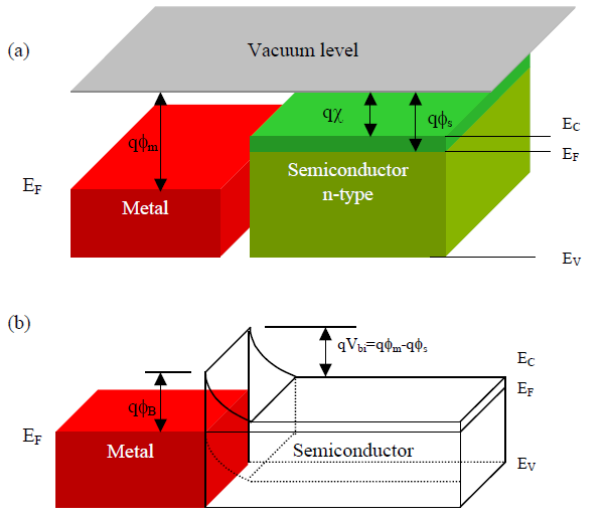

Fig. 3.3: The formation of a barrier between the metal and the semiconductor when (a) neutral and isolated and (b) in perfect contact without any oxide between them (Schottky-Mott limit) [23]

For this thesis the GaN HEMTs are metal to n-type semiconductors and the barrier height can be determined from the difference between the metal work function (Φ_m) and electron infinity (x_s).

$$q\phi_{Bn}=q(\phi_m - X_s) \tag{8}$$

For a given semiconductor and a metal, the sum of the barrier height on n- and p-type semiconductor is expected to be equal to the energy bandgap.

$$q(\phi_{Bn} + \phi_{Bp}) = E_g \tag{9}$$

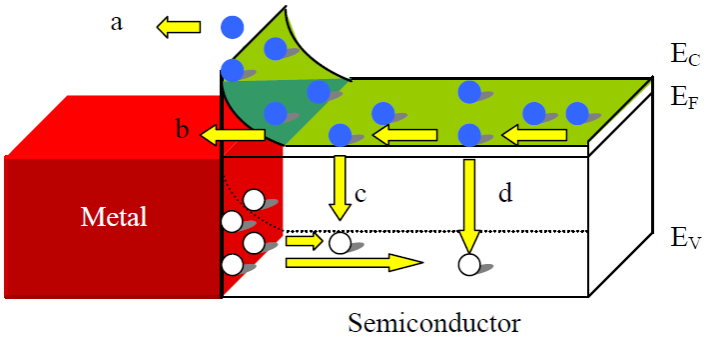

Fig. 3.4: Current transport processes in a forward biased Schottky barrier [23]

Fig. 3.4 shows 4 transport mechanism for n-type semiconductors in the forward bias condition. The four processes are a) emission of electrons from the semiconductor over the top of the barrier into the metal, b) quantum mechanical tunnelling through the barrier, c) recombination in the space-charge region, and d) recombination in the neutral region (called hole injection). For the lowly doped semiconductor, the current flows as a result of thermionic emission.

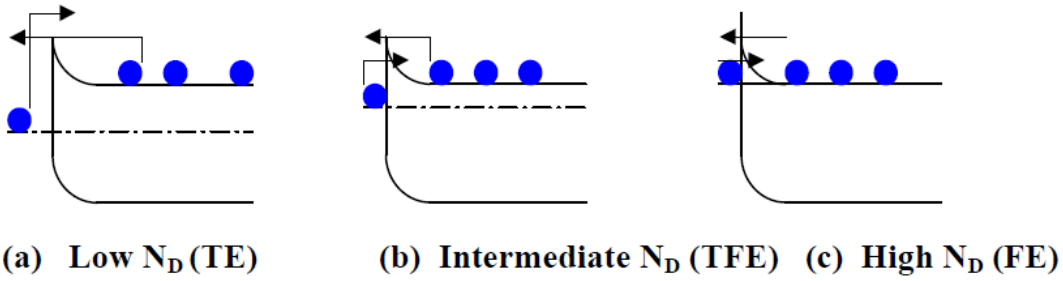

Fig. 3.5: Energy band diagram for (a) low doped, (b) intermediate doped, and (c) high doped n-type semiconductor. The arrow indicates the electron flow [23]

Fig. 3.5 above is a visual representation of a) a lightly doped semiconductor which would exhibit Thermionic Emission, b) a semiconductor which has intermediate doping would show Thermionic Field Emission and for high doping c) Field Emission would occur with direct tunnelling. Also, the characteristic energy of E_{00} (which is also a function of temperature and cannot be seen in the equation below) rules out the possibility of transport mechanism occurring, this parameter can be defined as [24]:

$$E_{00} = \frac{qh}{4\pi}\sqrt{\frac{N}{\varepsilon_0 \varepsilon_{GaN} m^*}} \qquad (10)$$

Where q is the electric charge, N is the doping concentration, ε_0 is the vacuum of permittivity, ε_{GaN} $(=9.5)$ and m^* $(=0.22m_e)$ are the permittivity and electron tunnelling effective mass of the semiconductor and h is Plank's constant. The comparison between E_{00} and the thermal energy kT *below* shows the mechanisms in dominant order:

$k_BT/q \ll E_{00}$ - Thermionic emission (TE)

$k_BT/q = E_{00}$ - Thermionic field emission (TFE)

$k_BT/q \gg E_{00}$ - Field emission (FE)

3.3.1 Thermionic emission

In lightly doped ($N_D<10^{17}cm^{-3}$) semiconductor materials the concentration of free electrons or holes is low. As a result, the density of states in the conduction band or valence band is also low, and the potential barrier at the metal-semiconductor interface is high. In this case, the rate of thermionic emission of electrons from the metal into the semiconductor is low because the probability of an electron having enough energy to overcome the potential barrier is also low. Therefore, the current flow in the device due to thermionic emission is also low. However, even in lightly doped semiconductor materials, thermionic emission can still occur if the temperature of the metal contact is high enough to provide the necessary thermal energy to the electrons. The amount of thermionic emission in this case is still low compared to heavily doped semiconductor materials, but it can still be significant in certain applications.

3.3.2 Thermionic field emission

Medium doping ($10^{17}<N_D<10^{20}cm^{-3}$) in a semiconductor material can lead to thermionic field emission, which is a combination of thermionic emission and field emission mechanisms. In a lightly doped semiconductor material, the potential barrier at the metal-semiconductor interface is high, and the rate of thermionic emission of electrons from the metal into the semiconductor is low. However, when the doping level is increased to a medium level, the potential barrier at the metal-semiconductor interface is reduced due to the higher concentration of free carriers. This increases the probability of thermionic emission of electrons from the metal into the semiconductor. In addition, when a high electric field is applied across the metal-semiconductor interface, the potential barrier can be further reduced. This can result in a significant increase in the rate of thermionic emission, as well as the additional emission of electrons due to the field emission mechanism.

The combined effect of thermionic and field emission mechanisms is called thermionic field emission, which can be a useful mechanism for injecting electrons into a semiconductor device. This mechanism is commonly used in field-effect transistors (FETs) and other electronic devices where a controlled injection of electrons is required. Thermionic field emission can also occur in heavily doped semiconductor materials, where the high concentration of free carriers leads to a low potential barrier at the metal-semiconductor interface. In this case, the field emission mechanism may

dominate, and the emission of electrons is enhanced by the high electric field across the interface.

3.3.3 Field emission

In a heavily doped ($N_D>10^{20}cm^{-3}$) semiconductor material, the concentration of free carriers is very high, and the potential barrier at the metal-semiconductor interface is very low. As a result, the probability of thermionic emission of electrons from the metal into the semiconductor is high, and the additional effect of electric field can lead to a strong field emission mechanism. In this case, the majority of electrons injected into the semiconductor device come from the field emission mechanism, which occurs when the high electric field at the metal-semiconductor interface causes electrons to tunnel through the potential barrier. The tunnelling process is assisted by the high density of states in the conduction band or valence band, as well as the high electric field. Field emission is a very efficient process for injecting electrons into a semiconductor device because it does not rely on thermal energy to overcome the potential barrier at the metal-semiconductor interface. This makes it suitable for applications that require high-speed operation or low power consumption. This makes field emission perfect for HEMTs.

3.4 Ohmic contacts

An ohmic contact is a metal/semiconductor interface that has very little resistance. The contact resistance R_C (Ω) depends on the overall contact size, so it is best to use the specific contact resistance ρ_c (Ω *x* cm^2) parameter which enables us to compare contacts separately from their geometry. The specific contact resistance ρ_c can be defined as [1]:

$$p_C = \left(\frac{\partial J}{\partial V}\right)^{-1}_{v\,=\,0}$$

(11)

Where *J* is the current density and *V* is the applied bias. The specific contact equation can vary on the current transport mechanism with regards to the doping levels. The specific contact resistance will also vary depending on the barrier height $q\Phi_B$ and temperature *T*. According to the classical expressions of current density at a metal, semiconductor interface the equations are given below as follows for, FE, TFE and TE [1]:

$$J_{FE} = \frac{A^{*}T\pi \exp\left[-q(\Phi_B - V_F)/E_{00}\right]}{C_1 k sin(\pi C_1 kT)}\left[1 - exp(-C_1 q V_F)\right]$$

(12)

$$With\ C_1 = \frac{1}{2E_{00}} \log\left[\frac{4(\Phi_{B-}V_F)}{-V_n}\right]$$

(13)

$$J_{TFE} = \frac{A^{*}T\sqrt{\pi E_{00} q(\Phi_B - V_n - V_F)}}{k cosh(E_{00}/kt)} exp\left[\frac{-qV_n}{kT} - \frac{q(\Phi_B - V_F)}{E_0}\right] exp\left(\frac{qV_F}{E_0}\right)$$

(14)

$$With\ E_0 = E_{00} \coth\left(E_{00}/kT\right)$$

(15)

$$J_{TE} = A^{*}T^2 exp\left(-\frac{q\Phi_B}{kT}\right)\left(e^{qV/nkT} - 1\right)$$

(16)

The three barrier height equations can be manipulated into the current density equation (Eq. 11) to extrapolate the specific contact resistance ***ρc*** for thermionic emission, thermion field emission and field emission:

$$\rho_{C-TE} = \frac{k}{A^{*}Tq} exp\left(\frac{q\Phi_B}{kT}\right)$$

(17)

$$\rho_{C-TFE} = \frac{k\sqrt{E_{00}} \cosh\left(E_{00}/kT\right)\coth\left(E_{00}/kT\right)}{A^{*}Tq\sqrt{\pi q(\Phi_B - V_n)}} exp\left[\frac{q(\Phi_B - V_n)}{E_{00}\coth\left(E_{00}/kT\right)}\right]$$

(18)

$$\rho_{C-FE} = \frac{k \sin\left(\pi C_1 kT\right)}{A^{*}Tq\pi} exp\left(\frac{q\Phi_B}{E_{00}}\right)$$

(19)

The most dominant tunnelling mechanism can be predicated by the calculation of the thermal energy normalised to the characteristic energy in the context of current transport mechanisms at a metal-semiconductor interface:

$$\frac{kT}{qE_{00}}$$

(20)

This equation shows the ratio between thermionic emission and the other two mechanisms, field emission and thermionic field emission.

$$E_{00} = \frac{h}{4\pi}\left(\frac{N_d}{m_\varepsilon}\right)^{1}/_{2}$$

(21)

Where *h* is Plank's constant, *m* is the effective mass and *ε* is the dielectric constant. Eq. 20 above shows the ratio between thermionic emission and the other two mechanisms. As previously discussed on page 13, when $kT/qE_{00} << 1$, thermionic emission is dominant. Field emission dominates when $kT/qE_{00} >> 1$ and when $kT/qE_{00} = 1$ thermionic filed emission is dominant. These three behaviours are shown in Fig. 3.6 below in which E_{00} is plotted as a function of the doping concentration [25]

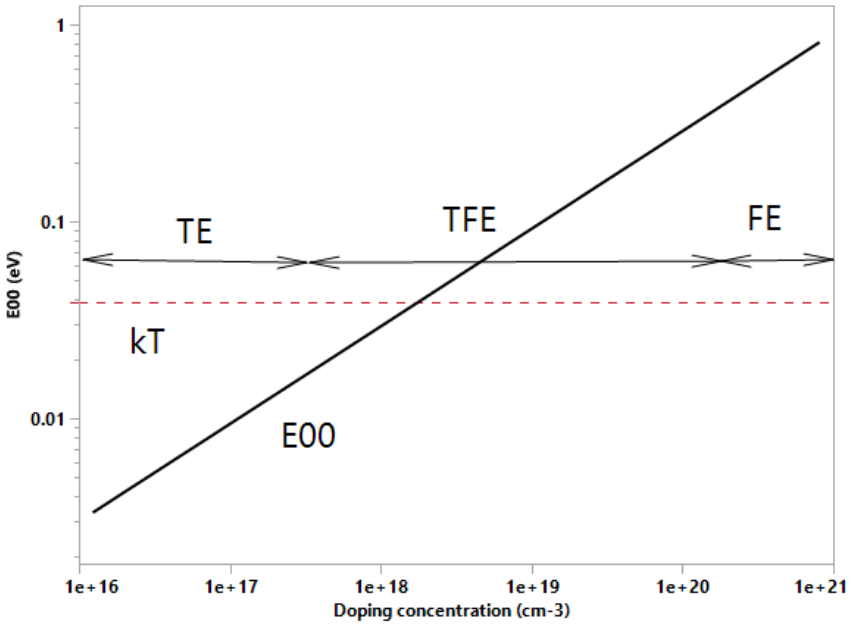

Fig. 3.6: E_{00} plotted as a function of doping concentration for GaN at T = 300K

Chapter 4: Characterisation and experimental techniques

This chapter describes the electrical characterisation and experimental techniques, used in the analysis of the wide band gap semiconductors for this thesis. All analyses were performed within the state-of-the-art Failure Analysis Laboratory at Nexperia Newport.

4.1 Energy dispersive x-ray analysis (EDX or EDS)

Energy Dispersive X-ray Analysis (EDX or EDS) is a technique used to analyse the elemental composition of a sample as shown in Fig. 4.1. It involves bombarding a sample with an electron beam, which causes the sample to emit X-rays. The X-rays emitted are then collected by a detector and analysed to determine the energy and intensity of the X-rays. In 1968 R. Fitzgerald, K. Keil, and K.F.J. Heinrich published a paper in Science [26] for an EDS system using a solid-state Si (Li) spectrometer with a resolution of 600eV. Today we expect silicon-based drift detectors (SDD) to feature active areas up to 1500mm^2 and a spectral energy resolution down to 120eV.

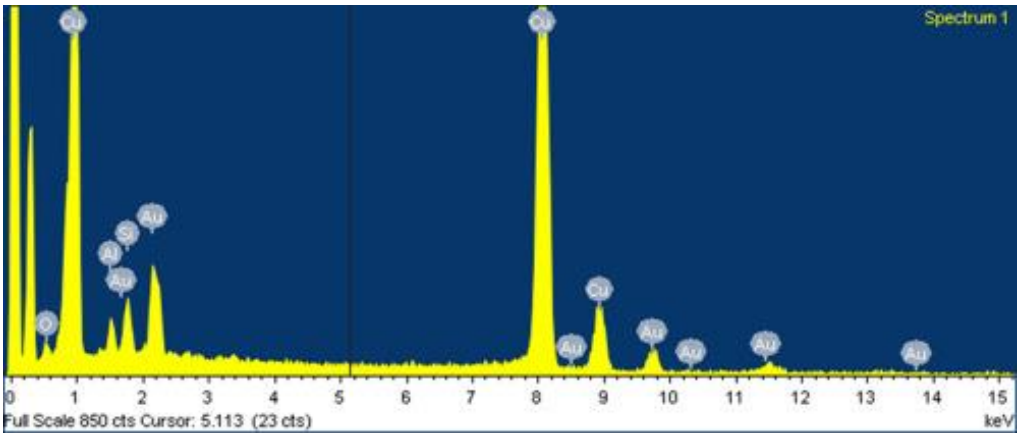

Fig. 4.1: Typical EDX spectra [26]

To understand how x-rays are generated we must remember that every atom has a varied number of electrons with specific energy levels. These electrons belong to certain shells, which have different, distinct energies.

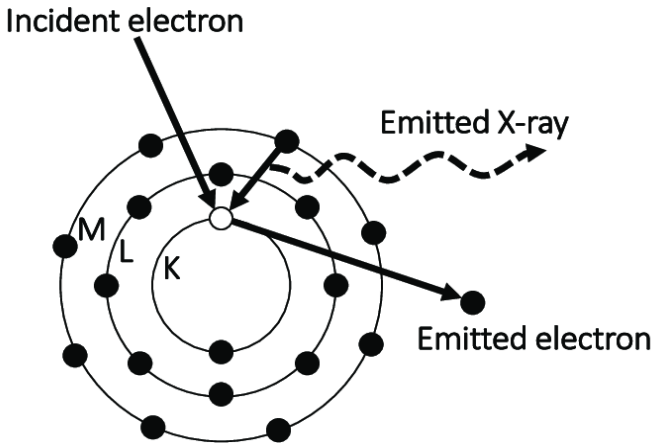

Fig. 4.2: Emission of characteristic x-ray [27]

When an electron beam hits the inner shell of an atom, Fig. 4.2 it knocks an electron off the shell and replaces it with a positively charged hole. As the electron is banished it attracts another electron from the outer shell to fill the hole. When this electron moves from the outer to the inner shell it creates an x-ray as the outer shell has a higher energy compared to the inner shell. This x-ray then has a distinct element and transition. These emitted x-rays are then collected by the collected and are interpreted into the spectrum that we see in Fig. 4.1. The Oxford Instruments INCA EDX tool incorporated into my Tescan Solaris [28] FIB-S/TEM tool can analyse sections produced from the FIB to show the distinct chemical composition of the HEMT layers.

4.2 Transmission electron microscopy (TEM)

A German physicist and electrical engineer called Ernst Ruska along with a colleague named Max Knoll invented the first Transmission Electron Microscope (TEM) back in 1931 at the University of Berlin. In their description of the tool, they described the process as "*A high-energy electron beam is focused onto the surface of the sample, and as the electrons interact with the sample, they produce various signals that can be detected to form an image".* Knolls and Ruska's work revolutionised our ability to image at the nanoscale and Ernst Ruska was subsequently awarded the Nobel prize in physics in 1986 [29].

TEM uses an electron beam to generate an image whereas light microscopes were traditionally used to generate an image. The maximum resolution (δ) of an optical device is proportional to the wavelength (λ) of the photons that are being used. *NA* is the numerical aperture.

$$\delta \approx \frac{\lambda}{2(NA)}$$

(22)

Light microscopes are limited to ~200nm resolution whilst todays sophisticated TEM's can perform at 0.23nm resolution. When De Broglie announced his theory on "Wave nature of electrons" it was realised that electrons can be used for imaging down to the nanoscale.

$$\lambda = \frac{h}{p}$$

(23)

The equation above shows that the wavelength (*λ*) of a particle is equal to Planck's constant (*h*) divided by the momentum (*p*) of the particle. For TEM to work the sample thickness (lamella) has to be milled down to <100nm for 100 – 300kV accelerating voltage TEM tools and down to >10nm for 30kV accelerating tools. Low voltage (30kV) TEM or STEM are excellent choices for sub <10nm lamella's as it provides a high scattering contrast. Low-voltage STEM with an aberration-corrected objective lens together with a high angle dark field (HADF) detector offers atomic resolution from sub >10nm lamellas.

The tool used in this thesis is a Solaris 30kV FIB S/TEM manufactured by Tescan [28]. The Solaris incorporates a UHR SEM with TriLens™ immersion optics. The Triglav™ SEM column features TriLens™, a three-lens compound objective system that enables both an ultra-high-resolution (UHR) immersion imaging mode and a high-throughput analytical mode. The UHR mode can be combined in a unique way with a crossover-free configuration, resulting in reduced aberrations and a significant improvement in beam performance at low beam energies. Moreover, immersion optics technology remains the best choice for STEM and microanalysis, delivering a 0.5 nm resolution at 30 keV electron beam energy. Microanalysis (i.e., EDS, EBSD) is performed in the field-free analytical mode. Field-free analytical mode is ideal for morphological characterization of magnetic samples. This analytical mode also provides a large field of view for fast, smooth, and easy navigation across the sample surface [30]

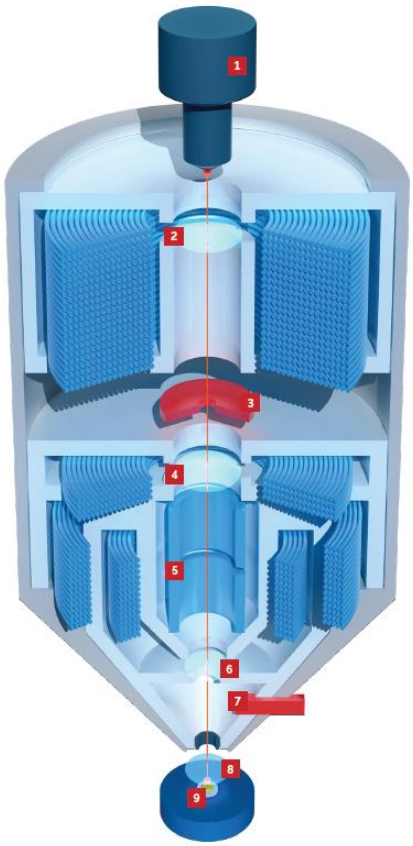

Fig. 4.3: Tescan Triglav SEM column: 1. Field emission source, 2. Condenser lens, 3. In-Beam BSE, 4. Third objective lens, 5. Stigmators, 6. Analytical objective lens, 7. In-Beam SE, 8. UH-Resolution objective lens, 9. Sample [30]

4.3 Electrical characterisation

The parameter most frequently used to describe ohmic contacts is the specific contact resistance ρc (Ωcm^2). There are various techniques which can be used to obtain contact resistance between metal and semiconductor, but the Transmission Line Method (TLM) is probably the most common. The TLM technique was first introduced by Shockley [31] and has been in common use since its inception around 1964. By using the TLM method you can successfully measure the metal contact resistance (R_M), contact resistance (R_C), specific contact resistance (ρc), sheet resistance (R_S), thickness of the material (t) and transfer length (L_T). The diagram below shows the TLM schematically.

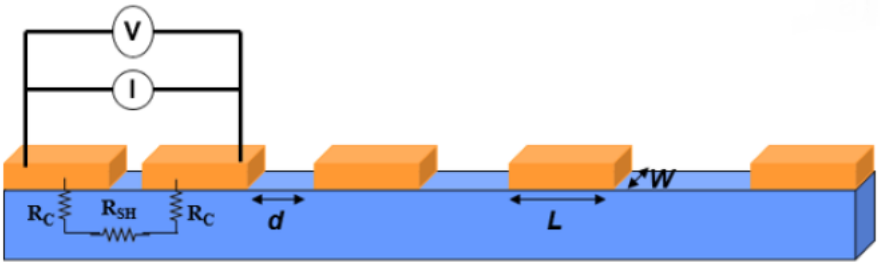

Fig. 4.4: Schematic diagram of TLM structure [1]

The TLM structure is similar to a ladder and is sometimes referred to as the ladder structure. The TLM structure contains metal contacts which are identical in area (L x W) with varying spaces (d) between each contact. As shown in figure 4.5 above there is a singular blue rectangle of doped area that has the same sheet resistance as the contact areas of the device. Metal contacts, orange in colour is formed over the doped region.

4.3.1 Sheet resistance (R_{sh})

When a semiconductor is homogeneous and rectangular in shape the resistance and sheet resistance can be expressed as:

$$R = \rho \frac{L}{tW} \tag{24}$$

$$R_{sh} = \frac{\rho}{t} \tag{25}$$

Where ρ, L, t and W represents the resistivity, length, thickness, and width of the semiconductor. R is used to calculate the total resistance of bulk materials based on their geometry, while R_{sh} represents the sheet resistance of thin films, which depends only on material resistivity and thickness whilst R_{semi} represents the bulk resistance of semiconductor materials in ohms, accounting for geometry and dimensions.

4.3.2 Contact resistance (R_C)

The plot of R_{tot} is shown in figure 4.5, R_{tot} is the accumulation of several components, R_m which is the resistance of the contact metal, R_{semi} which is the semiconductor resistance and R_c which is the contact resistance between the metal and the

semiconductor. From fig. 4.5 R_c and R_{tot} can be obtained an extrapolation at the point of zero *d = 0* represents $2R_c$, R_{tot} can also be expressed by the following equation:

$$R_{tot} = 2R_m + 2R_c + R_{semi} \quad (26)$$

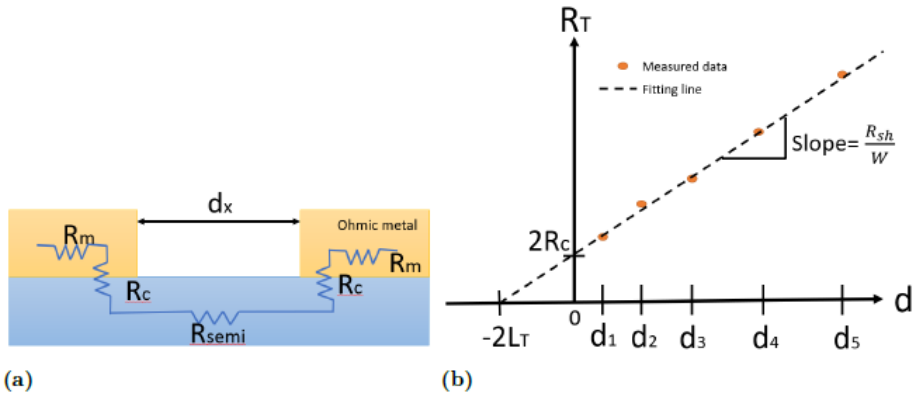

Fig. 4.5: (a) Schematic of the different components of R_{tot} (b) Total resistance R_{tot} plotted as a function of dx [25]

In general, the contact metal resistance R_m is usually smaller than the contact R_c and can be safely ignored. The slope of the line represents the sheet resistance R_{sh} and thus R_{tot} can be expressed by the following equation:

$$R_c >> R_m \quad (27)$$

$$R_{semi} = \frac{R_{sh}}{W} d \quad (28)$$

$$R_{tot} = 2R_c + \frac{R_{sh}}{W} d \quad (29)$$

4.3.3 Transfer length (L_T)

The transfer length is where the voltage, caused by current transferring between semiconductor and metal contacts, drops to *1/e* of its maximum value, which is at the contact edge. The transfer length is dependent on specific contact resistance and sheet resistance shown in fig. 4.6, and the relation can be expressed as:

$$L_T = \sqrt{\frac{\rho_c}{R_{sh}}}$$

(30)

4.3.4 Specific contact resistance (ρc)

Specific contact resistivity, p_C, is usually measured in Ωcm^2 which is independent of contact area or geometry. It can be defined as:

$$p_C = \left(\frac{\partial J}{\partial V}\right)^{-1}_{v\,=\,0}$$

(31)

The specific contact resistance contains the contact resistivity of both the interface and the regions above and below it, p_C can also be determined directly by the contact resistance R_C, transfer length L_T and the width of contact pads. It can be expressed as:

$$p_c = R_C L_T W = R_C A_{eff}$$

(32)

A_{eff} in the equation is the effective contact area. The contact area is always different from the A_{eff} due to the current crowding effect. The current going through the semiconductor is uniform; however, the current flow is not uniform through the metal contacts. Since the current flows through the metal contacts with low resistance, and therefore, the current density at the edge of the contacts is higher and drops to zero at the far edge.

Fig. 4.6: Current flow through contact for high and low p_C [25]

4.3.5 Two-point probe method over four-point probe method

The two-probe method for contact resistance measurements using the transfer length method offers distinct advantages over the four-probe method. Firstly, its simplicity and ease of setup make it a practical choice. With only two probes required, the two-probe method simplifies the measurement process, saving time and effort. This simplicity is particularly advantageous for quick assessments or situations where a straightforward setup is desired. Additionally, the reduced equipment requirement of the two-probe method can be cost-effective, making it more accessible for applications with budget constraints or limited resources. This affordability can be especially relevant for smaller projects or when a comprehensive four-probe setup is not essential.

Furthermore, the two-probe method can still provide meaningful results for comparative analysis. While it is sensitive to contact resistance, maintaining consistent measurement conditions allows for relative differences to be observed between samples. In situations where the primary goal is to compare different samples or assess changes in contact resistance relative to a reference, the two-probe method can offer practicality and insights. The two-probe method can be a viable option for scenarios where a comprehensive four-probe setup may not be necessary or feasible.

In the case of this thesis a two-probe set-up was chosen over a four-probe set-up due to the bench tester being a manual piece of equipment. The probes have to be manually lowered and risen in the Y direction and the probes also have to be manually moved in the X direction so that the probe tips sit neatly in the metal pads as the width increases from the 2µm spacing (d) up to the 25µm spacing.

The four-probe analysis would provide slightly better accuracy but at a cost in monetary value in purchasing the extra micromanipulators, cables and probes and an extra cost in time. By performing the two-probe analysis the probes were manually moved 3240 times. As stated above the bench tester is a manual piece of kit and the wafers had already been removed from the cleanroom so the automated testers in the probe area could not be utilised. if the four-probe method was used then this would be 6480 times the probes would have to be manually moved.

Chapter 5: Epitaxial wafers

As discussed in chapter 2, the characteristics required for high electron mobility transistors based on AlGaN/GaN heterostructures rely on the properties of the substrate used for their epitaxial growth.

GaN substrates play a crucial role in device performance, and different types offer distinct advantages and challenges. Bulk GaN substrates exhibit high crystal quality, low defect density, and excellent thermal conductivity, but are expensive and limited in availability. GaN-on-Si substrates provide cost-effectiveness and compatibility with silicon-based processes yet face lattice and thermal mismatch issues. GaN-on-Sapphire substrates offer good lattice matching and epitaxial growth quality but can experience thermal expansion mismatch and heat dissipation challenges. GaN-on-SiC substrates excel in thermal conductivity and breakdown voltage yet are costlier and may have limited availability. When selecting a GaN substrate, engineers must consider specific application requirements, scalability, cost, and fabrication processes. The choice must strike a balance between material properties, device performance, and cost considerations.

GaN layers for device applications are typically grown by various methods, MBE (molecular beam epitaxy), MOCVD (metal-organic chemical vapor deposition) or HVPE (hydride vapor phase epitaxy). The GaN layers and AlGaN/GaN heterostructures used in this thesis were grown on CZ p-type Si (111) substrates. CZ silicon refers to Czochralski silicon, which is a type of single-crystal silicon grown using the Czochralski (CZ) process, the Czochralski process is a method for growing high-purity single-crystal silicon by pulling a crystal seed from molten silicon. CZ Silicon is a widely used material in semiconductor fabrication, offering a balance between cost, scalability, and performance. Trimethylgallium, trimethylaluminum and ammonia were used as precursors for gallium, aluminium, and nitrogen respectively. Next, an AlN buffer was deposited followed by a single thick AlGaN intermediate layer and a thick GaN layer.

Two sets of twenty-five wafers were provided by our EPI vendor to Nexperia Newport for processing through the cleanroom. The first set of twenty-five wafers has seven individual layers with layer one being an unintentionally doped layer of AlN *(see Table 5.1 for details).* The second batch of twenty-five wafers has five individual layers with

layer one being an unintentionally doped nucleation layer *(see Table 5.2 for details).* An initial three wafers will be split out from either batch at the end of the fabrication process for characterisation of contact resistance, sheet resistance and specific resistance. The layer structure provided by the epitaxial vendor for the wafers have been placed into the two tables below.

From the first batch of EPI wafers, wafers 1, 2 and 3 (AlN) will be used for electrical testing after the fabrication process is complete.

Table 5.1: Epitaxial layers for batch 1, wafers 1, 2 and 3 (AlN)

Layer	Type	Material	Mole Fraction (x)	Thickness [nm]	Dopant
7	UID	GaN		3	
6	UID	Al(x)GaN	25%	20	
5	UID	AlN		0.5	
4	UID	GaN		400	
3	SI	GaN		900	carbon
2	SI	GaN/AlGaN buffer		2750	carbon
1	UID	AlN		180	
CZ Si (111) p-type (1150000nm)					

Fig. 5.1 shows the structure of wafers 1, 2 and 3 after processing. A TEM was performed on wafer 3 (AlN) to highlight the 7 layers.

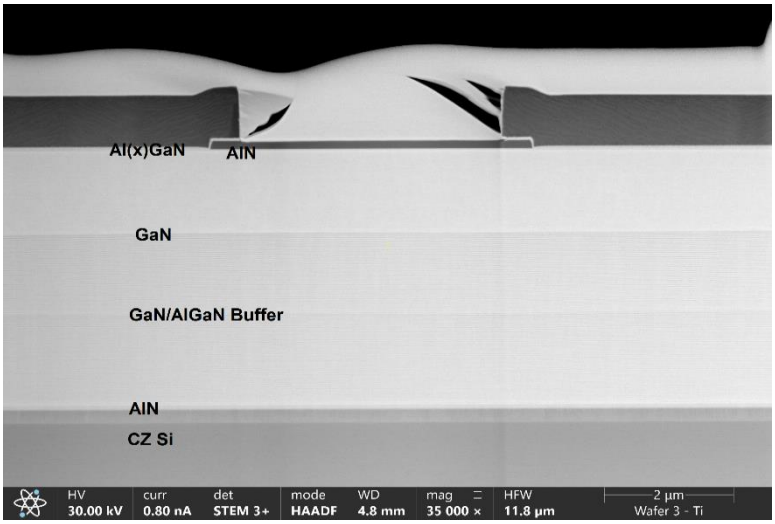

Fig. 5.1: TEM image of wafer 3 (AlN) showing the individual layers of the device

From the second batch of EPI wafers, wafers 7, 8 and 9 (Nucleation) will be used for electrical testing after the fabrication process is complete.

Table 5.2: Epitaxial layers for batch 1, wafers 1, 2 and 3 (Nucleation)

Layer	Type	Material	Mole Fraction (x)	Thickness [nm]	Dopant
5	UID	GaN		3	
4	UID	Al(x)GaN	25%	28	
3	UID	GaN		400	
2	SI	GaN/AlGaN buffer		3650	carbon
1	UID	Nucleation		180	
CZ Si (111) p-type (1150000nm)					

Fig. 5.2 shows the structure of wafers 7, 8 and 9 (Nucleation). A TEM was performed on wafer 9 (Nucleation) to highlight the 5 layers. TEM image of wafer 9 (Nucleation) showing the individual layers of the device.

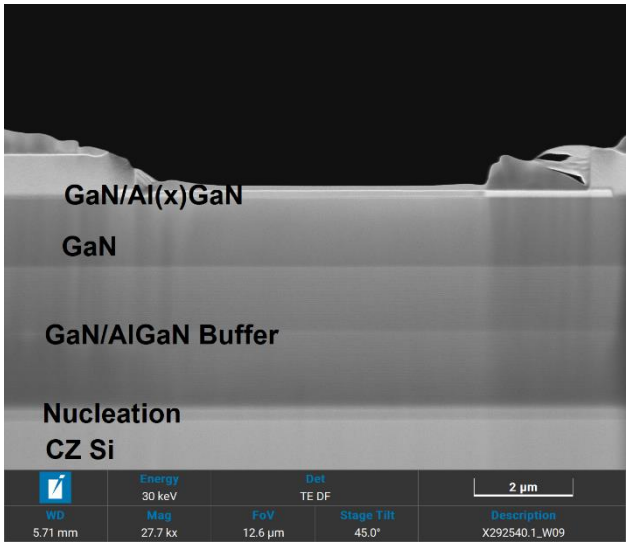

Fig. 5.2: TEM image of wafer 9 (Nucleation) showing the individual layers of the device

The individual layers of these wafers are detailed in Tables 5.1 and 5.2. Cross-sectional TEM images of the wafers are presented in Figures 5.1 and 5.2. These TEM images were captured at low magnification to provide an overview of the entire structures. However, some of the individual layers and films within the devices are only a few nanometers (nm) thick. The imagery of these ultra-thin films would require a high-resolution TEM operating at 300 kV with a magnification greater than 500,000x.

For wafers 7, 8 and 9 nucleation refers to the initial formation of a crystal structure during the growth process. Nucleation occurs when atoms or molecules come together to form a small seed crystal, known as a nucleus. In GaN semiconductor fabrication, nucleation is a critical step in the epitaxial growth process, where a thin layer of GaN is deposited on a substrate.

During the process of nucleation, the atoms or molecules in the vapor phase condense onto the substrate surface, adhering to it and forming tiny crystals. The nucleation step is paramount, as it can significantly impact the crystal lattice, defect quantity, and overall performance of the GaN semiconductor. Correct control of nucleation parameters, such as temperature, pressure, and growth conditions, is required to achieve uniform high-quality GaN layers with desirable properties for various electronic applications.

On the other hand, for wafers 1, 2 and 3, an AlN nucleation layer specifically refers to a nucleation layer composed of aluminium nitride. Aluminium nitride is a wide-bandgap semiconductor material that is commonly used as a buffer or nucleation layer in the growth of gallium nitride (GaN) semiconductors. The AlN nucleation layer helps promote the growth of high-quality GaN layers by providing a smooth, lattice-matched interface between the GaN and the substrate.

Chapter 6: Fabrication

The wafers were processed through a class 10 semiconductor fabrication facility based in Newport South Wales. The plant broke ground as INMOS back in 1980 and was completed in 1982. The facility now manufactures power MOSFETs, IGBTs, Diodes and ICs for various global customers along with manufacturing power devices for itself. The site is fully certified for IAFT16949 and ISO9001.

A semiconductor wafer fabrication plant, commonly referred to as a fab, is a highly specialized manufacturing facility dedicated to the intricate process of creating integrated circuits (ICs) and other semiconductor devices on silicon wafers. These wafers serve as the foundational substrate upon which electronic components are etched, deposited, and interconnected to form functional microelectronic devices. The fabrication process involves a series of meticulously controlled steps, each contributing to the intricate construction of transistors, diodes, resistors, and other essential elements that constitute modern electronic systems.

The fabrication process typically begins with the production of pure silicon wafers, which are then subjected to a sequence of photolithography, etching, deposition, and ion implantation processes. Photolithography involves projecting intricate patterns onto the wafer's surface using specialized masks, dictating the arrangement of transistors and circuitry. Etching and deposition processes selectively remove or add material to the wafer, creating intricate structures with nanoscale precision. Ion implantation introduces controlled impurities to create distinct electrical properties within specific regions of the semiconductor material. As the fabrication progresses, multiple layers of materials are stacked and interconnected, forming complex three-dimensional structures that collectively constitute advanced microchips. The entire process demands an environment of extreme cleanliness, precision, and control, often requiring specialized cleanrooms to prevent contamination that could compromise the final product's functionality.

6.1 Graphical data stream (GDS)

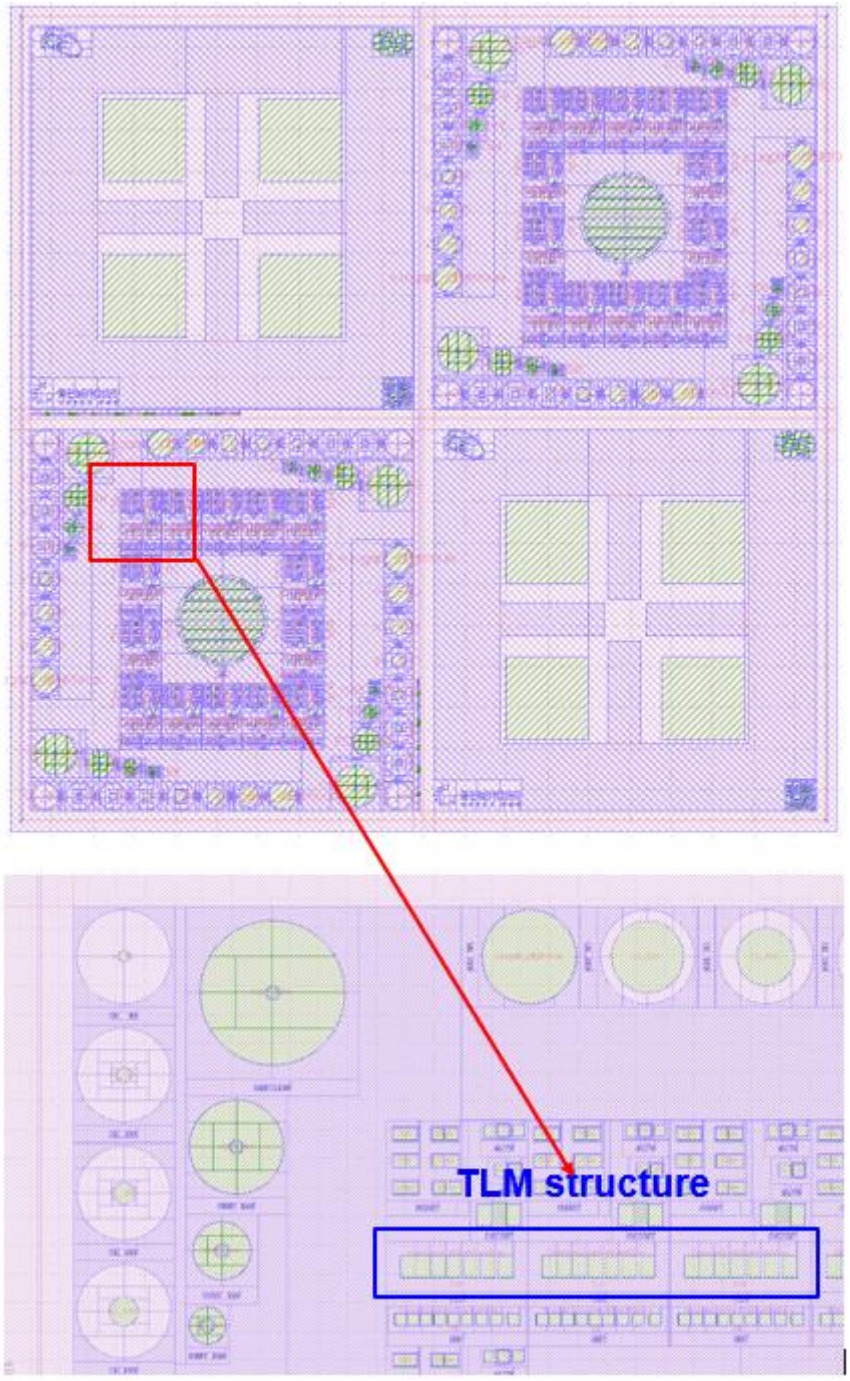

Fig. 6.1: Graphical data stream of reticle frame

The provided image above displays the reticle frame, which will undergo processing on the wafers. The reticle frame repeats 61 times across the entire eight-inch wafer. In the clean room fabrication plant, multiple process steps are involved in the design, which will be explained in detail later in the report. Within a single reticle, the TLM structure, used for measurement, is repeated three times. Any of these TLM structures

can be employed for our measurement purposes, the dimensions of the TLM structures are given in section 6.2. To account for potential misprocessing during manufacturing steps, multiple structures are fabricated. This ensures the final fabricated wafers consistently possess reliable TLM structures for electrical characterisation on the bench tester.

6.2 Transmission line method (TLM)

The TLM was covered in chapter 4.4 regarding electrical characterisation. Fig. 6.2 below shows the dimensions of the TLM pads from the GDS data.

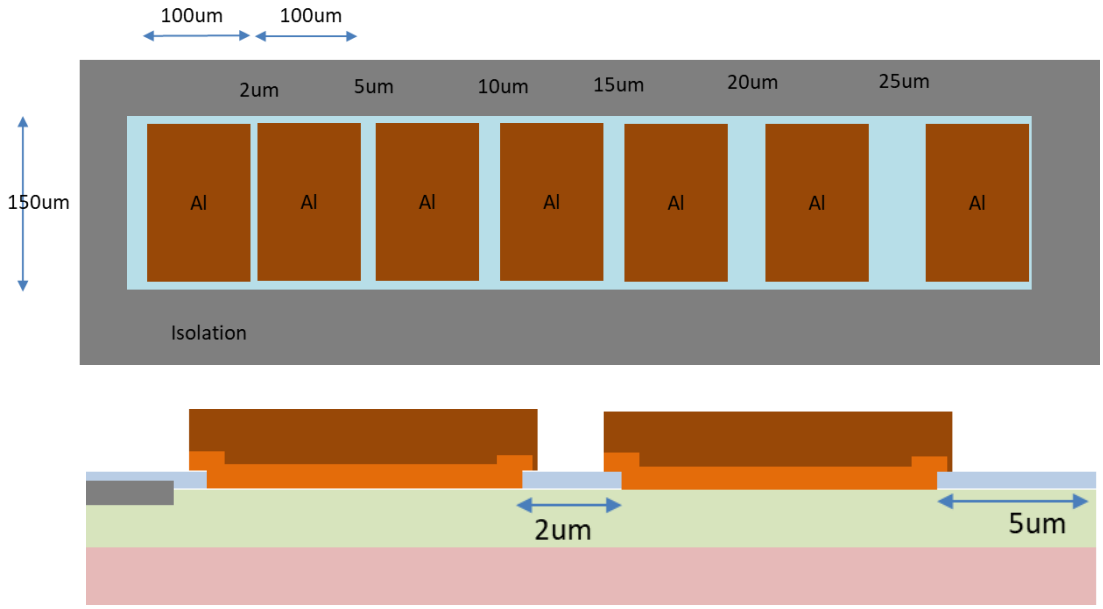

Fig. 6.2: TLM structure, pads, and dimensions

The dimensions shown above are the exact measurements taken from the GDS and the semiconductor design Engineers concept drawings. The TLM structures will have aluminium pad sizes of 100µm × 150µm with contact gaps of 2µm, 5µm, 10µm, 15µm, 20µm and 25µm isolated from the rest of the device.

6.2.1 Transmission line method (TLM) and not circular transmission line method (CTLM)

While the Transmission Line Method (TLM) was chosen for this thesis due to its compatibility with rectangular and square geometries of the gate and source pads, it is important to note that the Circular Transmission Line Method (CTLM) also offers distinct advantages. CTLM eliminates alignment issues due to its radial symmetry, provides more accurate measurements by minimising edge effects, and requires no sample cleaving, making it suitable for compact layouts and non-rectangular

geometries. However, given the rectangular nature of the final device design in this study, TLM remains the most suitable method for achieving accurate results.

6.3 Wafer metal splits

As discussed earlier in chapter 5, three wafers, wafers 1, 2 and 3 (batch 1) will be fabricated with different layers of GaN compounds as compared to wafers 7, 8 and 9 (batch 2). These EPI variations will also have wafer splits during the metallisation deposition. The table below shows the metal splits that will be performed.

Table 6.1: Metal pad splits

Wafer #	Dielectric	Ohmic Metal	Ohmic Anneal
W07	1400Å SiNx (LPCVD)	400ÅTa / 2000Å Pure Al	600°C, 60s
W08	1400Å SiNx (LPCVD)	250ÅTi / 3000Å AlCu	600°C, 60s
W09	1400Å SiNx (LPCVD)	250ÅTi / 3000Å Pure Al	600°C, 60s
W01	1400Å SiNx (LPCVD)	400ÅTa / 2000Å Pure Al	600°C, 60s
W02	1400Å SiNx (LPCVD)	250ÅTi / 3000Å AlCu	600°C, 60s
W03	1400Å SiNx (LPCVD)	250ÅTi / 3000Å Pure Al	600°C, 60s

The metal pad splits will sit on top of the epitaxial splits. All 6 wafers will receive the same dielectric deposition along with the same ohmic annealing temperature of 600°C for 60s.

Table 6.2: EPI splits and ohmic metal splits

Wafer #	Epi	Ohmic Metal
W07	Nucleation, GaN/AlGaN buffer & GaN	400ÅTa / 2000Å Pure Al
W08	Nucleation, GaN/AlGaN buffer & GaN	250ÅTi / 3000Å AlCu
W09	Nucleation, GaN/AlGaN buffer & GaN	250ÅTi / 3000Å Pure Al
W01	AlN, GaN/AlGaN buffer & GaN	400ÅTa / 2000Å Pure Al
W02	AlN, GaN/AlGaN buffer & GaN	250ÅTi / 3000Å AlCu
W03	AlN, GaN/AlGaN buffer & GaN	250ÅTi / 3000Å Pure Al

The EPI splits and ohmic metal splits of Titanium and Tantalum will provide the AlN and nucleation splits with varying metal depositions.

In chapter 2.1, it is stated that AlGaN/GaN heterostructures are highly intriguing systems used for creating high electron mobility transistors (HEMTs). To enhance the performance of HEMT devices, it is necessary to have good source and drain ohmic contacts that exhibit low specific resistance. Additionally, in GaN-on-Si technology, it is crucial to develop ohmic contacts that do not contain Gold *(As discussed in chapter*

3 literature review). Gold-free ohmic contacts are essential in GaN-on-Si technology to ensure compatibility with CMOS fabrication processes, as gold (Au) can diffuse into silicon at elevated temperatures, leading to contamination and device failure. Additionally, eliminating gold reduces costs and improves thermal stability, making the process more suitable for high-volume manufacturing in power electronics and automotive applications [17]. This thesis focuses on the investigation of Au-free ohmic contacts, specifically comparing contacts based on titanium (Ti) and tantalum (Ta). The research explores the structural, morphological, and electrical characteristics of these contacts and offers insights into the mechanism of carrier transport at the interface between the metal and the semiconductor [1].

6.4 Fabrication process

To fabricate the six wafers through the FAB we used the four steps of processing, they are layering, patterning, doping, and heat treatments.

- **Layering**: The operation used to add thin layers to the wafer surface.
- **Patterning**: the series of steps that results in the removal of selected portions of the added surface layers.
- **Doping**: the process that puts specific amounts of electrically active dopants in the wafer surface through openings in the surface layers.
- **Annealing**: Heat treatments are the operations in which the wafer is simply heated and cooled to achieve specific results

The table below shows the steps required to fabricate the metal pads through the cleanroom.

Table 6.3: Mask levels and fabrication steps for ohmic contacts

MASK	STEP	TASK	PROCESS	TOOL	DESCRIPTION
1	1	SiN Deposition	140nm LPCVD Nitride	TEL mark8	Coater & developer
	2	Zero Photo	Alignment mark photo	Nikon i14	Photo stepper
	3	Zero Etch	Alignment etch (nitride + ~500nm into GaN)	SPTS ICP + AMAT DPS	Oxide and metal etch
	4	Ohmic Window Photo	Ohmic window photo (S/D photo)	Nikon i14	Photo stepper
2	5	Ohmic Window Etch	S/D Etch soft landing on AlGaN	SPTS ICP	Oxide etch
	6	Pre Metal Clean	O2 ash & DSP (dilute sulphur peroxide) clean	Gasonics + Akrion	Plasma clean
	7	Metal Deposition	Ti/Al or Ta/Al Ta deposition	AMAT Endura	Metal deposition
	8	Metal Annealing	Ohmic anneal	RTP	Annealing
	9	Pre Metal Clean	O2 ash & DSP (dilute sulphur peroxide) clean	Gasonics + Akrion	Plasma clean
	10	Metal Deposition	Ti/Al dep	AMAT Endura	Metal deposition
3	11	Metal Photo	Metal photo	Nikon i14	Photo stepper
	12	Metal Etch	Metal etch	AMAT DPS	RIE etch
4	13	Isolation Photo	Isolation photo	Nikon i14	Photo stepper
	14	Isolation Implant	Isolation implant	Axcelis GSD	Implantation
	15	Isolation Strip	O2 ash & DSP (dilute sulphur peroxide) clean	Gasonics + Akrion	Plasma clean

The four-mask process for creating PCM structures in semiconductor manufacturing involves several sequential steps. In mask 1, Fig. 6.3, a 140nm LPCVD nitride layer is deposited using the TEL mark8 coater and developer. Subsequently, alignment marks are exposed through a photo stepper (Nikon i14) in the zero-photo step. This is followed by alignment etching of nitride and approximately 500nm into GaN using SPTS ICP and AMAT DPS tools in the zero etch step. In the ohmic window photo step, the ohmic window (source/drain) areas are exposed using a photo stepper.

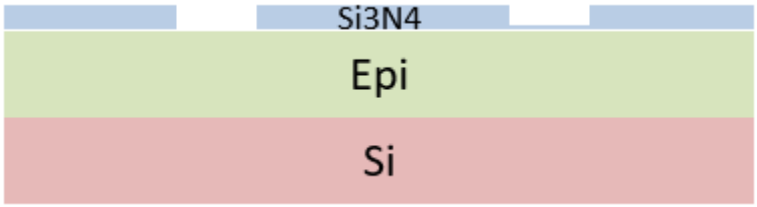

Fig. 6.3: Mask layer 1

Mask 2, Fig. 6.4 below, commences with the soft-landing etching of the oxide layer in the source/drain regions through SPTS ICP in the ohmic window etch step. The pre-metal clean step involves O2 ash and DSP (dilute sulphur peroxide) cleaning using Gasonics and Akrion tools. Next, metal deposition is performed using Ti/Al or Ta/Al Ta through the AMAT Endura tool in the metal deposition step. Ohmic annealing is conducted using RTP for enhancing the electrical properties of the metal contacts. Another round of pre metal clean is carried out before the final metal deposition of Ti/Al through the AMAT Endura tool.

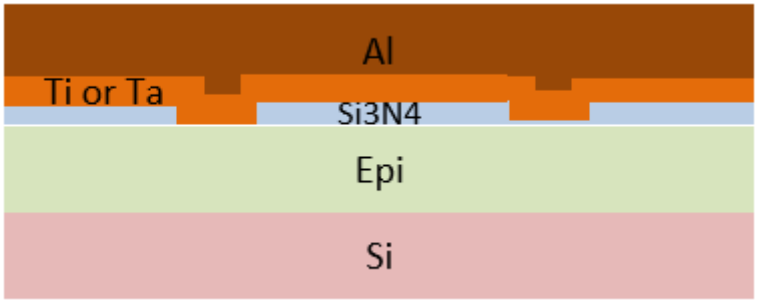

Fig. 6.4: Mask layer 2

Moving to mask 3, Fig. 6.5, the metal layer is patterned through exposure using the Nikon i14 photo stepper in the metal photo step. Subsequently, the unwanted metal layers are etched using AMAT DPS (Deep Reactive Ion Etch) in the metal etch step.

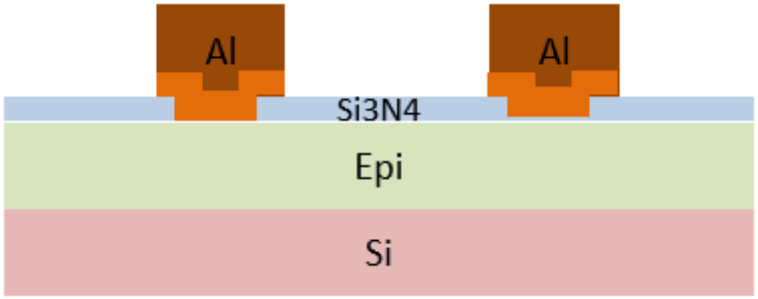

Fig. 6.5: Mask layer 3

Mask 4, Fig. 6.6 begins with the isolation regions being exposed through a photo stepper in the isolation photo step. Isolation implantation is performed using the Axcelis GSD tool, and finally, isolation striping is carried out through O2 ash and DSP cleaning using Gasonics and Akrion tools.

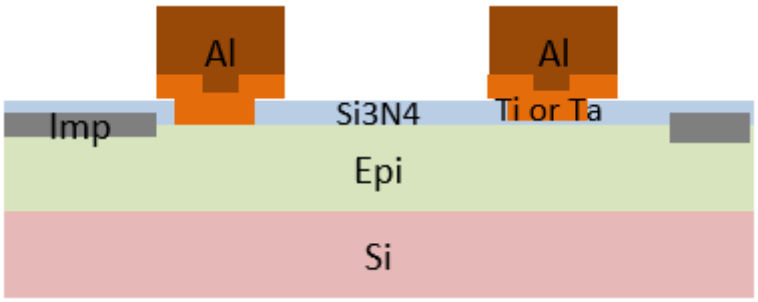

Fig. 6.6: Mask layer 4

After the fabrication process the wafers can be removed from the cleanroom for electrical and mechanical characterisation.

6.5 Optical images of completed wafers

The set of six AlGaN/GaN on Si HEMT wafers have undergone complete processing in a controlled environment and are now prepared for electrical testing. Prior to testing, photographs have been captured using a camera, along with high-powered optical images obtained from the Leica optical microscope within the Failure Analysis laboratory.

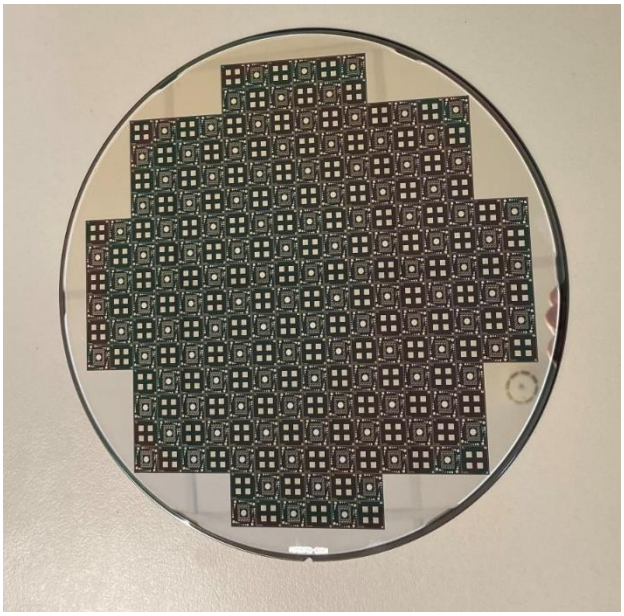

Fig. 6.7: Photograph of completed wafer

As per the GDS reference earlier in the thesis we can now match that up to the camera image of the reticle.

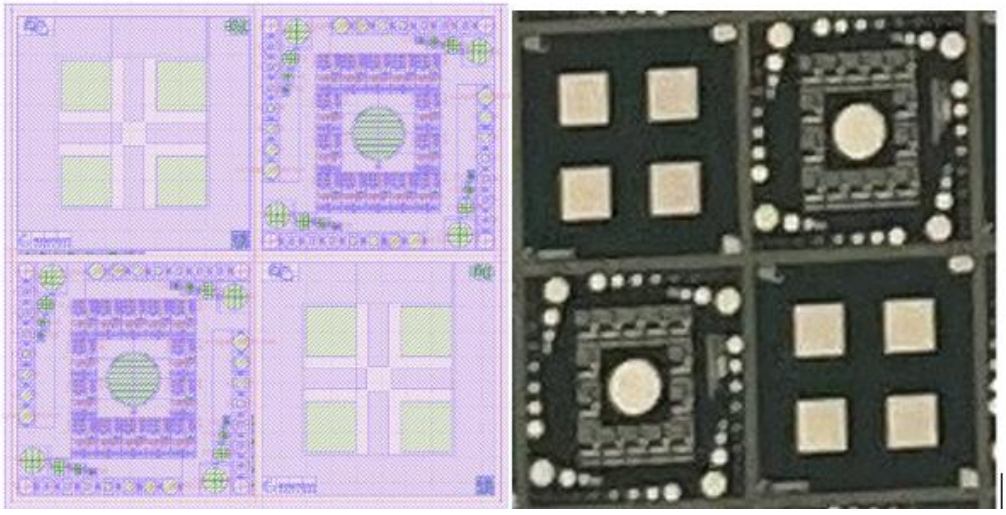

Fig. 6.8: GDS and optical image of reticle

The electrical characterisation will be performed on the TLM test structures that have been developed in the FAB. High magnification images of these pads have been taken for reference.

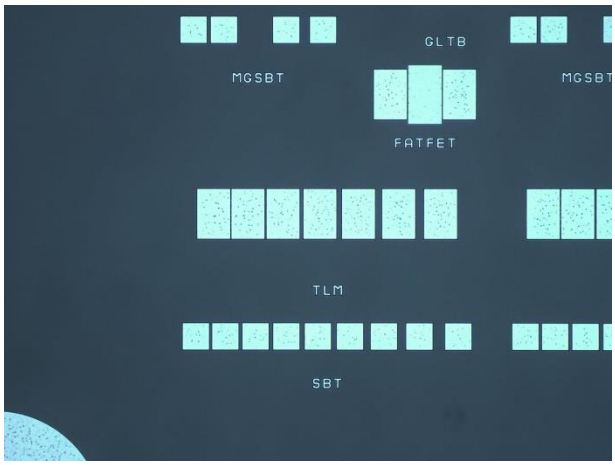

Fig. 6.9: Low magnification of TLM structure

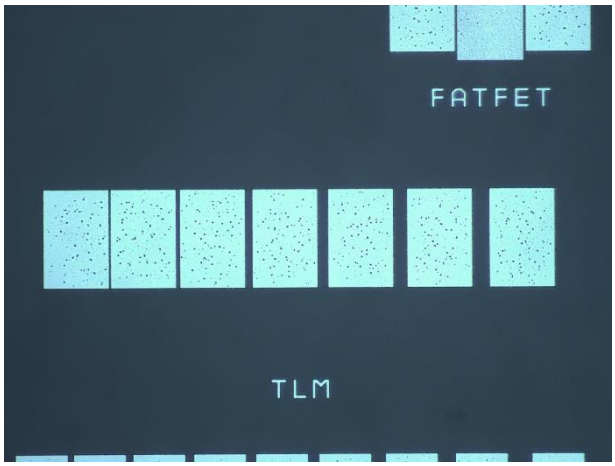

Fig. 6.10: Medium magnification of TLM structure

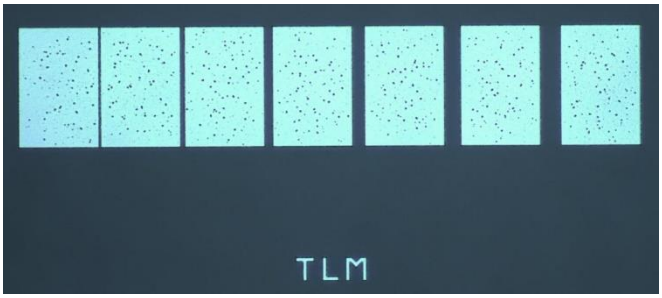

Fig. 6.11: High mag image of TLM structure

Fig. 6.9 above shows the aluminium pad sizes of 100µm × 150µm with contact gaps of 2µm, 5µm, 10µm, 15µm, 20µm and 25µm.

Chapter 7: Characterisation

This chapter presents a comprehensive evaluation of ohmic contacts composed of pure aluminium (pure Al), aluminium copper (AlCu), tantalum (Ta), and titanium (Ti) on two variations of GaN-based HEMTs, as described in detail throughout Chapter 6. The Transmission Line Method (TLM) technique is used to explore the influences of increasing temperatures on the electrical properties of ohmic contacts to GaN devices from the range of 300°K to 400°K in incremental values of 25°K. Ohmic contacts were fabricated onto the GaN substrate, with the layer composition detailed in Tables 5.1 and 5.2. The metallisation and subsequent post-annealing treatments are systematically presented in Table 6.1. All contacts underwent annealing at a maximum temperature of 600°C for 60s. FIB, TEM and EDX will provide visual and elemental confirmation of the contact's structural integrity post a 600°C annealing process, highlighting the robustness of the fabrication methodology. Specific contact resistivity (ρ_C) was extracted from the electrical data measured at the centre, mid-radius, and the edge of the wafer at various increasing temperatures (300°K, 325°K, 350°K, 375°K and 400°K) for contacts made from pure Al, AlSiCu, Ti, and Ta, with a focus on the temperature profile of 400°K. The focus on measurements at 400°K in this study is driven by its relevance to the practical operating conditions of GaN-based HEMTs, which are frequently used in high-power and high-temperature applications. Testing at this elevated temperature simulates real-world thermal stresses, enabling a thorough evaluation of contact reliability and performance. At 400°K, the thermionic field emission (TFE) model becomes highly applicable, providing insights into carrier transport mechanisms where both thermal excitation and quantum tunnelling contribute. The observed reduction in specific contact resistivity (ρ_C) at this temperature highlights the effectiveness of the annealing process in optimising electrical properties. Furthermore, 400°K is a commonly used benchmark in published studies, ensuring the results are directly comparable with state-of-the-art data and validating the suitability of these ohmic contacts for high-temperature operation.

7.1 400Å Ta and 2000Å Pure Al on AlN and Nucleation EPI

An abstract of ohmic specific contact resistance is shown as a function of increasing temperatures and annealing temperature using Ta and pure Al to GaN AlN and nucleation EPI in Table 7.1. The lowest specific contact resistance was for deposited

400Å Ta and 2000Å Pure Al at 3.35×10^{-3} Ωcm^2 at 400°K on the AlN EPI. The AlN EPI specific contact resistance is lower than the nucleation EPI and can be explained further as this substrate also shows a lower transfer length and contact resistance across the AlN wafer at all measured temperatures. The results of the specific contact resistance for GaN AlN (a) and GaN Nucleation (b) 400ÅTa / 2000Å Pure Al is also shown in Fig. 7.1 & Fig. 7.2, respectively. These results show the specific contact resistivity across the GaN devices at increasing temperatures.

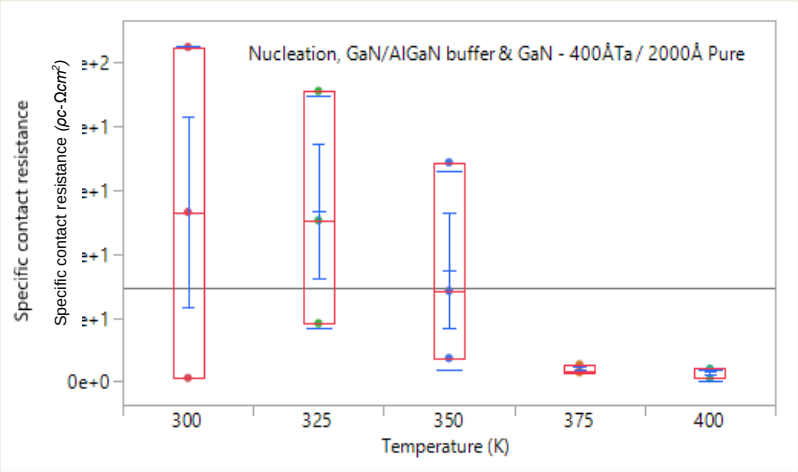

Fig. 7.1: The plot shows the specific contact resistance (ρc-Ωcm^2) at increasing measurement temperatures *(K)* across the center, mid-radius, and edge of the nucleation EPI with 400Å Ta and 2000Å Pure Al ohmic contacts

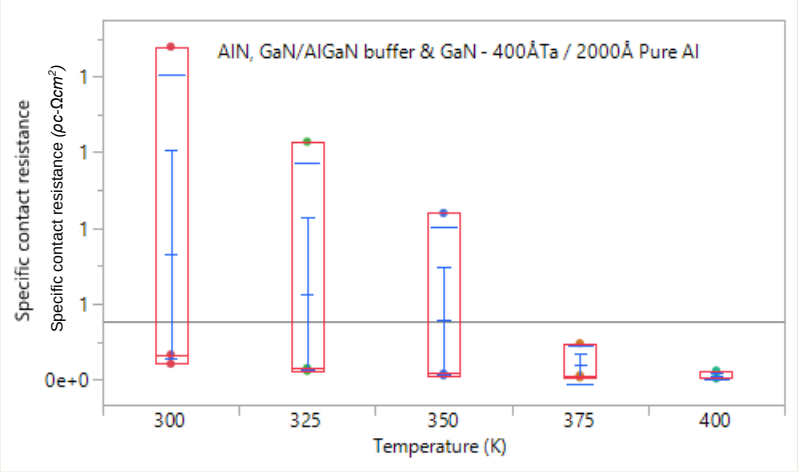

Fig. 7.2: The plot shows the specific contact resistance *(ρc-Ωcm^2)* at increasing measurement temperatures *(K)* across the center, mid-radius, and edge of the AlN EPI with 400Å Ta and 2000Å Pure Al ohmic contacts

Table 7.1: Specific contact resistance on AIN and Nucleation EPI with 400ÅTa / 2000Å Pure Al ohmic metal

EPI substrate and ohmic metal	Measurement Temperature (°K)	Specific contact resistance (Ωcm^2)		
		Center	Mid-radius	Edge
AlN, GaN/AlGaN buffer & GaN - 400ÅTa / 2000Å Pure Al	300	4.19E-02	8.79E-01	6.65E-02
	325	2.35E-02	6.28E-01	3.05E-02
	350	1.15E-02	4.40E-01	1.60E-02
	375	6.27E-03	9.60E-02	1.15E-02
	400	3.35E-03	2.40E-02	6.08E-03
Nucleation, GaN/AlGaN buffer & GaN - 400ÅTa / 2000Å Pure Al	300	1.16E+00	5.32E+01	1.05E+02
	325	1.83E+01	5.06E+01	9.12E+01
	350	2.85E+01	6.88E+01	7.37E+00
	375	5.40E+00	3.24E+00	2.90E+00
	400	9.75E-01	4.06E+00	1.10E+00

Across the wafer, differences in resistance values are observed, with the center displaying a higher resistance at room temperature (300°K) that gradually diminishes towards the mid-radius and edge. Interestingly, as the temperature rises, these variations become less evident, suggesting a more uniform behaviour at higher temperatures. A comparative analysis between AlN substrate and nucleation reveals higher resistance in nucleation at room temperature, but a more rapid decrease with temperature. An unexpected anomaly is noted at 350°K for Nucleation at the center, possibly attributed to experimental uncertainties. Furthermore, an average specific contact resistance is taken by averaging the center, mid-radius, and edge results, this is shown below in Fig. 7.3. While the differences between the AlN and nucleation data appear substantial, this comparison is critical to evaluating the impact of epitaxial layer quality on ohmic contact performance. It not only highlights the superior performance of AlN but also demonstrates the limitations of nucleation layers, providing guidance for material selection, process improvements, and cost-performance trade-offs in GaN device fabrication. These insights directly align with the broader objectives of the thesis, contributing to the advancement of high-performance ohmic contact designs for GaN-based technologies. The linear graph below shows the specific contact resistance of the Nucleation EPI layer as 9.75×10^{-1} Ωcm^2 at 400K, compared to 3.35×10^{-3} Ωcm^2 at 400°K for the AlN layer at the same temperature, plotting the graph

on a logarithmic scale highlights the magnitude of the difference more clearly. (Fig. 7.4).

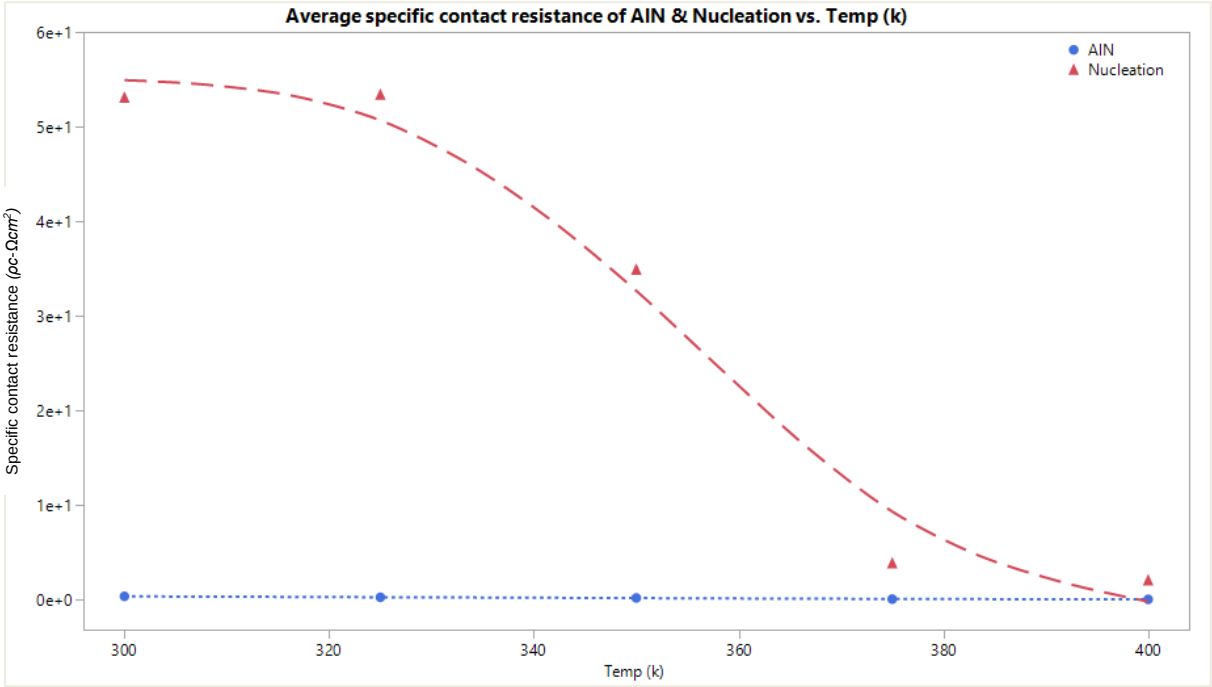

Fig. 7.3: Average specific contact resistance *(ρc-Ωcm²)* of AlN and Nucleation vs temperature *(K)*

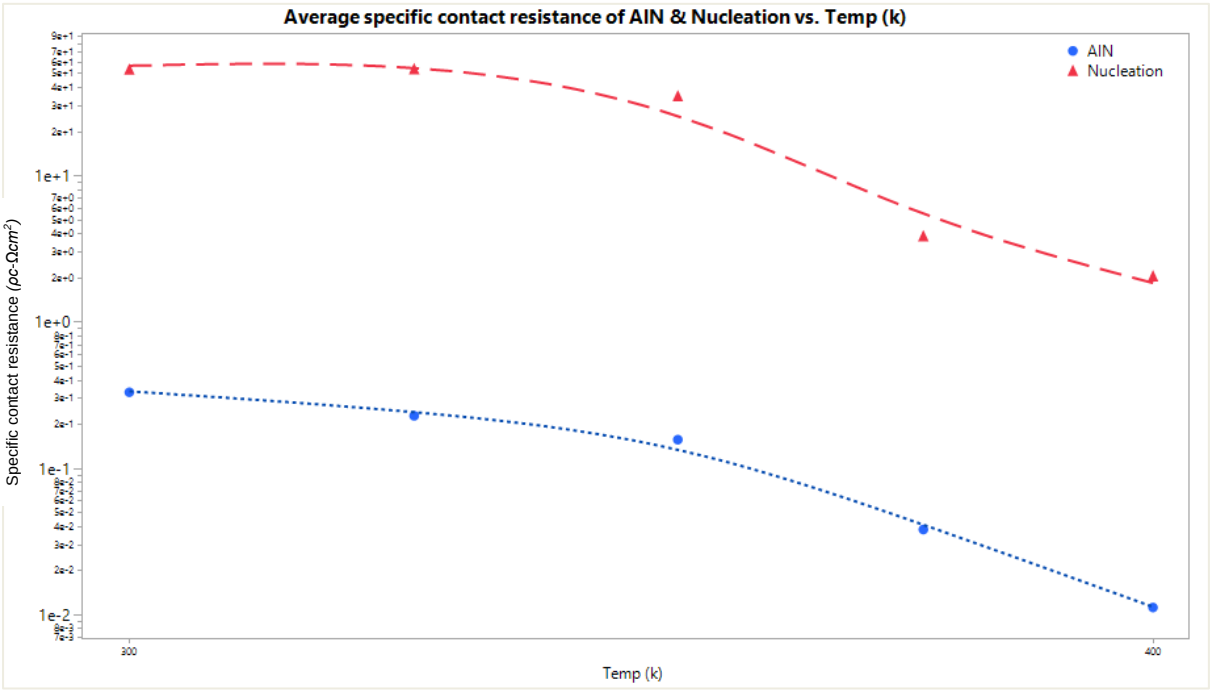

Fig. 7.4: Average specific contact resistance *(ρc-Ωcm²)* of AlN and Nucleation vs temperature *(K)* shown logarithmically

Transmission Electron Microscopy (TEM) was utilised alongside Energy Dispersive X-ray analysis (EDX) to determine the integrity of the contacts and to examine for any contamination within the contacts that may skew the electrical data. A protective layer of Platinum (Pt) was deposited using the FIB tool to shield the surface or area of interest during preparation and analysis.

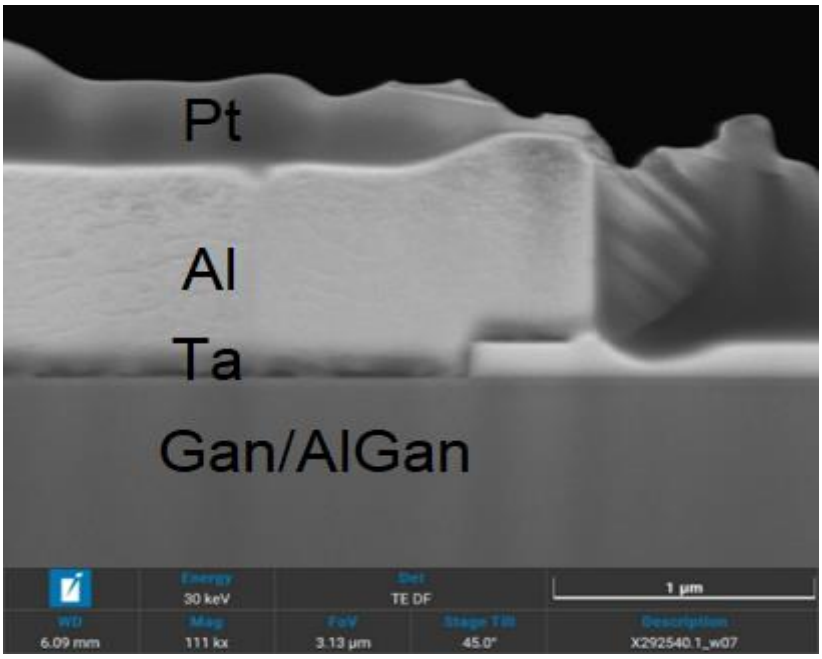

Fig. 7.5: TEM cross-section of the contact, Nucleation, GaN/AlGaN buffer & GaN - 400ÅTa / 2000Å Pure Al

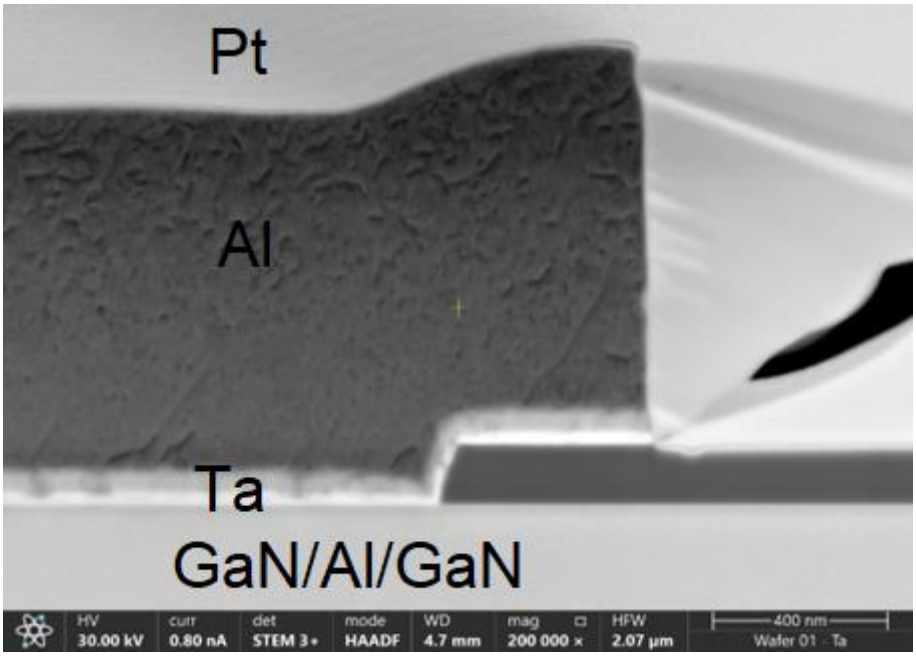

Fig. 7.6: TEM cross-section of the contact, AlN, GaN/AlGaN buffer & GaN - 400ÅTa / 2000Å Pure Al

From the TEM cross-sections (Fig. 7.5 and 7.6) we can see that there is some voiding (porosity) present on the Nucleation device between the metal-semiconductor interface. This voiding and or porosity could contribute to the higher resistance measurements recorded across this sample. The metal-semiconductor interface on the AlN device is annealed correctly which would provide better electrical characteristics, i.e. a lower resistance.

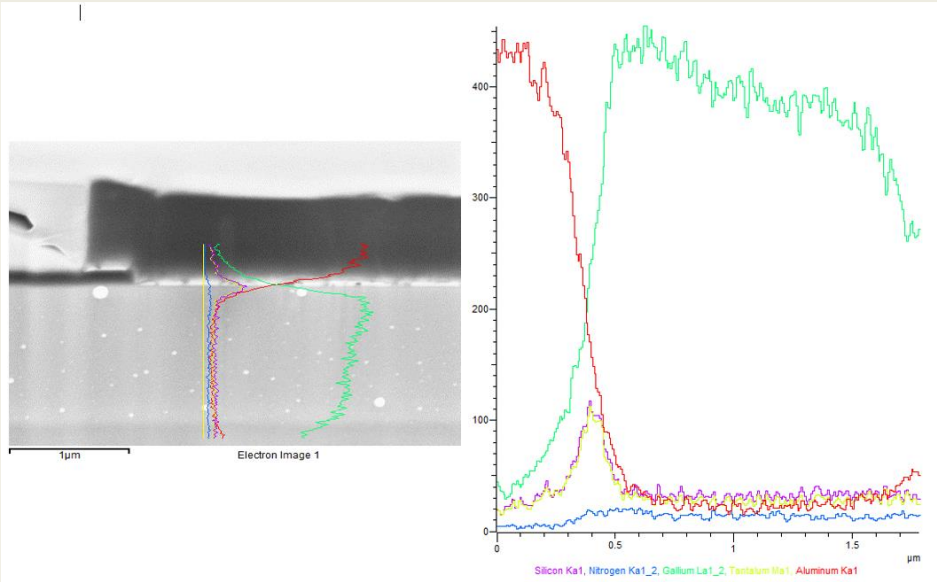

Fig. 7.7: EDX linescan of the contact, Nucleation, GaN/AlGaN buffer & GaN - 400ÅTa / 2000Å Pure Al

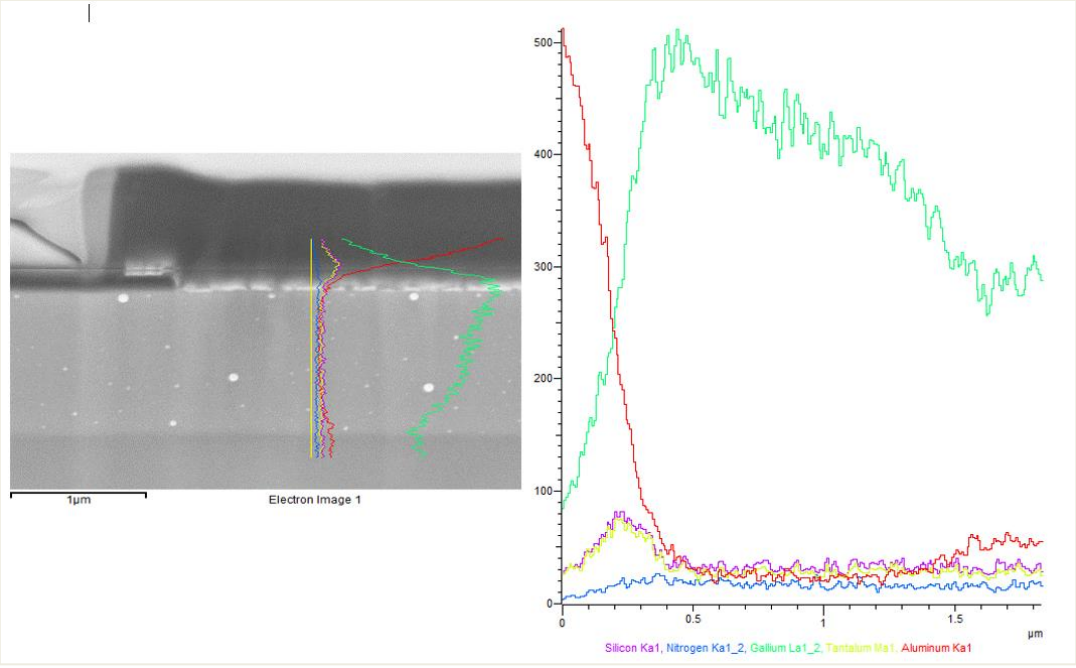

Fig. 7.8: EDX linescan of the contact, AlN, GaN/AlGaN buffer & GaN - 400ÅTa / 2000Å Pure Al

EDX line scan analyses as shown in Fig. 7.7 and 7.8 conducted across the metal-GaN interface, utilising elemental mapping provided conclusive evidence of an uncontaminated interface, reinforcing the reliability of the fabricated contacts for subsequent electrical measurements and analyses. For clarity, all the EDX line scans show compositions of silicon (purple line), nitrogen (blue line), gallium (green line), aluminium (red line) and titanium or tantalum (yellow line) retrospective of whether it is a titanium wafer being analysed or a tantalum wafer being analysed.

7.2 250Å Ti and 3000Å AlCu on AlN and Nucleation EPI

Ohmic specific contact resistance is shown as a function of increasing temperatures and annealing temperature using Ti and AlCu to GaN AlN and nucleation EPI is shown in Table 7.2. The lowest specific contact resistance was for deposited 250Å Ti and 3000Å AlCu at 2.43×10^{-3} Ωcm^2 at 400°K on the Nucleation EPI. The Nucleation and AlN EPI specific contact resistance for deposited 250Å Ti and 3000Å AlCu are very similar with the AlN EPI having a specific contact resistance of 6.67×10^{-3} Ωcm^2 at 400°K. The results of the specific contact resistance for GaN AlN (a) and GaN Nucleation (b) 250ÅTa / 3000Å AlCu is also shown in Fig. 7.9 & 7.10, respectively. These results show the specific contact resistivity across the GaN devices at increasing temperatures.

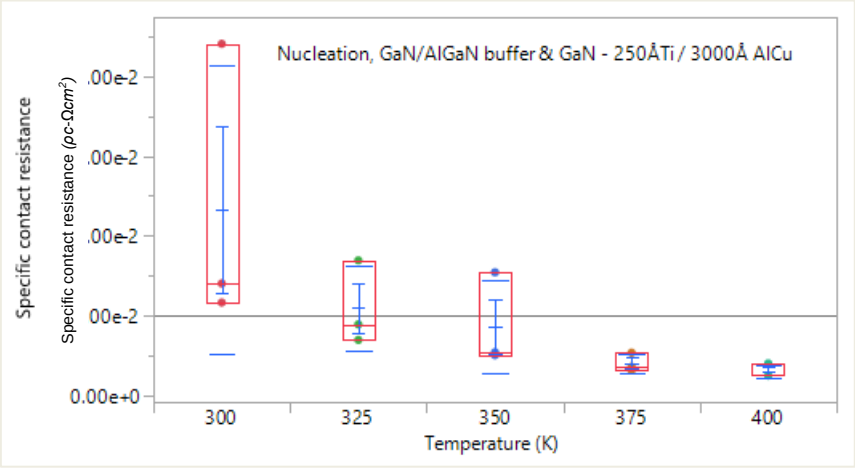

Fig. 7.9: The plot shows the specific contact resistance *(ρc-Ωcm²)* at increasing measurement temperatures *(K)* across the center, mid-radius, and edge of the nucleation EPI with 250Å Ti and 3000Å AlCu ohmic contacts

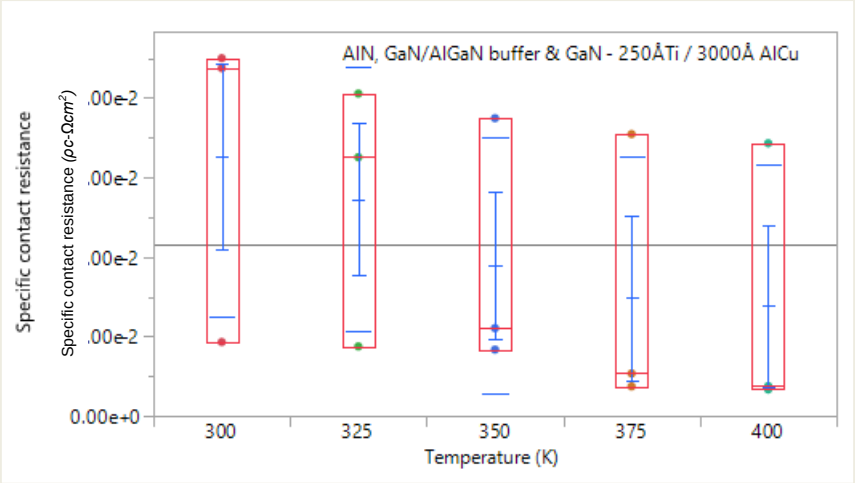

Fig. 7.10: The plot shows the specific contact resistance *(ρc-Ωcm²)* at increasing measurement temperatures *(K)* across the center, mid-radius, and edge of the AlN EPI with 250Å Ti and 3000Å AlCu ohmic contacts.

Table 7.2: Specific contact resistance on AlN and Nucleation EPI with 250ÅTi / 3000Å AlCu ohmic metal

EPI substrate and ohmic metal	Measurement Temperature (°K)	Specific contact resistance (Ωcm²)		
		Center	Mid-radius	Edge
AlN, GaN/AlGaN buffer & GaN - 250ÅTi / 3000Å AlCu	300	8.75E-02	1.86E-02	9.00E-02
	325	6.51E-02	1.75E-02	8.11E-02
	350	2.21E-02	1.67E-02	7.49E-02
	375	1.07E-02	7.45E-03	7.09E-02
	400	7.53E-03	6.67E-03	6.86E-02
Nucleation, GaN/AlGaN buffer & GaN - 250ÅTi / 3000Å AlCu	300	1.40E-02	1.16E-02	4.41E-02
	325	8.86E-03	6.91E-03	1.69E-02
	350	5.00E-03	5.35E-03	1.54E-02
	375	3.09E-03	3.53E-03	5.30E-03
	400	2.49E-03	2.43E-03	3.96E-03

Across the wafer locations, differences in resistance values are observed, with the center showing lower resistance at 300°K compared to mid-radius and edge. As the temperature increases, these disparities diminish. Notably, in this dataset, Nucleation exhibits lower specific contact resistance than the EPI substrate at 300°K, contrasting with the previous dataset (400ÅTa / 2000Å Pure Al). The rate of resistance decrease with temperature is more prominent for EPI substrate compared to Nucleation, emphasising the influence of fabrication parameters. The observed trends in this dataset highlight the complexity of optimising GaN HEMT devices, calling for careful consideration of fabrication parameters and temperature conditions for improved

device performance. The average specific contact resistance is taken by averaging the center, mid-radius, and edge results, this is shown below in Fig. 7.11. The linear graph shows that the Nucleation EPI specific contact resistance of 2.96×10^{-2} Ωcm^2 at 400°K is a similar value to the AlN specific contact resistance of 2.76×10^{-3} Ωcm^2 at 400°K. The data shows a factor difference of 1.072×10^{1} (or 10.72) between the two substrates at 400°K.

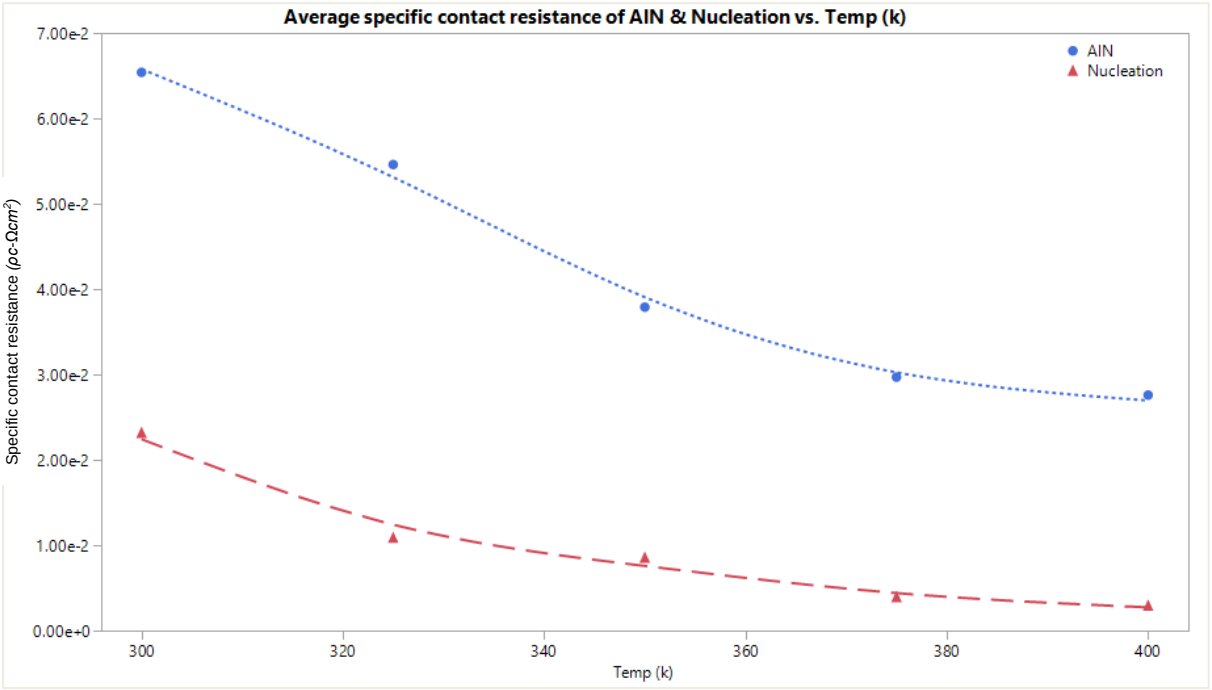

Fig. 7.11: Average specific contact resistance *(ρc-Ωcm²)* of AlN and Nucleation vs temperature *(K)*

Transmission Electron Microscopy (TEM) and Energy Dispersive X-ray analysis (EDX) were employed to assess the integrity of the contacts and investigate potential contamination that could affect the accuracy of the electrical data.

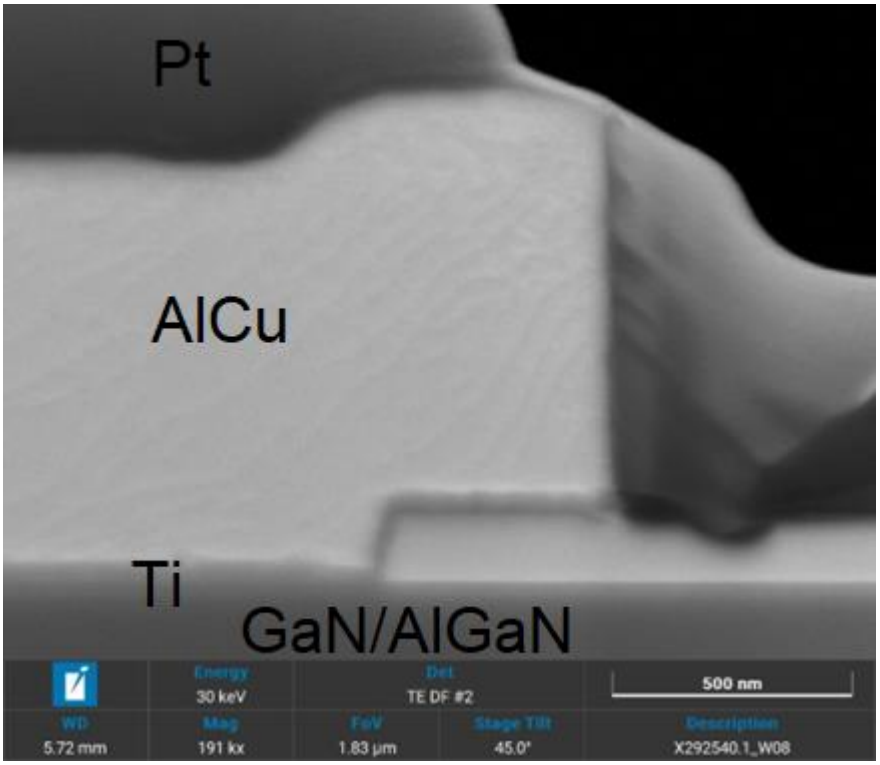

Fig. 7.12: TEM cross-section of the contact, Nucleation, GaN/AlGaN buffer & GaN - 250ÅTi / 3000Å AlCu

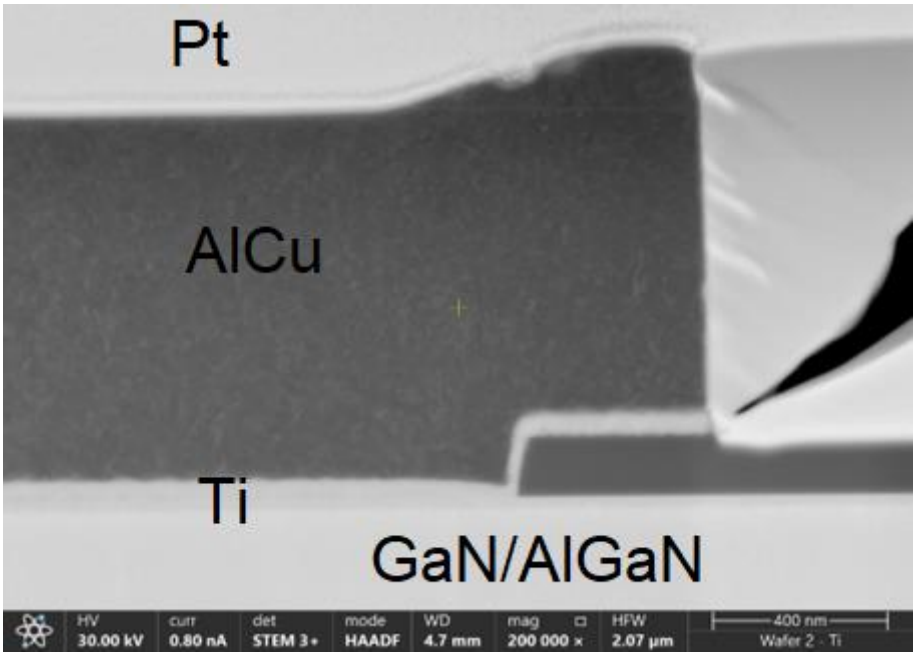

Fig. 7.13: TEM cross-section of the contact, AlN, GaN/AlGaN buffer & GaN - 250ÅTi / 3000Å AlCu

The TEM images in Figures 7.12 & 7.13 show no voiding or defectivity that would hinder or skew the electrical data. The metal to GaN interface looks consistent with the metal to GaN interface from the AlN, 400ÅTa / 2000Å Pure Al sample from the previous data set which also exhibited good specific contact resistance values.

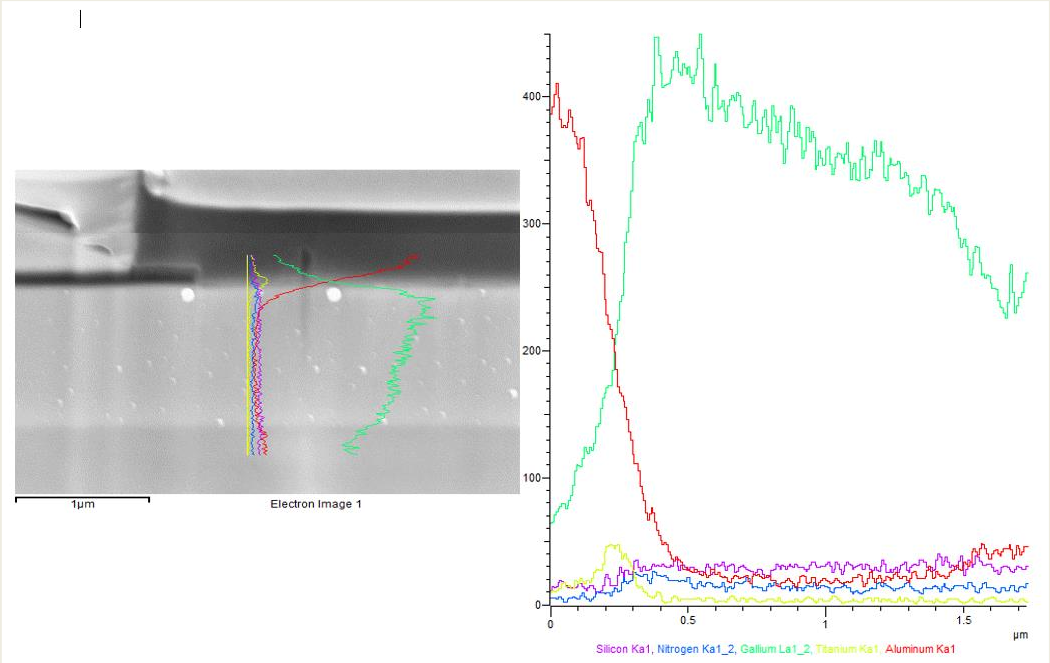

Fig. 7.14: EDX linescan of the contact, Nucleation, GaN/AlGaN buffer & GaN - 250ÅTi / 3000Å AlCu

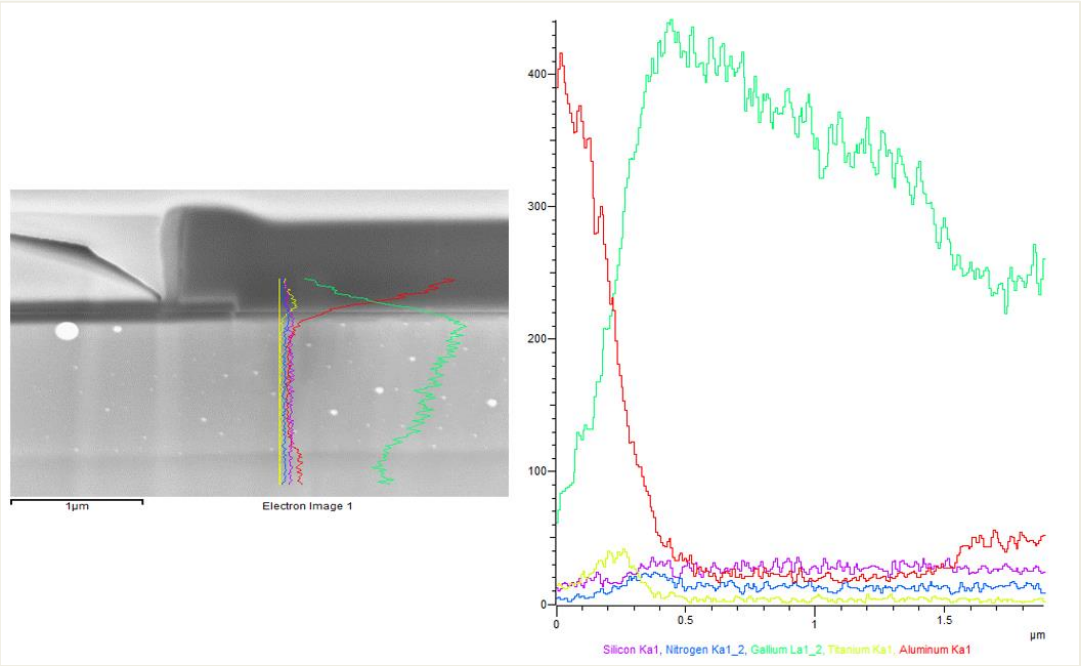

Fig. 7.15: EDX linescan of the contact, AlN, GaN/AlGaN buffer & GaN - 250ÅTi / 3000Å AlCu

Conclusive evidence of an uncontaminated interface was established through EDX line scan analyses, as depicted in Figures 7.14 and 7.15. These analyses were performed across the metal-GaN interface, employing elemental mapping. This finding strengthens the reliability of the fabricated contacts for subsequent electrical measurements and analyses.

7.3 250Å Ti and 3000Å Pure Al on AlN and Nucleation EPI

Ohmic specific contact resistance as a function of increasing temperatures using Ti and Pure Al to GaN AlN and nucleation EPI is shown in Table 7.3. The lowest specific contact resistance was for deposited 250Å Ti and 3000Å Pure Al was 1.86×10^{-3} Ωcm^2 at 400°K on the AlN EPI. The Nucleation and AlN EPI specific contact resistance for deposited 250Å Ti and 3000Å Pure Al are very similar with the Nucleation EPI having a specific contact resistance of 2.2×10^{-3} Ωcm^2 at 400°K. The results of the specific contact resistance for GaN AlN and GaN Nucleation 250ÅTa / 3000Å Pure Al is also shown in Fig. 7.16 & 7.17, respectively. These results show the specific contact resistivity across the GaN devices at increasing temperatures.

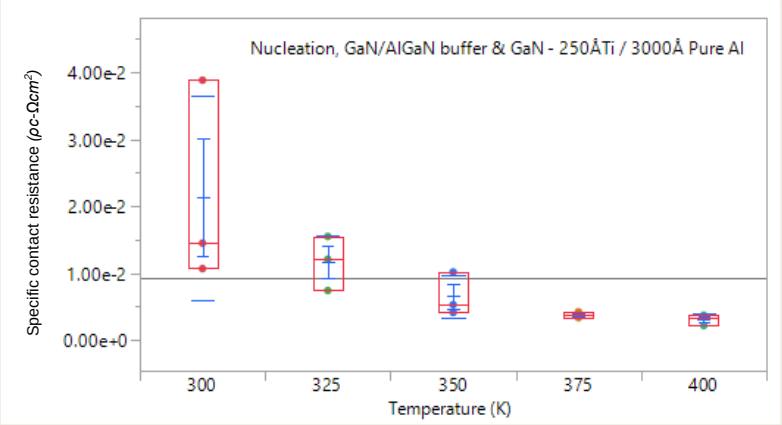

Fig. 7.16: The plot shows the specific contact resistance *(ρc-Ωcm²)* at increasing measurement temperatures *(K)* across the center, mid-radius, and edge of the nucleation EPI with 250Å Ti and 3000Å Pure Al ohmic contacts

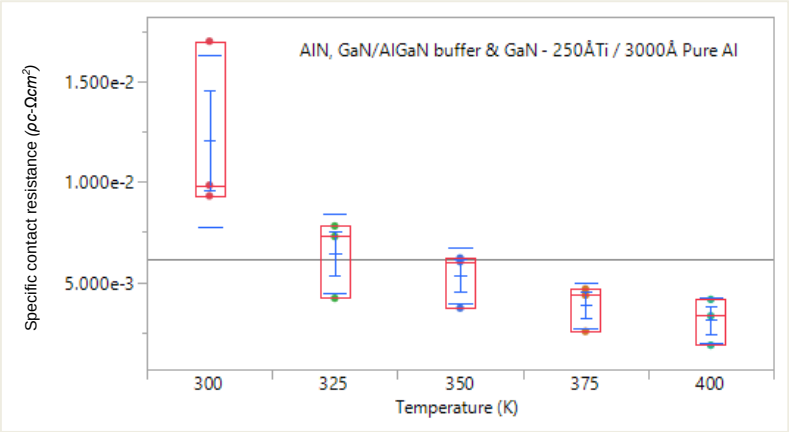

Fig. 7.17: The plot shows the specific contact resistance *(ρc-Ωcm²)* at increasing measurement temperatures *(K)* across the center, mid-radius, and edge of the AlN EPI with 250Å Ti and 3000Å Pure Al ohmic contacts.

Table 7.3: Specific contact resistance on AIN and Nucleation EPI with 250ÅTi / 3000Å Pure Al ohmic metal

EPI substrate and ohmic metal	Measurement Temperature (°K)	Specific contact resistance (Ωcm^2)		
		Center	Mid-radius	Edge
Nucleation, GaN/AlGaN buffer & GaN - 250ÅTi / 3000Å Pure Al	300	3.88E-02	1.45E-02	1.07E-02
	325	1.55E-02	1.21E-02	7.43E-03
	350	1.02E-02	4.15E-03	5.32E-03
	375	4.26E-03	3.37E-03	3.74E-03
	400	3.76E-03	2.20E-03	3.46E-03
AlN, GaN/AlGaN buffer & GaN - 250ÅTi / 3000Å Pure Al	300	1.70E-02	9.83E-03	9.30E-03
	325	7.28E-03	4.20E-03	7.80E-03
	350	6.02E-03	3.71E-03	6.20E-03
	375	4.35E-03	2.55E-03	4.66E-03
	400	3.32E-03	1.86E-03	4.14E-03

Interestingly, at 300°K, the center of the wafer shows higher resistance compared to the mid-radius and edge, a pattern that diminishes with increasing temperature. Notably, the comparison between Nucleation and EPI substrate reveals a shift in behaviour, with Nucleation consistently displaying higher resistance across all temperatures and wafer locations. The specific contact resistance average is taken by averaging the center, mid-radius, and edge results, this is shown below in Fig. 7.18. The linear graph shows that the Nucleation EPI specific contact resistance of 3.14×10^{-3} Ωcm^2 at 400°K is a similar value to the AlN specific contact resistance of 3.11×10^{-3} Ωcm^2 at 400°K.

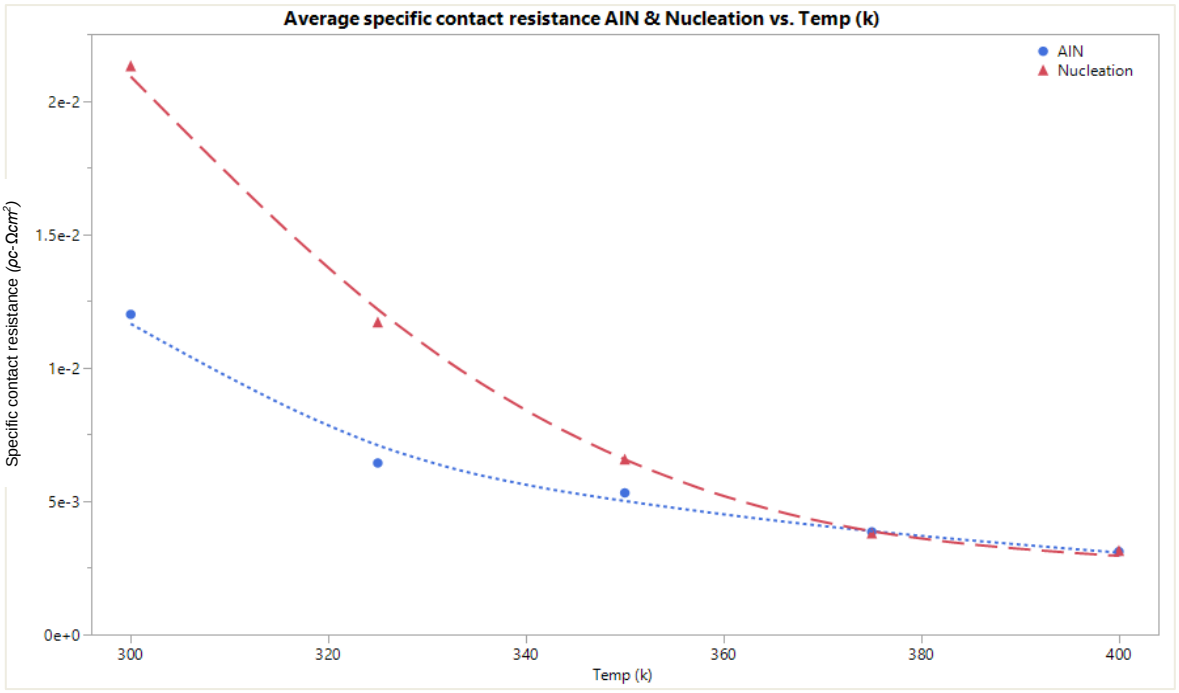

Fig. 7.18: Average specific contact resistance *(ρc-Ωcm²)* of AlN and Nucleation vs temperature *(K)*

Transmission Electron Microscopy (TEM) and Energy Dispersive X-ray analysis (EDX) were employed to assess the integrity of the contacts on the 250Å Ti and 3000Å Pure Al ohmic metals and investigate potential contamination that could affect the accuracy of the electrical data.

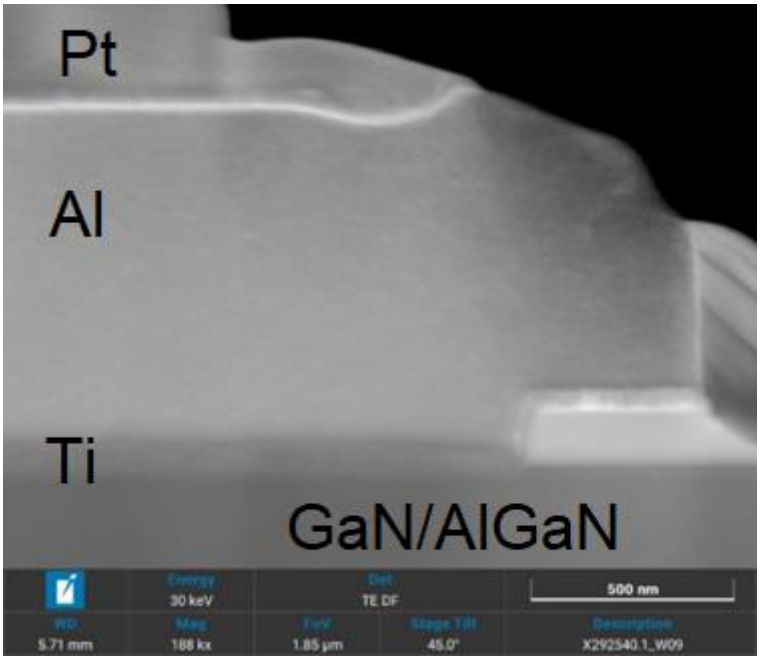

Fig. 7.19: TEM cross-section of the contact, Nucleation, GaN/AlGaN buffer & GaN - 250ÅTi / 3000Å Pure Al

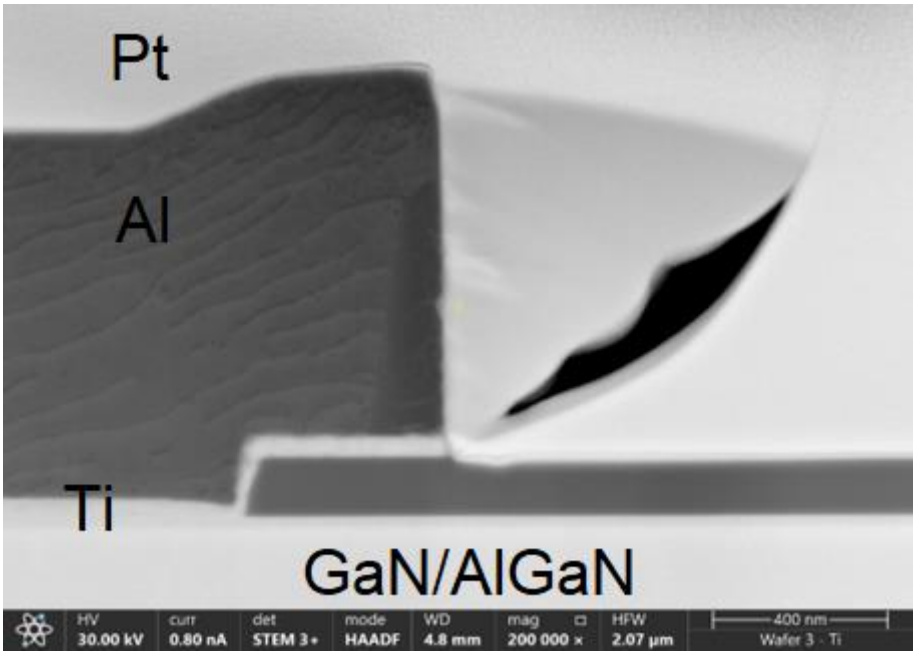

Fig. 7.20: TEM cross-section of the contact, AlN, GaN/AlGaN buffer & GaN - 250ÅTi / 3000Å Pure Al

The TEM images in Figures 7.19 & 7.20 show no voiding or defectivity that would hinder or skew the electrical data. The metal to GaN interface looks consistent with the metal to GaN interface from the AlN, 400ÅTa / 2000Å Pure Al sample from the first data set which also exhibited good specific contact resistance values.

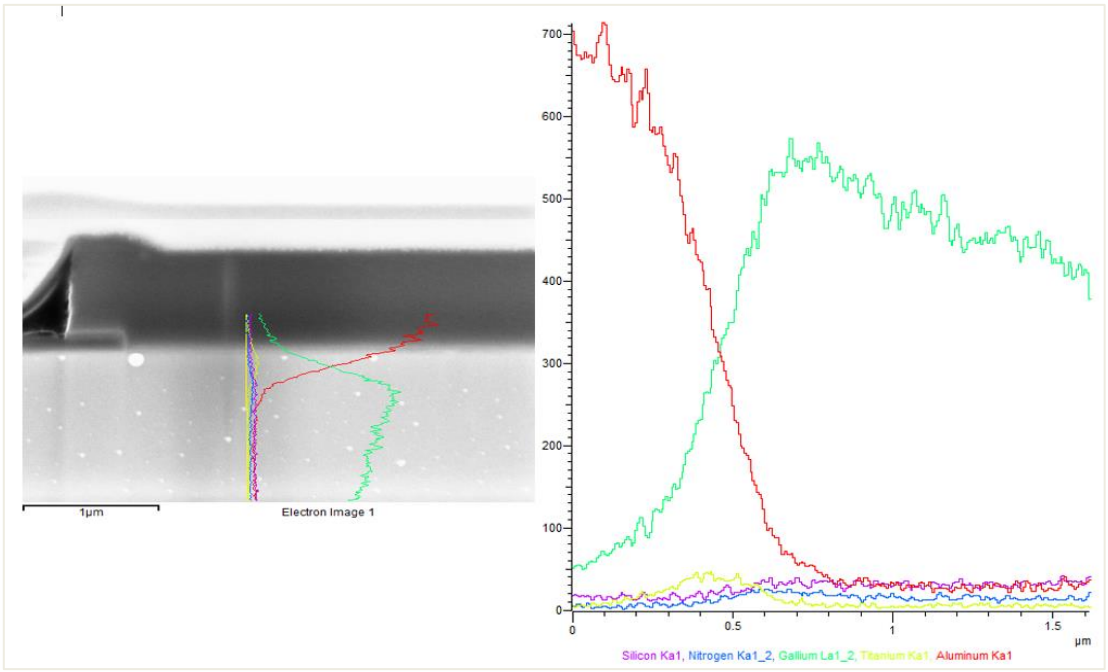

Fig. 7.21: EDX linescan of the contact, Nucleation, GaN/AlGaN buffer & GaN - 250ÅTi / 3000Å Pure Al

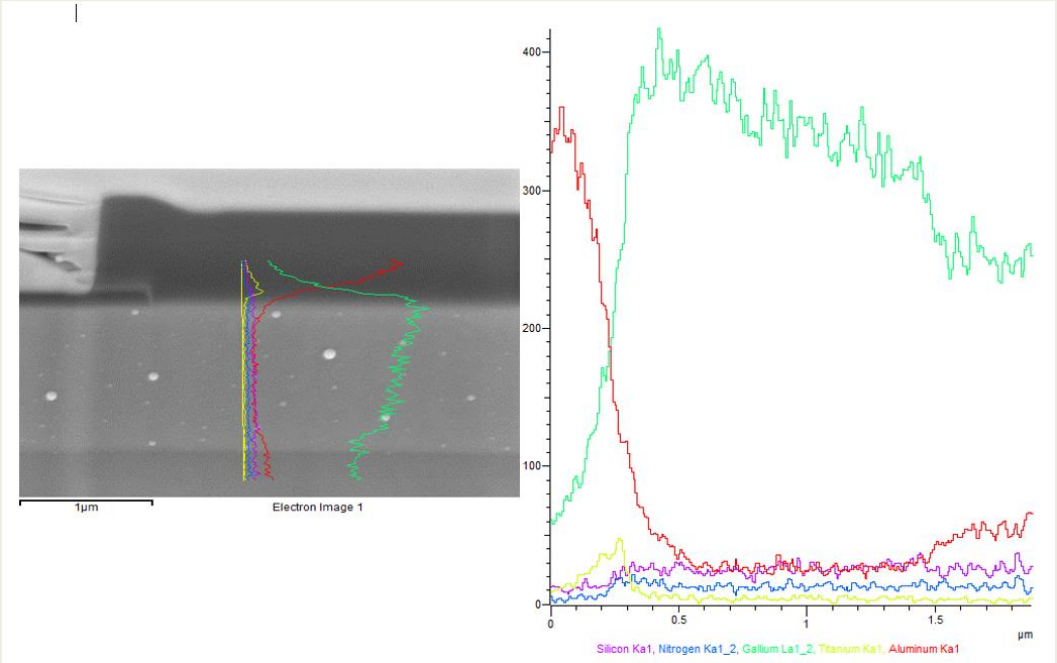

Fig. 7.22: EDX linescan of the contact, AlN, GaN/AlGaN buffer & GaN - 250ÅTi / 3000Å Pure Al

A pristine interface was confirmed through EDX line scan analyses, illustrated in Figures 7.21 and 7.22. This analyses through the metal, GaN interface enhances the trustworthiness of the electrical data.

7.4 Interpretation of electrical data and current transport mechanisms

Ohmic contacts were fabricated onto the two different GaN substrates, with the layer compositions detailed in Tables 5.1 and 5.2. The metallisation and subsequent post-annealing treatments are presented in Table 6.1. All contacts underwent annealing at a maximum temperature of 600 °C to assess their structural integrity. The TEM images provide a visual confirmation of the contact's structural integrity post a 600°C annealing process, highlighting the robustness of the fabrication methodology. Specific contact resistivity (ρ_C) was measured at the centre, mid-radius, and the edge of the wafers at various temperatures for contacts made from pure Al, AlCu, Ti, and Ta, with a focus on the temperature profile of 400°K. The specific contact resistivity values measured at 400°K exhibited various results:

- Nucleation, 400ÅTa / 2000Å Pure Al contact: 2.04×10^{0} Ωcm^2
- Nucleation, 250ÅTi / 3000Å AlCu contact: 2.96×10^{-3} Ωcm^2
- Nucleation, 250ÅTi / 3000Å Pure Al contact: 3.14×10^{-3} Ωcm^2
- AlN, 400ÅTa / 2000Å Pure Al contact: 1.11×10^{-2} Ωcm^2

- AlN, 250ÅTi / 3000Å AlCu contact: 1.13×10^{-1} Ωcm^2
- AlN, 250ÅTi / 3000Å Pure Al contact: 3.10×10^{-3} Ωcm^2

These resistivity values are notable, demonstrating an approximate order of magnitude reduction compared to contacts measured at room temperature. This alignment with the classic thermionic emission (TFE) theory underscores the effectiveness of the annealing process in optimising the electrical properties of the contacts. In-depth analysis of the current transport mechanism for the three lowest specific contact resistance wafers show AlN, 250ÅTi / 3000Å Pure Al contact: 3.10×10^{-3} Ωcm^2 to have a doping density (N_D) of 8.7×10^{19} cm^{-3} with a barrier height (Φ_B) of 1.477eV. Figure 7.23 below shows the specific contact resistance as a function of temperature for the AlN, 250ÅTi / 3000Å Pure Al contact annealed at 600°C. Red circles are the measured values and the blue stars are the best fit with the Thermionic Field Emission (TFE) model. The barrier height value was extracted from the best fit.

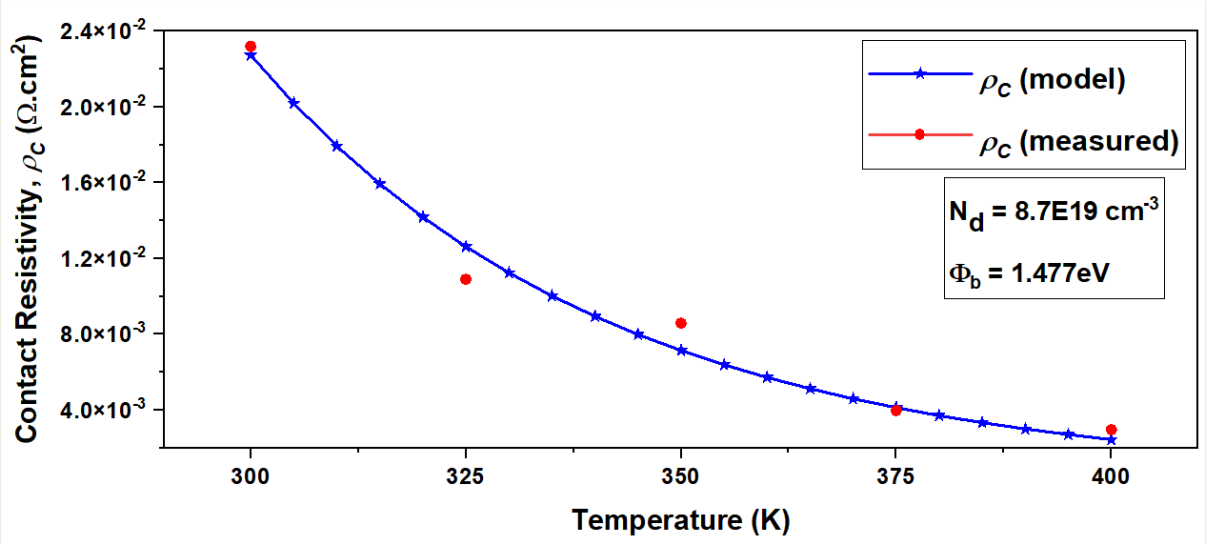

Fig. 7.23: Specific contact resistance *(ρc-Ωcm^2)* v temperature (*K*) showing TFE model and extracted barrier height for AlN, 250ÅTi / 3000Å Pure Al contact

The next wafer, nucleation, with a 250ÅTi / 3000Å AlCu contact reveals a specific contact resistivity of 2.96×10^{-3} Ωcm^2 and exhibits a doping density (N_D) of 7.7×10^{18} cm^{-3} with a barrier height (Φ_B) of 0.66eV. In Figure 7.24, the specific contact resistance is presented as a function of temperature for the nucleation, 250ÅTi / 3000Å AlCu contact after annealing at 600°C. The data points, represented by red circles, depict the measured values, while the blue stars correspond to the best fit achieved through the application of the Thermionic Field Emission (TFE) model. Notably, the barrier height value of 0.66eV was derived from the optimal fit obtained using the TFE model.

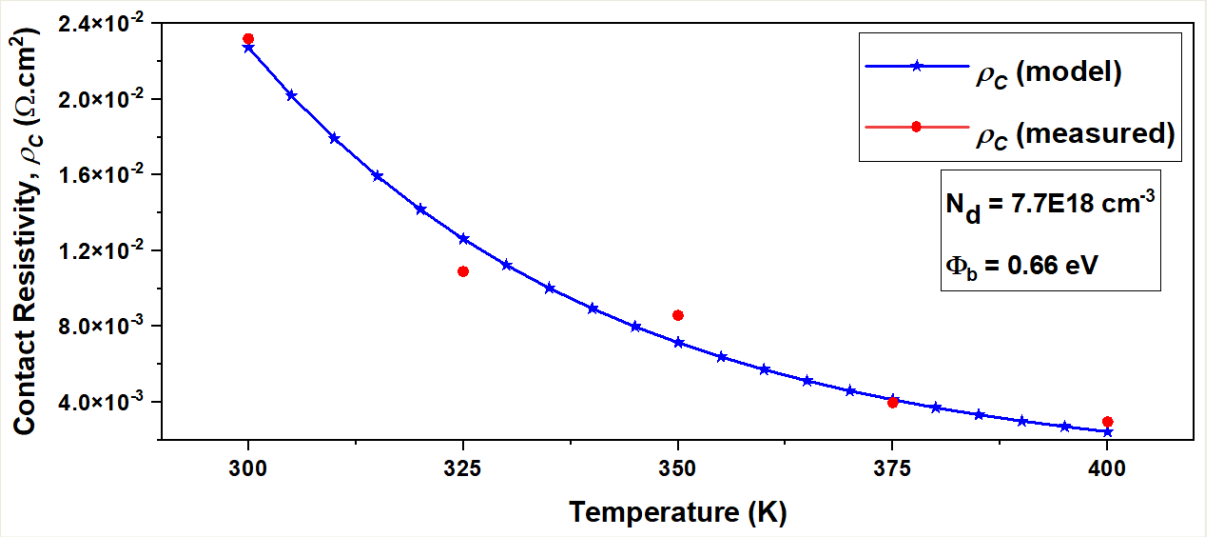

Fig. 7.24: Specific contact resistance *(ρc-Ωcm²)* v temperature (*K*) showing TFE model and extracted barrier height for nucleation, 250ÅTi / 3000Å AlCu contact

The most recent wafer, labelled as "nucleation" and featuring a 250Å Ti / 3000Å Pure Al contact, exhibits a specific contact resistivity of 3.14×10^{-3} Ωcm^2. This wafer also showcases a doping density (N_D) of 7.8×10^{18} cm^{-3}, along with a barrier height (Φ_B) of 0.66eV. In Figure 7.25, the specific contact resistance is illustrated as a function of temperature for the nucleation wafer with the 250Å Ti / 3000Å Pure Al contact, post-annealing at 600°C. The measured values are denoted by red circles, while the blue stars represent the best fit achieved using the Thermionic Field Emission (TFE) model. Notably, the barrier height value of 0.66 eV was deduced from the optimal fit obtained through the application of the TFE model.

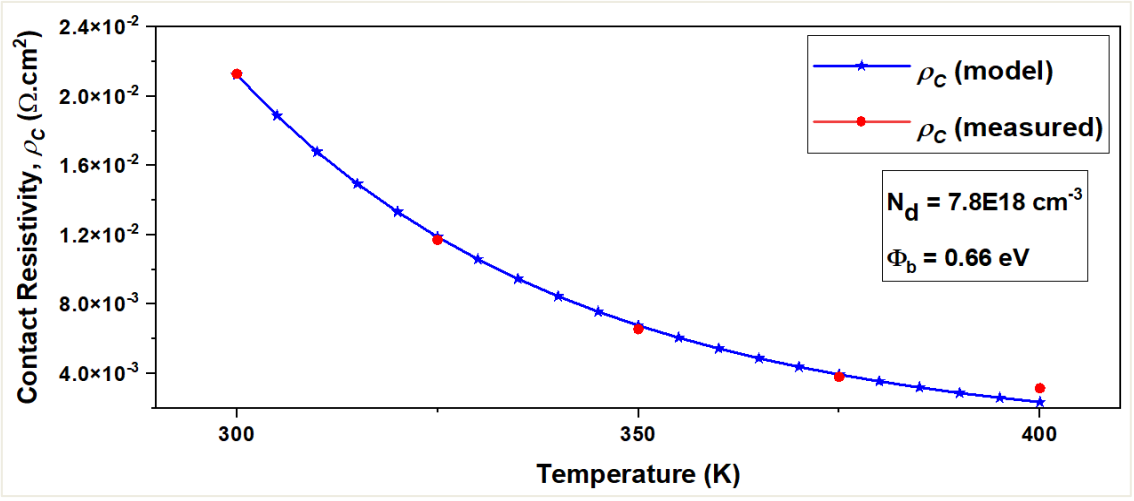

Fig. 7.25: Specific contact resistance *(ρc-Ωcm²)* v temperature (*K*) showing TFE model and extracted barrier height for nucleation, 250ÅTi / 3000Å Pure Al contact

TFE modeling of the three lowest valued specific contact resistance wafers shows an average doping density (N_D) of 3.42×10^{19} cm^{-3}. Insight into the doping density provides valuable information on the concentration of charge carriers within the semiconductor material, thus influencing the overall conductivity. Similarly, the barrier height determination is crucial in understanding the energy barrier that carriers must overcome during transport, impacting the efficiency of charge injection and extraction processes. All three Thermionic Field Emission fits showed an R^2 confidence value that exceeded 0.96.

To accompany the electrical data, top-down SEM images provided a visual conformation of zero defectivity. Complementing this technique, Transmission Electron Microscopy (TEM) was employed, providing high-resolution imagery for a thorough examination of the contact's internal structure. TEM was used to detect any anomalies or contamination that could potentially influence the electrical characteristics. The SEM and TEM images, collectively affirmed the absence of defectivity, highlighting the structural robustness of the ohmic contacts. Furthermore, EDX line scan analyses conducted across the metal-GaN interface, utilising elemental mapping provided conclusive evidence of an uncontaminated interface, reinforcing the reliability of the fabricated contacts for subsequent electrical measurements and analyses.

7.5 Comparison of results vs. published data and state-of-the-art review

The results in this study demonstrate specific contact resistivity (ρ_C) values ranging from 2.96×10^{-3} Ωcm^2 to 3.14×10^{-3} Ωcm^2 which are competitive and comparable to those reported in recent literature for GaN-based ohmic contacts.

7.5.1 Comparison of results vs. published data

Comparable studies show that Ti/Al-based contacts annealed at 600–850°C typically achieve ρ_C in the range of 10^{-4} to 10^{-6} Ωcm^2 [15] and Ta- and Ti-based contacts fabricated through high-temperature annealing have shown specific contact resistances on the order of 10^{-3} Ωcm^2 [16]. The measured values align with the thermionic field emission (TFE) transport model, further confirming the validity of the fabrication and testing methodology. The observed doping densities (N_D) of 7.7×10^{18} cm^{-3} to 8.7×10^{19} cm^{-3} fall within the reported values in literature, consistent with highly doped GaN structures used in ohmic contacts [18]. The extracted barrier heights

ranging from 0.66 eV to 1.477 eV are consistent with reported values for Ti/Al-based contacts on n-GaN substrates, further validating the TFE model's applicability. Similar works have demonstrated barrier heights from 0.6 eV to 1.5 eV, depending on annealing conditions and metallization stacks [19].

7.5.2 Comparison of results vs. state-of-the-art review (Chapter 3.1)

In Chapter 3.1, the state-of-the-art review emphasised several trends for ohmic contact development. Ti/Al-based contacts were widely adopted due to their low contact resistivity and thermal stability post-annealing. This study's Ti/AlCu and Ti/Al stacks exhibit similar performance, supporting the review's claim regarding their suitability for GaN devices. The review also highlighted the shift toward gold-free metallisation to reduce costs and improve CMOS compatibility. The use of pure Al and AlCu stacks in this study aligns with this trend, reinforcing the push for cost-effective, thermally stable alternatives. Material choices and processing techniques were another focus, identifying Ti and Ta based stacks as promising due to their strong adhesion, high-temperature stability, and ability to form low-barrier interfaces. The results obtained in this study confirm this, with Ta/Al contacts showing resistivities competitive with published values, particularly for nucleation layers. Finally, Chapter 3.1 discussed Thermionic Field Emission (TFE) as a dominant mechanism for heavily doped semiconductors with intermediate barrier heights. The data in this study aligns well with the TFE model, as evidenced by the high R^2 confidence values (>0.96) for all three fitted datasets, supporting the theoretical framework reviewed earlier.

7.6 Review of the results vs. published data and state-of-the-art review

The data presented in this chapter supports the conclusions drawn in the state-of-the-art review (Chapter 3.1), highlighting the effectiveness of Ti/Al- and Ta/Al-based ohmic contacts. The results are consistent with published values, validating the suitability of the annealing process and the metallisation stacks used. Furthermore, the use of the TFE model to interpret current transport mechanisms confirms its applicability to highly doped GaN layers, contributing to the ongoing development of low-resistance ohmic contacts for GaN-based devices.

Chapter 8: Conclusion

The pursuit of efficient, reliable, and high-performance ohmic contacts in Gallium Nitride (GaN) based High Electron Mobility Transistors (HEMTs) stands at the forefront of semiconductor research. This research thesis has undertaken a comprehensive exploration of various material variations, including pure aluminium (Pure Al), aluminium copper (AlCu), tantalum (Ta), and titanium (Ti), evaluating their specific contact resistivity (ρ_C) and shedding light on current transport mechanisms. The obtained results, coupled with advanced characterisation techniques, offer a critical understanding of the ohmic contact performance and lay the foundation for further research in GaN based HEMT devices.

The specific contact resistivity measurements conducted at 400°K unveil promising outcomes, showcasing an order of magnitude reduction compared to room temperature measurements. This reduction aligns with the classic thermionic field emission (TFE) theory, indicating a favourable enhancement in the electrical properties of the ohmic contacts at elevated temperatures. The temperature dependent behaviour observed in the specific contact resistivity values also provides valuable insights into the thermionic emission processes governing the charge transport across the contacts. The barrier height plays a crucial role in determining the type of contact (Schottky or ohmic) and thus affects the overall efficiency of the charge transport across the metal semiconductor interface.

When compared to state-of-the-art and typical commercial devices, the results presented in this thesis demonstrate competitive performance. For example, state-of-the-art ohmic contacts in GaN devices typically achieve specific contact resistivities in the range of 10^{-6} to 10^{-4} Ωcm^2. The values obtained in this study, such as 2.96×10^{-3} Ωcm^2 and 4.14×10^{-3} Ωcm^2, while higher than the ideal target of 10^{-6} Ωcm^2, are still within the range of commercially viable devices, particularly for applications where cost and thermal stability outweigh absolute resistivity performance.

An integral aspect of this research lies in the structural integrity assessment of the ohmic contacts post a 600°C annealing process, crucial for ensuring the robustness of the fabrication methodology. The confirmation through scanning electron microscopy (SEM) images and transmission electron microscopy (TEM) images attests to the resilience of the contacts, highlighting the reliability and stability of the

fabricated ohmic contacts under elevated annealing temperatures. This structural confirmation is pivotal for the practical implementation of these contacts in real-world applications, where they may encounter varying environmental conditions. The following table summarizes the key findings from this research:

Table 8.1 – Summary of results

Contact type	Substrate	Specific Contact Resistivity (Ωcm²)	Doping Density (ND) (cm^{-3})	Barrier Height (ΦB) (eV)
400Å Ta / 2000Å Pure Al	AlN	3.35×10^{-3}	8.7×10^{19}	1.477
250Å Ti / 3000Å AlCu	Nucleation	2.96×10^{-3}	7.7×10^{18}	0.66
250Å Ti / 3000Å Pure Al	Nucleation	3.14×10^{-3}	7.8×10^{18}	0.66

The specific configurations explored, such as the nucleation with a 250Å Ti / 3000Å AlCu contact and nucleation with a 250Å Ti / 3000Å Pure Al contact, provide a deeper understanding of the material-specific performance. The former reveals a specific contact resistivity of 2.96×10^{-3} Ωcm², a doping density of 7.7×10^{18} cm^{-3}, and a barrier height (ΦB) of 0.66 eV. Meanwhile, the latter exhibits a specific contact resistivity of 3.14×10^{-3} Ωcm², a doping density of 7.8×10^{18} cm^{-3}, and a barrier height of 0.66 eV. These findings are extremely positive as the data shows ohmic contacts, emphasising the significance of material dependent characteristics in achieving desired electrical performance.

Regarding the potential influence of gate voltage on the results, it is acknowledged that this parameter was not explicitly investigated in this thesis. The focus of this research was to evaluate intrinsic material properties and their impact on ohmic contact performance, particularly under elevated temperatures. Future studies could incorporate gate voltage effects to explore how modulation of the electric field influences charge transport mechanisms and contact resistivity, providing a more comprehensive understanding of device behaviour under operational conditions.

The electrical data allows us to examine ways of reducing the RDSon on GaN HEMT devices which will contribute to its uses at higher frequencies. For these 100V GaN HEMT devices, an ideal specific contact resistance would be around 1×10^{-6} Ωcm². With the values from this research, it would account for around half of the RDSon of the device as shown in the plot below modelled from MATLAB.

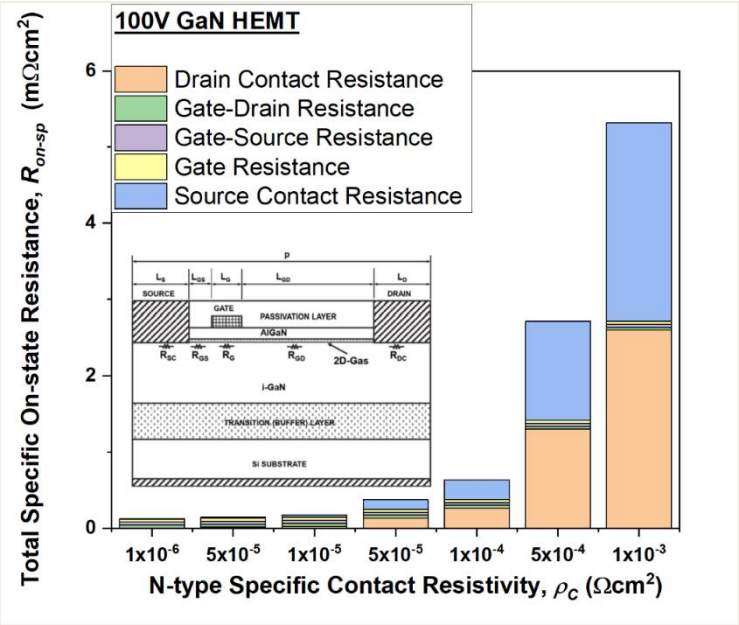

Fig. 8.1: Plot of specific contact resistivity v total specific on-state resistance

While this research advances our understanding of GaN based HEMT ohmic contacts, there are opportunities for further exploration. Future work should delve into additional material variations, considering diverse combinations and compositions to identify optimal configurations for specific applications. Examining temperature dependencies in greater detail will also enhance our grasp of the dynamic behaviour of ohmic contacts under varying operational conditions. Exploring different device geometries and employing advanced characterisation techniques can further refine our understanding and contribute to the ongoing evolution of GaN-based HEMT technologies.

In conclusion, this thesis contributes valuable insights to the field of semiconductor manufacturing and power electronics. The promising outcomes observed in specific contact resistivity measurements, aligned with theoretical expectations, underscore the efficiency of the studied ohmic contacts. The structural integrity confirmation and the detailed material specific performance analysis provide a robust foundation for the continuous refinement of ohmic contacts in GaN-based HEMT devices. As the semiconductor industry continues to evolve, the knowledge generated through this research serves as a catalyst for advancements in device design and performance optimization, ultimately driving innovations in power electronics applications.

References

[1] M. Spera, “Ohmic contacts on wide band gap semiconductors,” 2019.

[2] J. Bodzenta, B. Burak, A. Jagoda and B. Stanczyk, “Thermal conductivity of AlN and AlN–GaN thin films deposited on Si and GaAs substrates,” *Diamond and Related Materials,* vol. 14, no. 10.1016/j.diamond.2005.01.016, pp. 1169-1174, 2005.

[3] A. Lidow, J. Strydom, M. d. Rooij and D. Reusch, "GaN transistors for efficient power conversion", Chichester: John Wiley & Sons Ltd, 2015.

[4] S. Dimitrijev, “Power switching applications beyond silicon: The status and future prospects of SiC and GaN devices,” *International conference on microelectronics,* vol. 29, pp. 12-14, 2014.

[5] Wikipedia Contributors, “Gallium nitride,” Wikipedia, 11 November 2024. [Online]. Available: https://en.wikipedia.org/w/index.php?title=Gallium_nitride&oldid=1256729476. [Accessed 22 November 2024].

[6] M. A. Khan, K. Balakrishnan, T. M. Katona and A. S. Brown, “Spontaneous and piezoelectric polarization effects in III-V nitride semiconductor heterostructures,” *Journal of Applied Physics,* vol. 87, no. 5, pp. 2384-2393, 2000.

[7] O. Ambacher, “Growth and applications of group III-nitrides,” *Journal of Physics of Applied Physics,* vol. 31, no. 20, p. 2653, 1998.

[8] S. J. Pearton and F. Ren, “GaN materials and devices,” *Journal of Electronic Materials,* vol. 37, no. 5, pp. 605-617, 2008.

[9] H. Tietjen and H. P. Maruska, “The preparation and properties of vapour-deposition,” *Applied Physics Letters,* vol. 15, no. 327, 1969.

[10] A. Khan, N. Kuzina, D. T. Olson, W. J. Schaff and J. W. Burn, “Microwave performance of a 0.25μm gate AlGaN/GaN heterostructure field,” *Applied Physics Letters,* vol. 65, no. 1121-2, 1994.

[11] K. Cen, Z. Jianjun, K. Yuechan, Z. Kai and C. Tangsheng, “Enhancement-mode GaN HEMT power electronic device with low specific on resistance,” *China International Forum on Solid State Lighting: International Forum on Wide Bandgap Semiconductors China,* vol. 14, pp. 183-185, 2017.

[12] J. M. Lauenstein, M. C. Casey, R. L. Ladbury, H. S. Kim, A. M. Phan and A. D. Topper, “Space Radiation Effects on SiC Power Device Reliability,” *IEEE International Reliability Physics Symposium ,* pp. 1-8, 2021.

[13] K. Cheng, “AlGaN/GaN/AlGaN Double Heterostructures Grown on 200 mm Silicon (111) Substrates with High Electron Mobility,” *Applied Physics Letters,* vol. 5, 2012.

[14] TrendForce, “SiC and GaN Go Full Steam Ahead in Automotive Industry,” 22 October 2024. [Online]. Available: https://www.trendforce.com/news/2024/10/22/news-sic-and-gan-go-full-steam-ahead-in-automotive-industry/. [Accessed 30 December 2024].

[15] S. S. Kim, “Low-resistance Ti/Al-based ohmic contacts for AlGaN/GaN HEMTs,” *IEEE Electron Device Letters,* vol. 25, no. 8, p. 541–543, 2004.

[16] J. Y. Park, “High-Temperature Stability of Refractory Metal-Based Ohmic Contacts to GaN,” *Journal of Electronic Materials,* vol. 45, no. 3, p. 679–685, 2016.

[17] H. Xing, “Development of Gold-Free Ohmic Contacts for GaN Power Devices,” *Applied Physics Letters,* vol. 109, no. 12, 2018.

[18] Y. Yue, “Low-Resistance Ohmic Contacts Using Regrown GaN Layers,” *IEEE Transactions on Electron Devices,* vol. 67, no. 3, 2020.

[19] C. Gupta, “Tunnel Junction Contacts for GaN HEMTs,” *Applied Physics Letters,* vol. 115, no. 21, 2019.

[20] Y. Takei, M. Kamiya and K. Tsutsui, “Reduction of contact resistance on AlGaN/GaN HEMT structures introducing uneven AlGaN layers,” *Phys. Status Solidi,* vol. 212, no. 5, p. 1104–1109, 2015.

[21] N. F. Mott, “Note on the contact between a metal an insulator or semiconductor,” *Cambridge Philosophical Society,* vol. 34, pp. 568-572, 1938.

[22] J. Bardeen, “Surface States and Rectification at a Metal Semi-Conductor Contact,” *Physics Review,* vol. 71, p. 717, 1947.

[23] S. K. Lee, “Processing and Characterization of Silicon Carbide (6H- and 4H-SiC) Contacts for High Power and High Temperature Device Applications,” Stockholm, 2002.

[24] M. S. Arora, “Analytical Model for Two-Dimensional Electron Gas Charge Density in Recessed-Gate GaN High-Electron-Mobility Transistors,” *Journal of Electronic Materials,* vol. 50, no. 4, p. 1550–1557, 2021.

[25] K. WEN, “Study of ohmic contact formation on AlGaN/GaN heterostructures,” 2019.

[26] R. Fitzgerald, K. Keil and K. Heinrich, “Solid-state energy-dispersive spectrometer for electron-microprobe X-ray analysis,” *Science,* no. 159, pp. 528-530, 1968.

[27] W. Bragg, “The specular reflection of X-rays,” *Nature,* vol. 90, no. 2250, 1912.

[28] Tescan Orsay holding, “An ultimate resolution FIB-SEM workbench for advanced nanofabrication applications,” [Online]. Available: https://irp-cdn.multiscreensite.com/ebc29cc1/files/uploaded/TESCAN%20SOLARIS_Product%20Data%20Sheet.pdf. [Accessed 31 December 2024].

[29] E. Ruska, “The development of the electron microscope and of electron microscopy,” *Nobel lecture,* vol. 1, no. 1, p. 26, 1986.

[30] Tescan Orsay Holdings, “Tescan Solaris,” marketing@tescan, Brno, 2021.

[31] W. Shockley, “Research and Investigation of Inverse Epitaxial UHF Power Transistors,” Air Force Avionics Lab, Ohio, 1964.

[32] B. J. Baliga, "Gallium Nitride And Silicon Carbide Power Devices", World Scientific, 2017.

[33] I. NobbiP, “Wikipedia,” 29 April 2008. [Online]. Available: https://commons.wikimedia.org/wiki/File:Tranputer_83.jpg. [Accessed 17 August 2023].

Appendix

The appendix contains all the electrical data collated from the six wafers, plus MATLAB code. All six wafers were electrically analysed on a Cascade Microtech Alessi REL-6100 200mm 8" Wafer Probe Station, this probe station is rated up to 200V and is more than suitable for the required testing. The probe station is sat upon a vibration table.

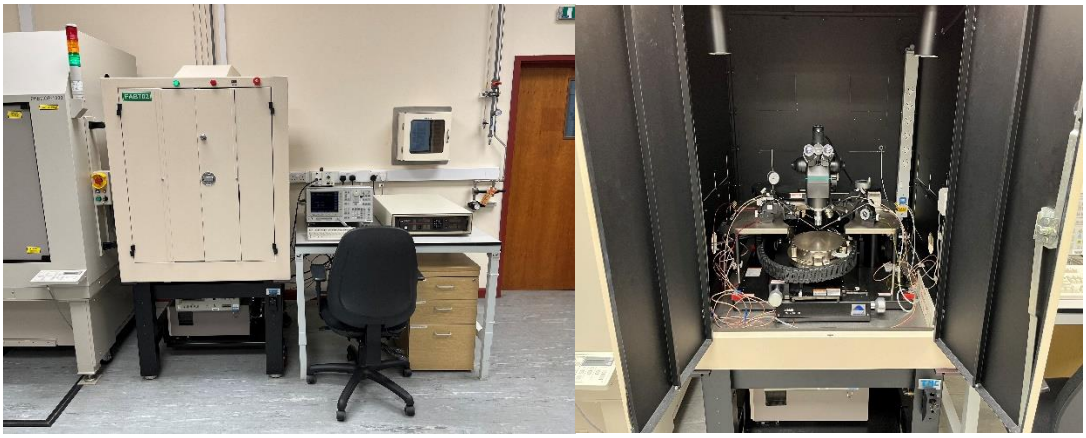

Fig. A 0: Alessi bench tester

The HP4156B provides characterisation measurements for semiconductor devices and process control modules. Each of the six wafers were individually tested on the TLM structures. I/V curves were taken of the individual contact spacings (2µm, 5µm, 10µm, 15µm, 20µm and 25µm). This was repeated at the center, mid-radius, and edge of the wafers at 300°K, 325°K, 350°K, 375°K and 400k°K. From this electrical data we could then extract:

- Resistance (Ω)
- Slope (µm)
- Contact resistance (Ωmm)
- Sheet resistance (Ω/sq)
- Transfer length (um)
- Specific contact resistance (Ωcm^2)

Wafer 01: AlN, GaN/AlGaN buffer & GaN - 250ÅTi / 3000Å AlCu contacts

Table 9.1: Wafer 01: AlN, GaN/AlGaN buffer & GaN - 250ÅTi / 3000Å AlCu contacts – Electrical data

		CENTER				
		300k	**325k**	**350k**	**375k**	**400k**
Resistance	**Ω**	2746.00	1280.00	800.00	538.00	407.00
Slope	**µm**	45.00	17.41	13.96	11.54	12.36
Contact resistance	**Ωmm**	1373.00	640.00	400.00	269.00	203.50
Sheet resistance	**Ω/sq**	4500.00	1741.00	1396.00	1154.00	1236.00
Transfer length	**um**	30.51	36.76	28.65	23.31	16.46
Specific contact resistance	**Ωcm^2**	4.19E-02	2.35E-02	1.15E-02	6.27E-03	3.35E-03
		MID-RADIUS				
		300k	**325k**	**350k**	**375k**	**400k**
Resistance	**Ω**	5728.00	2533.00	1361.00	916.00	641.00
Slope	**µm**	123.30	52.60	29.00	18.30	16.90
Contact resistance	**Ωmm**	2864.00	1266.50	680.50	458.00	320.50
Sheet resistance	**Ω/sq**	12330.00	5260.00	2900.00	1830.00	1690.00
Transfer length	**um**	23.23	24.08	23.47	25.03	18.96
Specific contact resistance	**Ωcm^2**	6.65E-02	3.05E-02	1.60E-02	1.15E-02	6.08E-03
		EDGE				
		300k	**325k**	**350k**	**375k**	**400k**
Resistance	**Ω**	3593.00	8381.00	1893.00	1195.00	806.00
Slope	**µm**	3.67	27.94	0.24	3.72	6.78
Contact resistance	**Ωmm**	1796.50	4190.50	946.50	597.50	403.00
Sheet resistance	**Ω/sq**	367.20	2794.00	23.97	371.80	678.00
Transfer length	**um**	489.24	149.98	144.35	160.70	59.44
Specific contact resistance	**Ωcm^2**	8.79E-01	6.28E-01	3.74E+00	9.60E-02	2.40E-02
		AVERAGE				
		300k	**325k**	**350k**	**375k**	**400k**
Resistance	**Ω**	4022.33	4064.67	1351.33	883.00	618.00
Slope	**µm**	57.32	32.65	14.40	11.19	12.01
Contact resistance	**Ωmm**	2011.17	2032.33	675.67	441.50	309.00
Sheet resistance	**Ω/sq**	5732.40	3265.00	1439.99	1118.60	1201.33
Transfer length	**um**	180.99	70.27	65.49	69.68	31.62
Specific contact resistance	**Ωcm^2**	3.29E-01	2.28E-01	1.25E+00	3.79E-02	1.11E-02

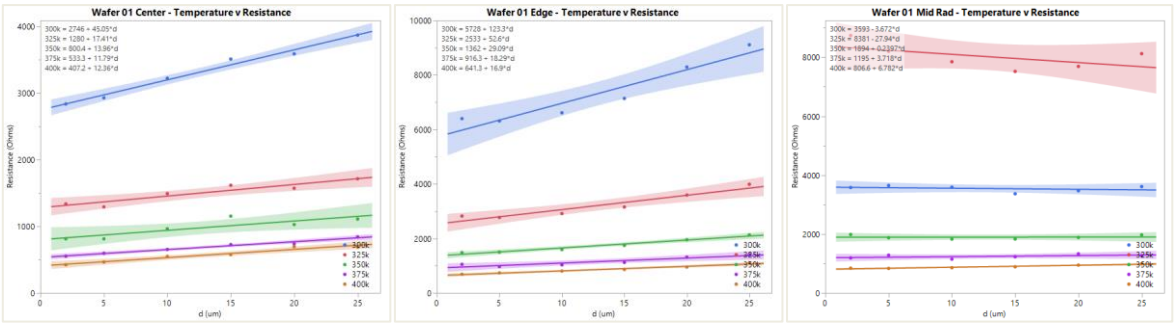

Fig. A.1: Wafer 01: AlN, GaN/AlGaN buffer & GaN - 250ÅTi / 3000Å AlCu contacts, temperature v resistance center, mid radius, and edge

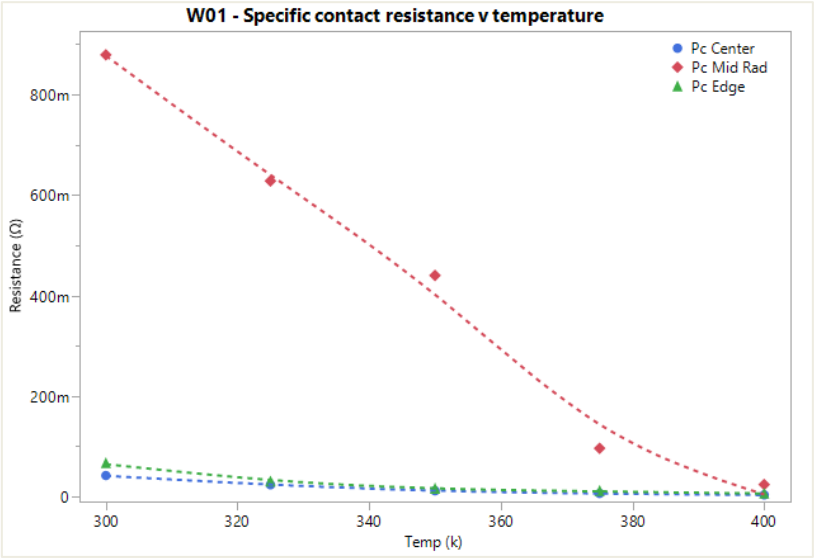

Fig. A.2: Wafer 01: AlN, GaN/AlGaN buffer & GaN - 250ÅTi / 3000Å AlCu, specific contact resistance v temperature, center, mid radius, and edge

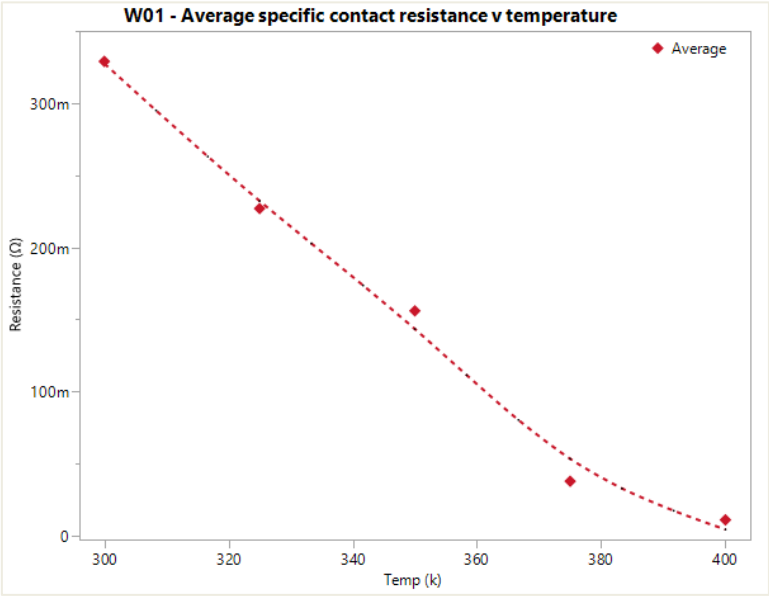

Fig. A.3: Wafer 01: AlN, GaN/AlGaN buffer & GaN - 250ÅTi / 3000Å AlCu, average specific contact resistance v temperature, center, mid radius, and edge

Wafer 02: AlN, GaN/AlGaN buffer & GaN - 250ÅTi / 3000Å AlCu contacts

Table 9.2: Wafer 02: AlN, GaN/AlGaN buffer & GaN - 250ÅTi / 3000Å AlCu contacts – Electrical data

		CENTER				
		300k	**325k**	**350k**	**375k**	**400k**
Resistance	**Ω**	974.00	729.00	567.00	464.00	420.00
Slope	**µm**	2.71	2.04	3.64	5.03	5.86
Contact resistance	**Ωmm**	487.00	364.50	283.50	232.00	210.00
Sheet resistance	**Ω/sq**	271.20	204.00	363.90	502.80	585.60
Transfer length	**um**	179.57	178.68	77.91	46.14	35.86
Specific contact resistance	**Ωcm^2**	8.75E-02	6.51E-02	2.21E-02	1.07E-02	7.53E-03
		MID-RADIUS				
		300k	**325k**	**350k**	**375k**	**400k**
Resistance	**Ω**	743.00	625.00	555.00	457.00	436.00
Slope	**µm**	7.43	5.58	4.62	7.01	5.89
Contact resistance	**Ωmm**	371.50	312.50	277.50	228.50	218.00
Sheet resistance	**Ω/sq**	742.90	557.70	461.70	701.00	588.70
Transfer length	**um**	50.01	56.03	60.10	32.60	37.03
Specific contact resistance	**Ωcm^2**	1.86E-02	1.75E-02	1.67E-02	7.45E-03	8.07E-03
		EDGE				
		300k	**325k**	**350k**	**375k**	**400k**
Resistance	**Ω**	8345.10	4262.00	2422.00	1566.00	1218.00
Slope	**µm**	564.69	56.00	20.68	8.19	1.15
Contact resistance	**Ωmm**	4172.55	2131.00	1211.00	783.00	609.00
Sheet resistance	**Ω/sq**	5646.00	5600.00	2068.00	818.60	115.10
Transfer length	**um**	7.39	38.05	58.56	95.65	529.11
Specific contact resistance	**Ωcm^2**	3.08E-02	8.11E-02	7.09E-02	7.49E-02	3.22E-01
		AVERAGE				
		300k	**325k**	**350k**	**375k**	**400k**
Resistance	**Ω**	3354.03	1872.00	1181.33	829.00	691.33
Slope	**µm**	191.61	21.21	9.65	6.74	4.30
Contact resistance	**Ωmm**	1677.02	936.00	590.67	414.50	345.67
Sheet resistance	**Ω/sq**	2220.03	2120.57	964.53	674.13	429.80
Transfer length	**um**	78.99	90.92	65.52	58.13	200.67
Specific contact resistance	**Ωcm^2**	4.56E-02	5.46E-02	3.66E-02	3.10E-02	1.13E-01

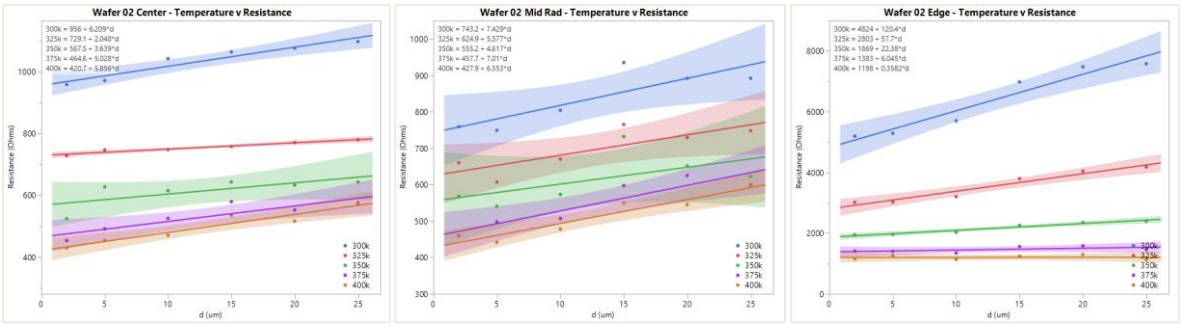

Fig. A 4: Wafer 02: AlN, GaN/AlGaN buffer & GaN - 250ÅTi / 3000Å AlCu contacts temperature v resistance center, mid radius, and edge

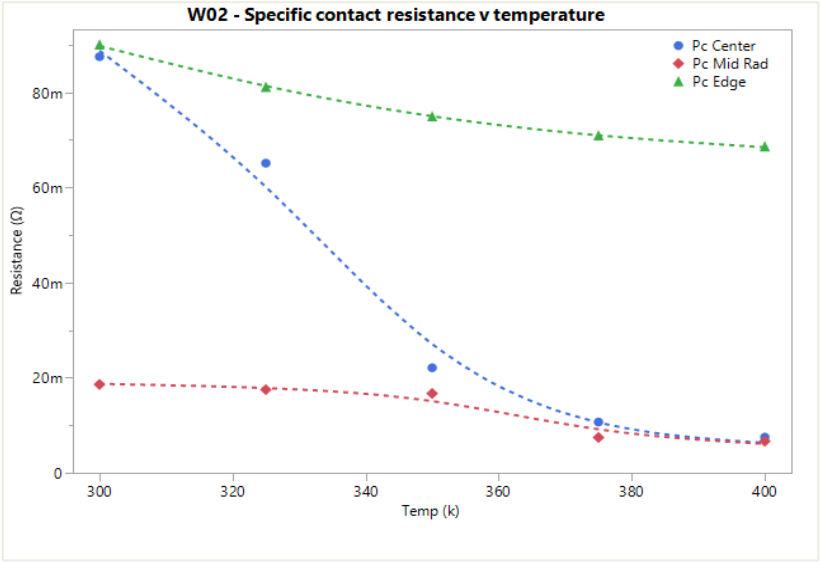

Fig. A 5: Wafer 02: AlN, GaN/AlGaN buffer & GaN - 250ÅTi / 3000Å AlCu contacts specific contact resistance v temperature, center, mid radius, and edge

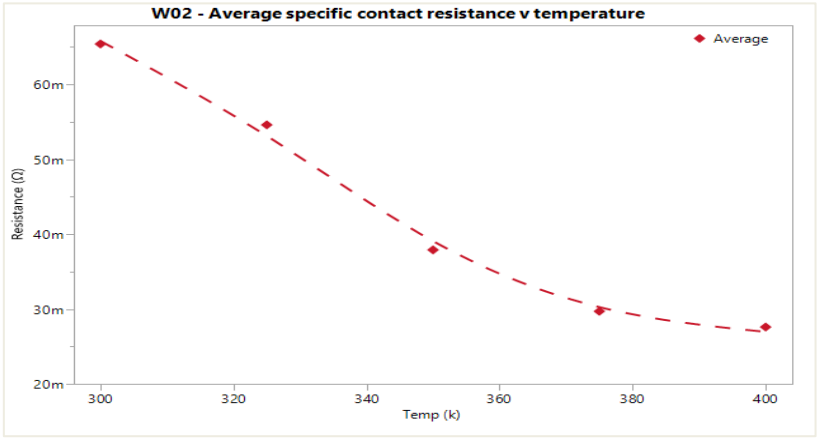

Fig. A 6: Wafer 02: AlN, GaN/AlGaN buffer & GaN - 250ÅTi / 3000Å AlCu contacts, average specific contact resistance v temperature, center, mid radius, and edge

Wafer 03: AlN, GaN/AlGaN buffer & GaN - 250ÅTi / 3000Å Pure Al contacts

Table 9.3: Wafer 03: AlN, GaN/AlGaN buffer & GaN - 250ÅTi / 3000Å Pure Al contacts – Electrical data

		CENTER				
		300k	**325k**	**350k**	**375k**	**400k**
Resistance	**Ω**	419.63	346.00	324.00	301.00	276.00
Slope	**µm**	2.59	4.11	4.36	5.20	5.74
Contact resistance	**Ωmm**	209.82	173.00	162.00	150.50	138.00
Sheet resistance	**Ω/sq**	258.64	411.00	435.61	520.13	574.07
Transfer length	**um**	81.12	42.09	37.19	28.94	24.04
Specific contact resistance	**Ωcm^2**	1.70E-02	7.28E-03	6.02E-03	4.35E-03	3.32E-03
		MID-RADIUS				
		300k	**325k**	**350k**	**375k**	**400k**
Resistance	**Ω**	327.00	266.50	255.00	230.00	214.00
Slope	**µm**	2.72	4.22	4.38	5.18	6.17
Contact resistance	**Ωmm**	163.50	133.25	127.50	115.00	107.00
Sheet resistance	**Ω/sq**	271.90	422.30	437.90	517.70	616.80
Transfer length	**um**	60.13	31.55	29.12	22.21	17.35
Specific contact resistance	**Ωcm^2**	9.83E-03	4.20E-03	3.71E-03	2.55E-03	1.86E-03
		EDGE				
		300k	**325k**	**350k**	**375k**	**400k**
Resistance	**Ω**	649.00	524.00	474.00	397.00	369.00
Slope	**µm**	11.32	8.80	7.40	8.45	8.23
Contact resistance	**Ωmm**	324.50	262.00	237.00	198.50	184.50
Sheet resistance	**Ω/sq**	1132.00	880.00	740.00	845.00	823.00
Transfer length	**um**	28.67	29.77	32.03	23.49	22.42
Specific contact resistance	**Ωcm^2**	9.30E-03	7.80E-03	7.59E-03	4.66E-03	4.14E-03
		AVERAGE				
		300k	**325k**	**350k**	**375k**	**400k**
Resistance	**Ω**	465.21	378.83	351.00	309.33	286.33
Slope	**µm**	5.54	5.71	5.38	6.28	6.71
Contact resistance	**Ωmm**	232.61	189.42	175.50	154.67	143.17
Sheet resistance	**Ω/sq**	554.18	571.10	537.84	627.61	671.29
Transfer length	**um**	56.64	34.47	32.78	24.88	21.27
Specific contact resistance	**Ωcm^2**	1.21E-02	6.43E-03	5.78E-03	3.86E-03	3.10E-03

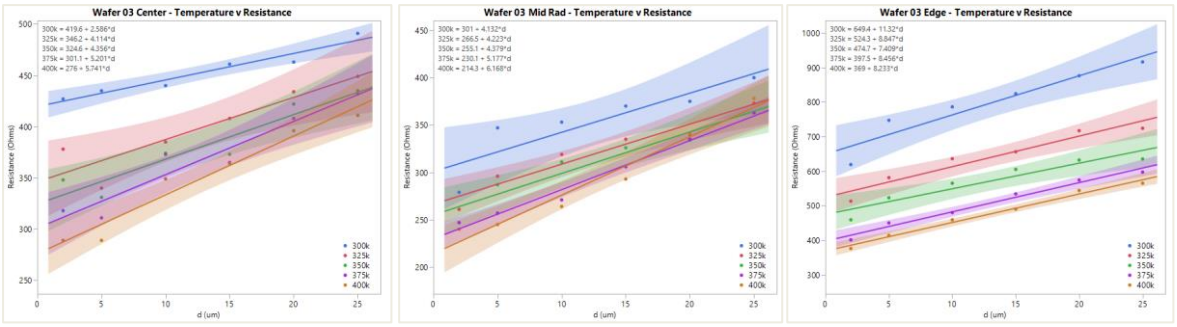

Fig. A 7: Wafer 03: AlN, GaN/AlGaN buffer & GaN - 250ÅTi / 3000Å Pure Al contacts, temperature v resistance center, mid radius, and edge

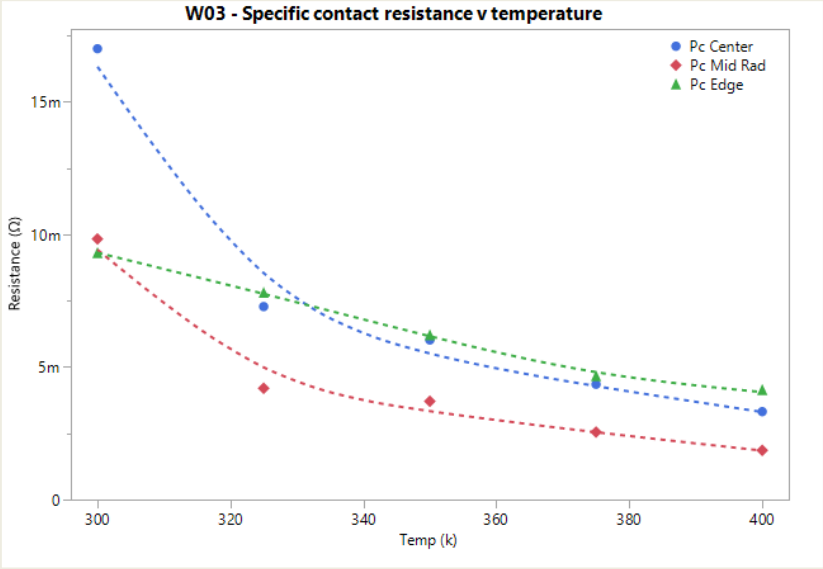

Fig. A 8: Wafer 03: AlN, GaN/AlGaN buffer & GaN - 250ÅTi / 3000Å Pure Al contacts, specific contact resistance v temperature, center, mid radius, and edge

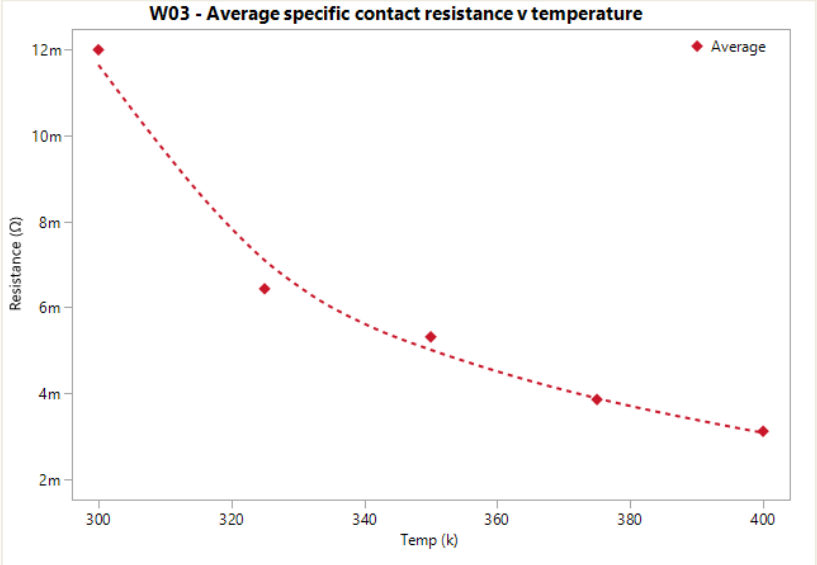

Fig. A 9: Wafer 03: AlN, GaN/AlGaN buffer & GaN - 250ÅTi / 3000Å Pure Al contacts, average specific contact resistance v temperature, center, mid radius, and edge

Wafer 07: Nucleation, GaN/AlGaN buffer & GaN - 400ÅTa / 2000Å Pure Al contacts

Table 9.4: Wafer 07: Nucleation, GaN/AlGaN buffer & GaN - 400ÅTa / 2000Å Pure Al contacts – Electrical data

		CENTER				
		300k	**325k**	**350k**	**375k**	**400k**
Resistance	**Ω**	331908.00	120599.00	41396.00	15841.00	7230.00
Slope	**µm**	24085.00	198.77	15.02	11.61	13.40
Contact resistance	**Ωmm**	165954.00	60299.50	20698.00	7920.50	3615.00
Sheet resistance	**Ω/sq**	1408500.00	19877.00	1501.80	1161.10	1339.80
Transfer length	**um**	6.89	303.36	1378.21	682.15	269.82
Specific contact resistance	**Ωcm^2**	1.14E+00	1.83E+01	2.85E+01	5.40E+00	9.75E-01
		MID-RADIUS				
		300k	**325k**	**350k**	**375k**	**400k**
Resistance	**Ω**	864041.00	360701.00	95645.00	33593.00	13803.00
Slope	**µm**	3510.90	642.36	33.24	87.10	11.73
Contact resistance	**Ωmm**	432020.50	180350.50	47822.50	16796.50	6901.50
Sheet resistance	**Ω/sq**	351090.00	64236.00	3323.60	8709.90	1172.80
Transfer length	**um**	123.05	280.76	1438.88	192.84	588.46
Specific contact resistance	**Ωcm^2**	5.32E+01	5.06E+01	6.88E+01	3.24E+00	4.06E+00
		EDGE				
		300k	**325k**	**350k**	**375k**	**400k**
Resistance	**Ω**	2000000.00	397879.00	110814.00	35502.00	12929.00
Slope	**µm**	9494.90	433.94	416.37	108.68	57.16
Contact resistance	**Ωmm**	1000000.00	198939.50	55407.00	17751.00	6464.50
Sheet resistance	**Ω/sq**	949490.00	43394.00	41637.00	10868.00	5715.60
Transfer length	**um**	105.32	458.45	133.07	163.33	113.10
Specific contact resistance	**Ωcm^2**	1.05E+02	9.12E+01	7.37E+00	2.90E+00	1.10E+00
		AVERAGE				
		300k	**325k**	**350k**	**375k**	**400k**
Resistance	**Ω**	1065316.3	293059.7	82618.33	28312	11320.67
Slope	**µm**	12363.6	425.0233	154.8747	69.13	27.42733
Contact resistance	**Ωmm**	532658.17	146529.8	41309.17	14156	5660.333
Sheet resistance	**Ω/sq**	903026.67	42502.33	15487.47	6913	2742.733
Transfer length	**um**	78.420419	347.525	983.387	346.1104	323.7942
Specific contact resistance	**Ωcm^2**	53.207965	53.37731	34.90335	3.847143	2.044465

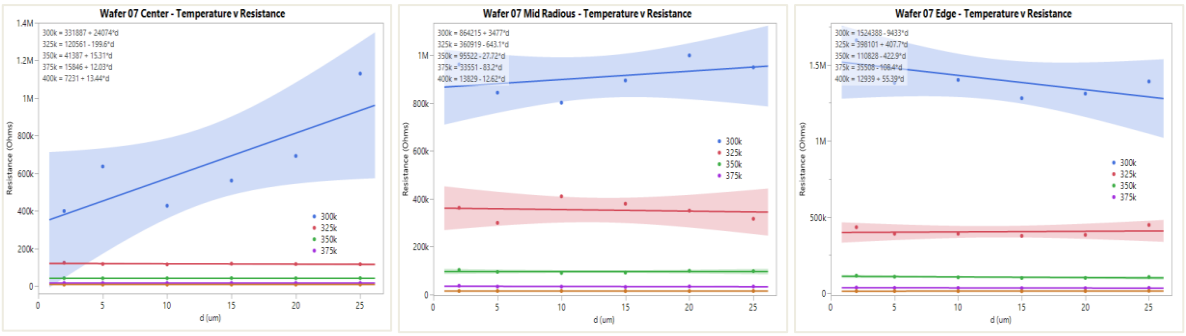

Fig. A 10: Wafer 07: Nucleation, GaN/AlGaN buffer & GaN - 400ÅTa / 2000Å Pure Al contacts, temperature v resistance center, mid radius, and edge

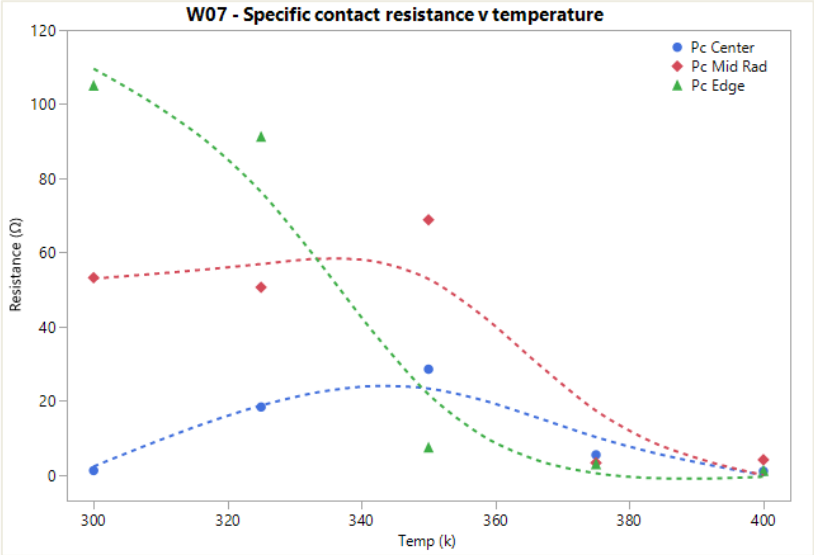

Fig. A 11: Wafer 07: Nucleation, GaN/AlGaN buffer & GaN - 400ÅTa / 2000Å Pure Al contacts, specific contact resistance v temperature, center, mid radius, and edge

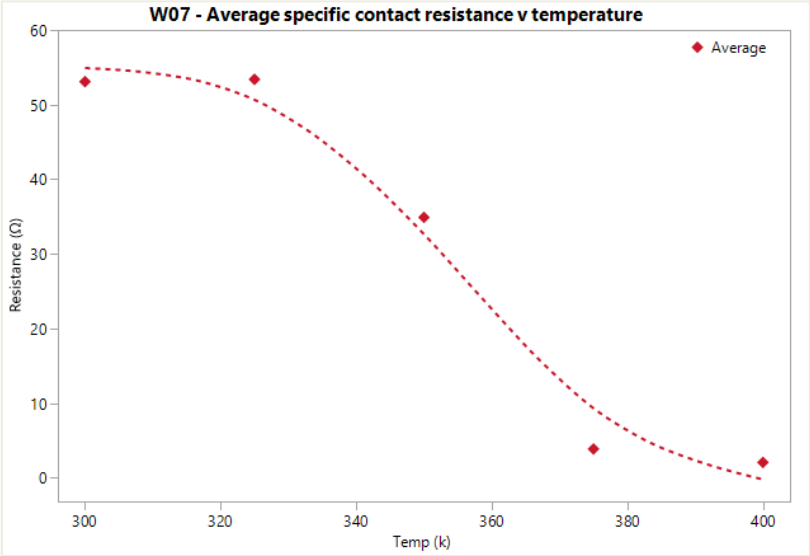

Fig. A 12: Wafer 07: Nucleation, GaN/AlGaN buffer & GaN - 400ÅTa / 2000Å Pure Al contacts, average specific contact resistance v temperature, center, mid radius, and edge

Wafer 08: Nucleation, GaN/AlGaN buffer & GaN - 250ÅTi / 3000Å AlCu contacts

Table 9.5: Wafer 08: Nucleation, GaN/AlGaN buffer & GaN - 250ÅTi / 3000Å AlCu contacts – Electrical data

		CENTER				
		300k	**325k**	**350k**	**375k**	**400k**
Resistance	**Ω**	495.50	402.77	331.41	275.93	253.07
Slope	**µm**	4.38	4.58	5.49	6.16	6.42
Contact resistance	**Ωmm**	247.75	201.39	165.71	137.97	126.54
Sheet resistance	**Ω/sq**	437.70	457.61	548.78	616.12	642.35
Transfer length	**um**	56.60	44.01	30.20	22.39	19.70
Specific contact resistance	**Ωcm^2**	1.40E-02	8.86E-03	5.00E-03	3.09E-03	2.49E-03
		MID-RADIUS				
		300k	**325k**	**350k**	**375k**	**400k**
Resistance	**Ω**	446.42	361.22	327.80	281.09	254.62
Slope	**µm**	4.30	4.72	5.02	5.60	6.68
Contact resistance	**Ωmm**	223.21	180.61	163.90	140.55	127.31
Sheet resistance	**Ω/sq**	429.92	472.28	501.54	560.34	667.89
Transfer length	**um**	51.92	38.24	32.68	25.08	19.06
Specific contact resistance	**Ωcm^2**	1.16E-02	6.91E-03	5.36E-03	3.53E-03	2.43E-03
		EDGE				
		300k	**325k**	**350k**	**375k**	**400k**
Resistance	**Ω**	1010.00	675.31	524.84	414.30	369.00
Slope	**µm**	5.78	6.75	6.71	8.09	8.60
Contact resistance	**Ωmm**	505.00	337.66	262.42	207.15	184.50
Sheet resistance	**Ω/sq**	578.28	675.48	671.39	809.34	859.79
Transfer length	**um**	87.33	49.99	39.09	25.59	21.46
Specific contact resistance	**Ωcm^2**	4.41E-02	1.69E-02	1.54E-02	5.30E-03	3.96E-03
		AVERAGE				
		300k	**325k**	**350k**	**375k**	**400k**
Resistance	**Ω**	650.64	479.7667	394.6833	323.7733	292.23
Slope	**µm**	4.81967	5.351233	5.739033	6.619333	7.233433
Contact resistance	**Ωmm**	325.32	239.8833	197.3417	161.8867	146.115
Sheet resistance	**Ω/sq**	481.967	535.1233	573.9033	661.9333	723.3433
Transfer length	**um**	65.283158	44.07919	33.98686	24.35653	20.073
Specific contact resistance	**Ωcm^2**	2.32E-02	1.09E-02	8.58E-03	3.97E-03	2.96E-03

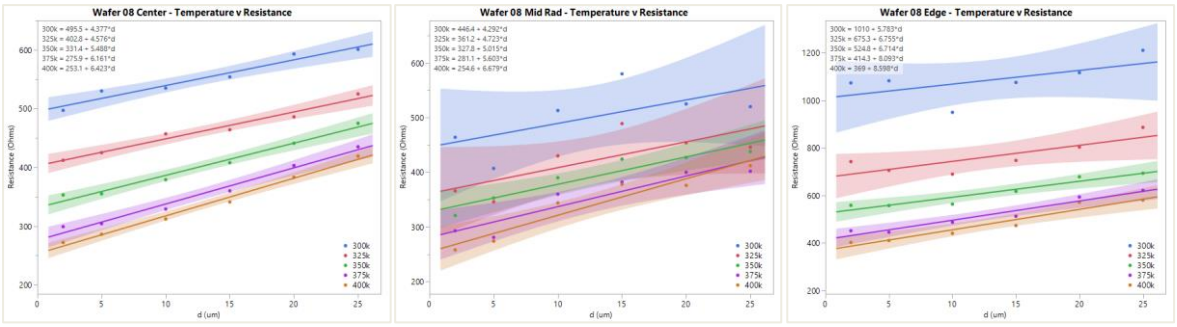

Fig. A 13: : Wafer 08: Nucleation, GaN/AlGaN buffer & GaN - 250ÅTi / 3000Å AlCu contacts, temperature v resistance center, mid radius, and edge

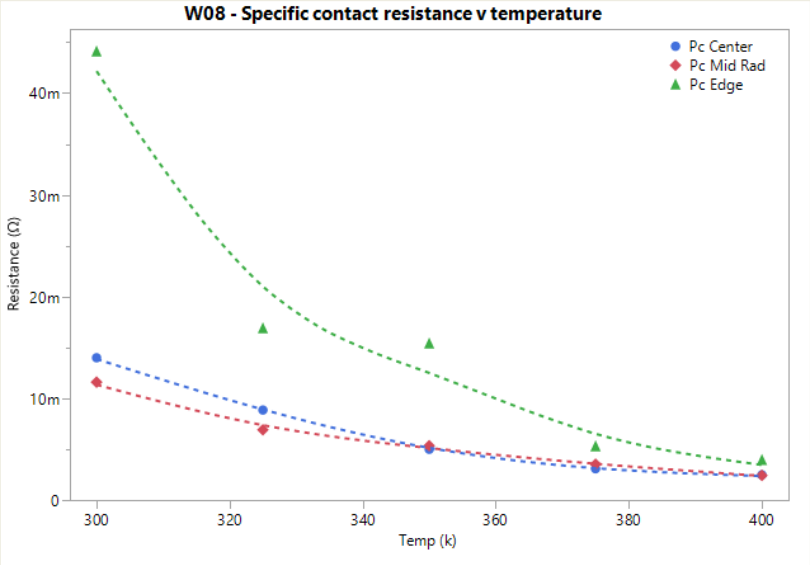

Fig. A 14: Wafer 08: Nucleation, GaN/AlGaN buffer & GaN - 250ÅTi / 3000Å AlCu contacts, specific contact resistance v temperature, center, mid radius, and edge

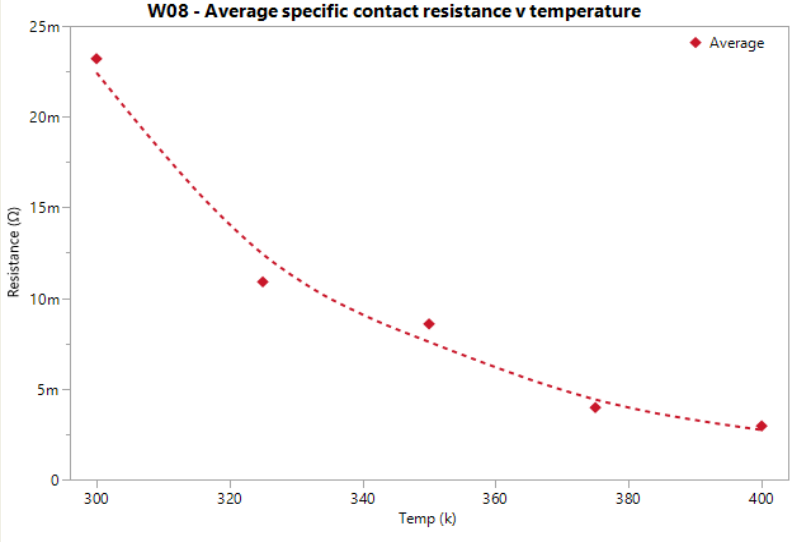

Fig. A 15: Wafer 08: Nucleation, GaN/AlGaN buffer & GaN - 250ÅTi / 3000Å AlCu contacts, average specific contact resistance v temperature, center, mid radius, and edge

Wafer 09: Nucleation, GaN/AlGaN buffer & GaN - 250ÅTi / 3000Å Pure Al contacts

Table 9.6: Wafer 09: Nucleation, GaN/AlGaN buffer & GaN - 250ÅTi / 3000Å Pure Al contacts – Electrical data

		CENTER				
		300k	**325k**	**350k**	**375k**	**400k**
Resistance	**Ω**	797.00	570.00	451.00	364.00	308.00
Slope	**µm**	4.09	5.24	5.00	7.78	6.31
Contact resistance	**Ωmm**	398.50	285.00	225.50	182.00	154.00
Sheet resistance	**Ω/sq**	409.00	524.00	500.00	778.00	631.00
Transfer length	**um**	97.43	54.39	45.10	23.39	24.41
Specific contact resistance	**Ωcm^2**	3.88E-02	1.55E-02	1.02E-02	4.26E-03	3.76E-03
		MID-RADIUS				
		300k	**325k**	**350k**	**375k**	**400k**
Resistance	**Ω**	488.17	418.00	317.27	280.61	236.40
Slope	**µm**	4.10	3.60	6.07	5.85	6.36
Contact resistance	**Ωmm**	244.09	209.00	158.64	140.31	118.20
Sheet resistance	**Ω/sq**	410.36	360.00	606.95	584.82	635.82
Transfer length	**um**	59.48	58.06	26.14	23.99	18.59
Specific contact resistance	**Ωcm^2**	1.45E-02	1.21E-02	4.15E-03	3.37E-03	2.20E-03
		EDGE				
		300k	**325k**	**350k**	**375k**	**400k**
Resistance	**Ω**	825.54	599.81	449.31	375.96	332.52
Slope	**µm**	15.91	12.11	9.50	9.46	7.99
Contact resistance	**Ωmm**	412.77	299.91	224.66	187.98	166.26
Sheet resistance	**Ω/sq**	1590.60	1210.50	949.55	945.76	798.55
Transfer length	**um**	25.95	24.78	23.66	19.88	20.82
Specific contact resistance	**Ωcm^2**	1.07E-02	7.43E-03	5.32E-03	3.74E-03	3.46E-03
		AVERAGE				
		300k	**325k**	**350k**	**375k**	**400k**
Resistance	**Ω**	703.57	529.27	405.86	340.19	292.3067
Slope	**µm**	8.0332	6.981667	6.855	7.695267	6.884567
Contact resistance	**Ωmm**	351.785	264.635	202.93	170.095	146.1533
Sheet resistance	**Ω/sq**	803.32	698.1667	685.5	769.5267	688.4567
Transfer length	**um**	60.954682	45.74006	31.63184	22.42018	21.27204
Specific contact resistance	**Ωcm^2**	2.14E-02	1.17E-02	6.54E-03	3.79E-03	3.14E-03

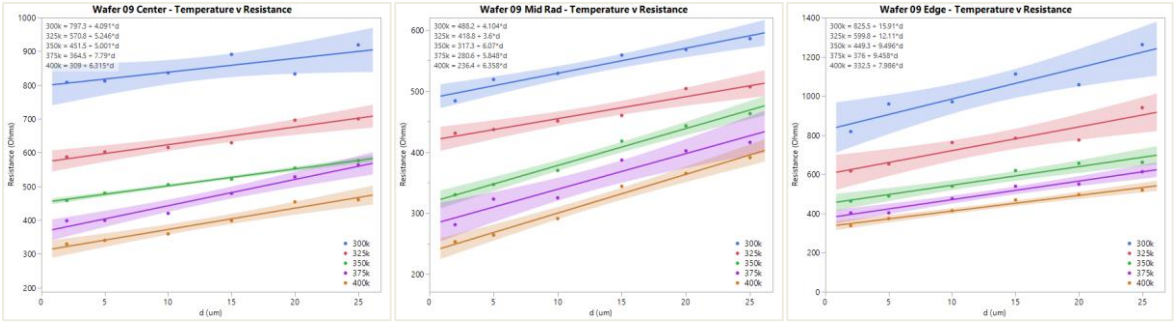

Fig. A 16: Wafer 09: Nucleation, GaN/AlGaN buffer & GaN - 250ÅTi / 3000Å Pure Al contacts, temperature v resistance center, mid radius, and edge

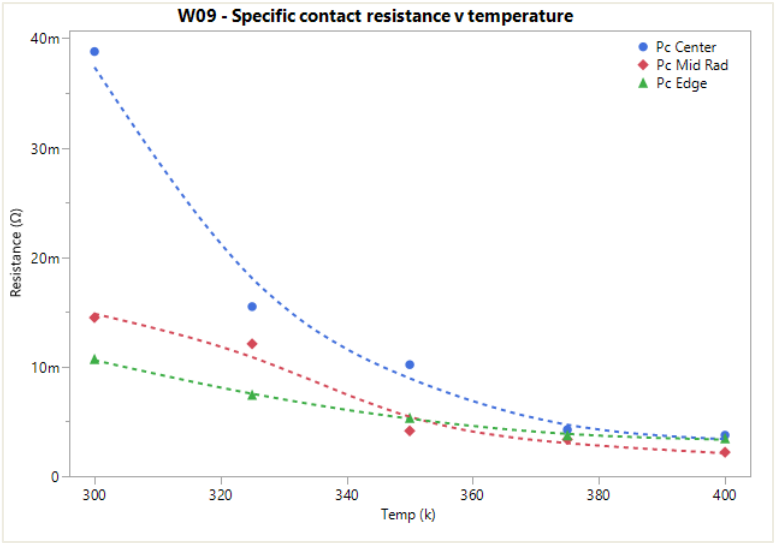

Fig. A 17: Wafer 09: Nucleation, GaN/AlGaN buffer & GaN - 250ÅTi / 3000Å Pure Al contacts, specific contact resistance v temperature, center, mid radius, and edge

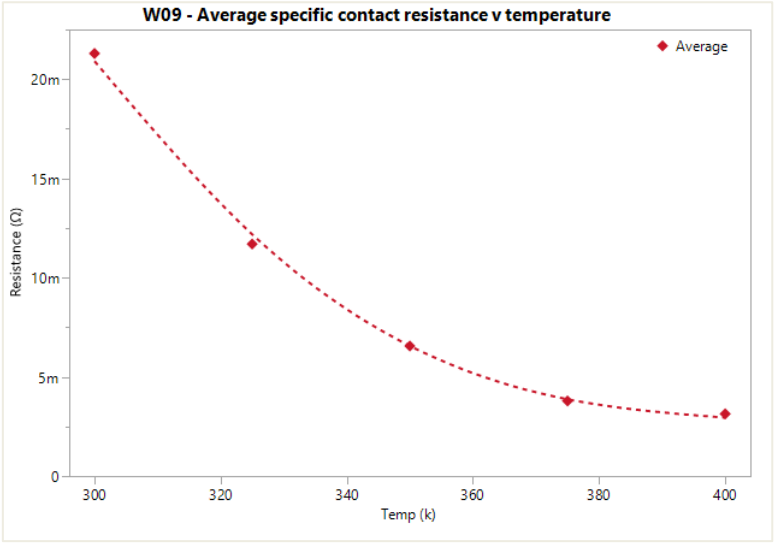

Fig. A 18: Wafer 09: Nucleation, GaN/AlGaN buffer & GaN - 250ÅTi / 3000Å Pure Al contacts, average specific contact resistance v temperature, center, mid radius, and edge

GaN HEMT Unipolar Limit – MATLAB code

Model taken from B. J. Baliga "Gallium nitride and silicon carbide power devices", 2017 Publisher "World Scientific" chapter 13 page 406 [32]

```
clear; clc; close all;

% Basic HEMT parameters
BV=100; %Breakdown voltage array (V)
eps = (10.4*8.85e-14); %GaN Relative Permittivity (Fcm-1)
E_avlat = 1e6; %Average Lateral Electric Field (V/cm)

% HEMT Geometry
L_S = 5e-4; %Source contact length (cm)
L_GS = 1e-4; %Gate-Source Length (cm)
L_G = 1e-4; %Gate length (cm)
L_D = 5e-4; %Drain contact length (cm)
L_GD = BV./E_avlat; %Gate-Drain Length (cm)
p = L_S+L_GS+L_G+L_GD+L_D; %Device pitch (lateral) (cm)

% for i=1:length(BV)
% L_GD(i) = BV(i)./E_avlat; %Gate-Drain Length (cm)
% p(i) = L_S+L_GS+L_G+L_GD(i)+L_D; %Device pitch (lateral) (cm)
% end

% Specific Resistances
rho_c = [1e-6 5e-6 1e-5 5e-5 1e-4 5e-4 1e-3]; %Specific contact resistance
(ohm-cm2)
rho_2D = 300; %2DEG resistance (ohm or ohm/sq)

for i=1:length(rho_c)
R_SC_sp(i) = (rho_c(i)*p)/L_S; %Specific source contact
resistance (ohm-cm2)
R_GS_sp(i) = rho_2D*L_GS*p; %Specific gate-source resistance (ohmcm2)
R_G_sp(i) = rho_2D*L_G*p; %Specific gate resistance (ohm-cm2)
R_GD_sp(i) = rho_2D.*L_GD.*p; %Specific gate-drain resistance (ohmcm2)
R_DC_sp(i) = (rho_c(i)*p)/L_D; %Specific drain contact resistance
(ohm-cm2)
R_tot_sp(i)=R_SC_sp(i)+R_GS_sp(i)+R_G_sp(i)+R_GD_sp(i)+R_DC_sp(i);
%Total specific on-resistance (ohm-cm2)
End
```

Bar Chart Plot

```
% ind = [1 401 551 1101 1901 2901];
% BV_BAR = BV(ind);
% R_SC_sp_BAR = R_SC_sp(ind);

% R_GS_sp_BAR = R_GS_sp(ind);
% R_G_sp_BAR = R_G_sp(ind);
% R_GD_sp_BAR = R_GD_sp(ind);
% R_DC_sp_BAR = R_DC_sp(ind);
% R_tot_sp_BAR = R_tot_sp(ind);
save BarChartRon rho_c R_SC_sp R_GS_sp R_G_sp R_GD_sp R_DC_sp R_tot_sp
```